TWO STAGGERED FINITE CIRCULAR CYLINDERS IN CROSS-FLOW

A Thesis Submitted to the College of
Graduate Studies and Research
in Partial Fulfillment of the Requirements
for the Degree of Master of Science
in the Department of Mechanical Engineering
University of Saskatchewan
Saskatoon

By
He Li

PERMISSION TO USE

The author grants permission to the Libraries of the University of Saskatchewan to make this thesis available for inspection. Permission for copying of this thesis in any manner, in whole or in part, for scholarly purposes should be granted by my supervisor, Prof. D. Sumner, the Head of the Department of Mechanical Engineering, or the Dean of the College of Engineering. It is understood that any copying or publication or use of this thesis or parts thereof for financial gain shall not be allowed without my written permission. It is also understood that due recognition shall be given to me and to the University of Saskatchewan in any scholarly use which may be made of any material in my thesis.

Requests for permission to copy or to make other use of material in this thesis, in whole or part, should be addressed to:

Head of the Department Mechanical Engineering

University of Saskatchewan

57 Campus Drive

Saskatoon, Saskatchewan, S7N 5A9

Canada

ABSTRACT

Circular cylinders in cross-flow have been extensively studied in the last century. However, there are still many unsolved problems in this area, one of which is the flow structure around two staggered finite circular cylinders. This thesis mainly focuses on an experimental investigation of the vortex shedding characteristics of two staggered finite circular cylinders of equal diameter in cross-flow. Wind tunnel experiments were conducted to measure the vortex shedding frequency at the mid-height of the two cylinders and along the height of the two cylinders. Two identical circular cylinders of aspect ratio AR = 9 were partially immersed in a flat-plate turbulent boundary layer, where the boundary layer thickness to cylinder height ratio at the location of the cylinders was $\delta/H = 0.4$. The Reynolds number based on the cylinder diameter was $Re_D = 2.4\times10^4$. Centre-to-centre pitch ratios of P/D = 1.125, 1.25, 1.5, 2, 2.5, 3, 4 and 5 were examined and the incidence angle was incremented in small steps from $\alpha = 0°$ to 180°. For each configuration of the cylinders, the vortex shedding frequency, represented in dimensionless form as the Strouhal number, St, was measured with a single-component hot-wire anemometer. Also, a seven-hole pressure probe was used to measure the time-averaged wake velocity field behind the cylinders at selected configurations in order to get a better understanding of the wake structure.

The vortex shedding frequencies measured at the mid-height of the cylinders clearly showed the similarities and differences of vortex shedding between two staggered

finite and infinite circular cylinders. The Strouhal number behavior of the two finite circular cylinders is generally similar to that of two infinite circular cylinders, but the values of St for the two finite cylinders were found for most cases to be smaller than the case of the infinite cylinders.

The measurements of vortex shedding frequency along the heights of each finite cylinder revealed that, for most incidence angles, the value of the Strouhal number remains constant along the height of the cylinder, but a notable variation in the shape and strength of the vortex shedding peak along the heights of the cylinders is observed. Sharp and strong peaks in the power spectra are measured around the mid-height of the cylinder. Broader and weaker peaks are found both at the base of the cylinder and near the free end. At several particular configurations, the vortex shedding frequency changes along the height of the cylinder, caused by the varying flow pattern in the vertical direction.

Wake measurements showed the velocity field behind the two finite circular cylinders arranged in tandem configurations of P/D = 1.125, 2 and 5. The experimental data revealed that the flow structure behind two finite circular cylinders arranged in a tandem configuration is much more complicated than that of the single finite circular cylinder. The downwash flow from the tip of the downstream cylinder is weaker due to the flow interaction between the free ends of two cylinders, and this downwash flow becomes stronger with increasing P/D. A similar trend happens to the vorticity of the tip vortex structures. However, the upwash flow behind the downstream cylinder is not strongly affected by the existence of the upstream cylinder.

ACKNOWLEDGMENTS

I would like to express my wholehearted gratitude to my supervisor, Prof. D. Sumner, for providing this research opportunity to me. I am also greatly indebted for his advice and guidance which significantly contributed to the successful completion of my program. Likewise, I want to send my gratitude to the members of my advisory committee, Prof. D.J. Bergstrom and Prof. J.D. Bugg, for their invaluable suggestions and advice on my research work as well as their inspiring lectures. The indispensable assistance from Mr. Dave Deutscher is also highly appreciated.

I also would like to thank my parents for their support and encouragement throughout my Master's degree program.

Special thanks go to my friends Samuel Adaramola, Chen Tiebing, Ji Ge, Lao Gao, Ye Dian and Yi Lang for their help both in my study and life.

TABLE OF CONTENTS

NOMENCLATURE

English Symbols

AR	aspect ratio of the cylinder
a	calibration constant for the hot-wire anemometer
B	bias error
b	coefficient for Sutherland correlation [kg/(m·s·K$^{1/2}$)]; calibration constant for the hot-wire anemometer
c	calibration constant for the hot-wire anemometer
D	diameter of the cylinder [mm]
E	voltage output from the hot-wire [V]
f	vortex shedding frequency [Hz]
H	height of the cylinder [mm]; boundary layer shape factor
P	centre-to-centre spacing or pitch [mm]; precision error
P/D	centre-to-centre pitch ratio
P_0	stagnation pressure [Pa]
P_∞	freestream static pressure [Pa]
q_∞	freestream dynamic pressure [Pa]
R	gas constant [J/kg·K]
Re_D	Reynolds number based on the cylinder diameter
Re_θ	Reynolds number based on the momentum thickness

S	reference temperature for the Sutherland correlation [K]
St	Strouhal number
T_∞	freestream temperature [°C]
t	two-tailed Student t number for the 95% confidence level
U	total uncertainty
U_∞	freestream velocity [m/s]
u	streamwise velocity component [m/s]
u^*	non-dimensional streamwise velocity component
v	cross-stream velocity component [m/s]
v^*	non-dimensional cross-stream velocity component
w	wall-normal velocity component [m/s]
w^*	non-dimensional wall-normal velocity component
x	streamwise coordinate direction [mm]; voltage combination [V]
y	cross-stream coordinate direction [mm]; voltage combination [V]
z	wall-normal coordinate direction [mm]

Greek Symbols

α	incidence angle [°]
δ	boundary layer thickness [mm]
δ^*	displacement thickness [mm]
μ_∞	freestream dynamic viscosity [Ns/m^2]

θ	momentum thickness [mm]
ρ_∞	freestream density [kg/m^3]
σ	uncertainty
ω_x	streamwise component of vorticity [1/s]
ω_x^*	non-dimensional streamwise component of vorticity

CHAPTER 1

INTRODUCTION

1.1 Circular Cylinders in Cross-Flow

As one of the most important research topics of bluff-body aerodynamics, the flow around a circular cylinder has been widely investigated in the past century due to the common occurrence of cylinder-like structures in engineering applications, such as cylindrical buildings (Fig. 1.1), power transmission lines (Fig. 1.2), and power station smokestacks (Fig. 1.3). Experimental results obtained from wind tunnel testing and numerical simulations obtained from computational fluid dynamics have been applied to calculate the wind load and the vibration of various cylindrical structures and also to study the behavior of the flow field. However, the wide range of studies in the literature is still not enough to clarify all the related problems and misunderstandings, simply because the flow around a cylinder is complicated and is easily affected by many factors, such as Reynolds number, aspect ratio, end configuration, blockage, freestream turbulence, surface roughness, interfering body proximity, body rotation, and so on. Therefore, this subject still poses great challenges for engineers and scientists, and stimulates people to put more attention and effort to research it.

Figure 1.1. Cylindrical buildings.

Figure 1.2. Smokestacks at a power plant.

Figure 1.3. Electrical transmission lines in the air.

It is easily seen that when the air flows around a circular cylinder, there are forces and moments applied on the cylinder. As the flow moves around the cylinder, boundary layers develop on the two sides of the cylinder. In many practical applications, such as in Figs. 1.1 to 1.3, the boundary layers separate from the circular cylinder due to the adverse pressure gradient and form two separated shear layers. The two shear layers from each side of the cylinder then roll up, alternately, into vortices. These vortices, once they are fully formed, are shed alternately from the cylinder, in a periodic fashion, as shown in Fig. 1.4, where D is the diameter of the circular cylinder and U_∞ is the incoming flow velocity. The wake region formed by the two rows of shed vortices behind the cylinder is called the Kármán vortex street. The vortex shedding frequency, f, at which vortices are shed from two sides of the circular cylinder, is represented in dimensionless form as the Strouhal number, $\mathrm{St} = fD/U_\infty$. The periodic vortex shedding from the circular cylinder can cause alternating low-pressure zones on the sides of the cylinder, leading potentially to cylinder vibration perpendicular to the direction of the airflow as well as acoustic noise. More importantly, when the vibration frequency is close to the natural frequency of the cylinder, resonance may occur which often leads to structural failure.

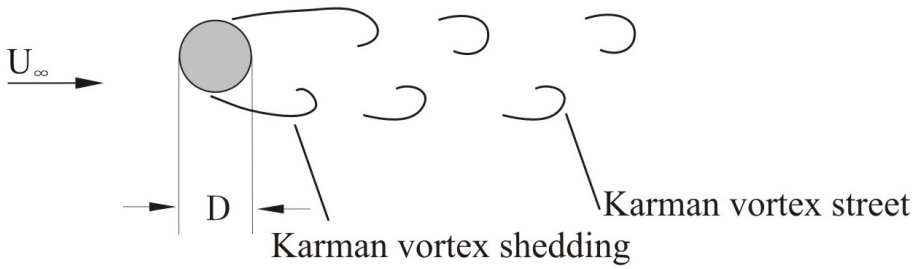

Figure 1.4. Flow around a single infinite circular cylinder.

Due to the importance of this subject, different flow measurement and simulation methods have been used to obtain a better understanding of the flow around the cylinder, including hot-film and hot-wire anemometry, various pressure probes, flow visualization, and computer modeling. Flow visualization techniques can provide detailed information about the flow pattern around the cylinder by putting visible particles into the fluid flow whose traces can be captured by a camera. The latest technique of quantitative flow visualization is particle image velocimetry (PIV) which is able to provide an entire velocity vector field showing the flow structure. Since computational fluid dynamics (CFD) has been developing rapidly during the last two decades, more and more researchers prefer to use computer simulations to model the flow structure around the circular cylinder and some of them have already obtained results that are in agreement with the experimental data. However, most of the flow visualization and computer modeling studies have been confined to relatively low Reynolds numbers and currently it is still not possible to obtain solutions for all flow conditions that originate from practical

applications, which are often at higher Reynolds numbers. The experimental approach is still the most dominant and efficient way to study the flow around bluff bodies.

So far, a considerable number of research studies regarding cross-flow past an "infinite" circular cylinder have been accomplished, since it is simplest model and is also treated as the basis for the study of more sophisticated cases. The characteristics of a single infinite circular cylinder in a cross-flow have been compiled in review articles by Coutanceau and Defaye (1991) and Williamson (1996), and textbooks by Sumer and Fredsoe (1997) and Zdravkovich (1997, 2003).

In some engineering applications, the cylindrical structures appear in groups. A simple model for the flow around small groups of circular cylinders is two circular cylinders in a staggered configuration, as shown in Fig. 1.5. The geometry of the two staggered circular cylinders is set by the centre-to-centre pitch ratio, P/D, where P is the center-to-center spacing, and the incidence angle, α. For two staggered cylinders, complex flow patterns are obtained as P/D and α are varied (Gu and Sun, 1999; Sumner et al., 2000; Sumner et al., 2005).

Recently, the finite circular cylinder has attracted particular attention, since many of the cylinder-like structures in the real world (Figs. 1.1 and 1.2, for example) are better modeled as finite cylinders (e.g., Okamoto and Yagita, 1973; Okamoto and Sunabashiri, 1992; Luo et al., 1996; Park and Lee, 2000; Sumner et al., 2004; Adaramola et al., 2006). Fig. 1.6 shows a circular cylinder of finite height mounted normal to a ground plane and partially immersed in a flat-plate boundary layer, where $U(z)$ is the incoming flow

velocity profile, z is the wall-normal coordinate, H is the height of the cylinder, and δ is the thickness of the boundary layer. The slenderness ratio or aspect ratio, AR, is defined as AR = H/D. The finite cylinder has aerodynamically distinct characteristics from the infinite cylinder because of its two ends. One of the ends is located on the ground plane and is known as the base of the cylinder (or the cylinder-wall junction), and the other is called the free end. The presence of the two ends makes the flow field around the finite cylinder more complicated and strongly three-dimensional compared to the case of the infinite cylinder. Due to the complexities in the flow behaviour behind the finite cylinder, there are only a limited number of investigations on the flow around *groups* of two finite circular cylinders (e.g., Taniguchi et al., 1981; Rooney et al., 1995; Park and Lee, 2003).

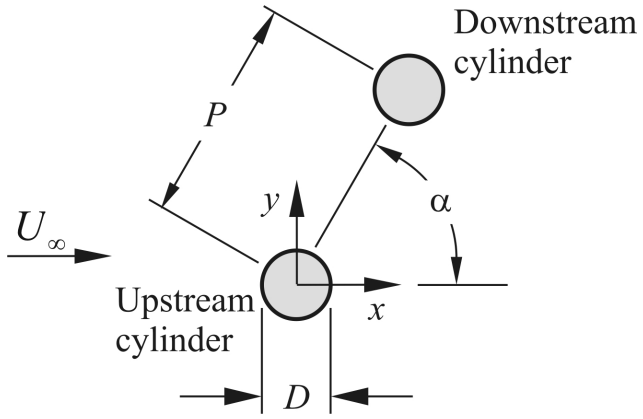

Figure 1.5. Staggered configuration of two circular cylinders of equal diameter in steady cross-flow, where x is the streamwise coordinate, y is the cross-stream coordinate, P is the centre-to-centre pitch (or spacing), and α is the incidence angle.

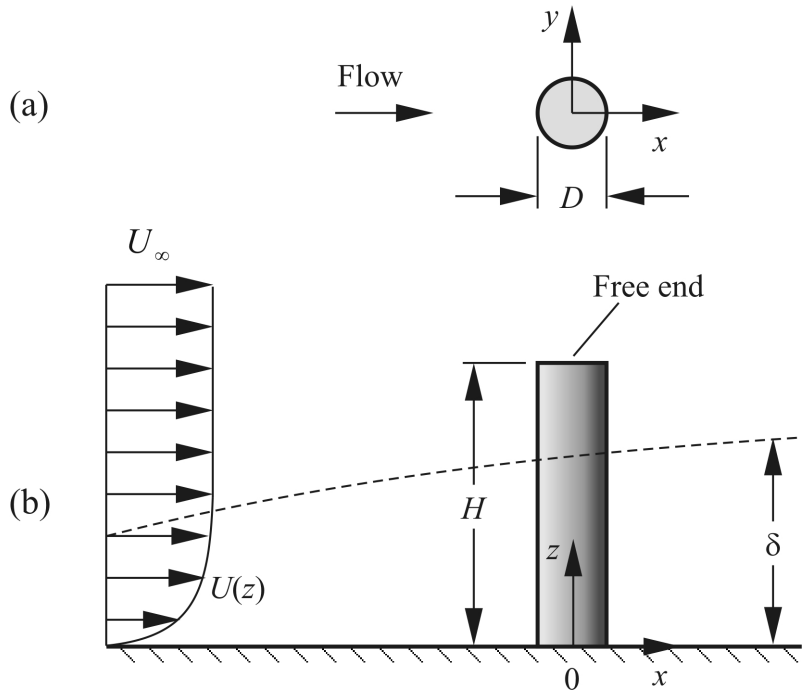

Figure 1.6. Circular cylinder of finite height mounted normal to a ground plane and partially immersed in a flat-plate boundary layer: (a) top view; (b) side view.

1.2 Objectives

The major objective of this research is to study and better understand Kármán vortex shedding from two staggered finite circular cylinders, and specifically how the Strouhal numbers depend on P/D and α, i.e., to determine St = f(P/D, α). The characteristics of the vortex shedding frequencies behind the two finite circular cylinders, with different combinations of P/D and α, are to be investigated through analyzing experimental results from low-speed wind tunnel experiments (measurements of the vortex shedding frequencies in the wakes of the finite circular cylinders from hot-wire anemometry) and then by comparing the results to those of two staggered infinite circular cylinders (using the data from Sumner et al. (2005)). In addition, the experimental data

will be used to study the effect of base and free end on the vortex shedding along the height of each of the two circular cylinders.

1.3 Outline of Thesis

The fundamentals of vortex shedding from a circular cylinder and the previous research work related to an isolated circular cylinder and groups of circular cylinders in cross-flow are reviewed in Chapter 2. In Chapter 3, the experimental apparatus and instrumentation are described. In Chapter 4, the main results and experimental data are presented and discussed, including vortex shedding from a single finite circular cylinder and vortex shedding from two staggered finite circular cylinders. The latter is discussed from two points of view, focusing first on vortex shedding from the *mid-height* of the circular cylinders and, second, focusing on vortex shedding *along the height* of the circular cylinders. Wake measurements behind the two finite circular cylinders at selected configurations are then presented to help understand the velocity field and to interpret some of the vortex-shedding data. Conclusions and recommendations are presented in Chapter 5.

CHAPTER 2

LITERATURE REVIEW

2.1 Introduction

In order to fully understand the flow behavior around an isolated circular cylinder or groups of circular cylinders, a wide range of experimental and numerical studies have been conducted to measure the various flow parameters, including Strouhal numbers, mean and fluctuating lift and drag force coefficients, the pressure distributions on the cylinder surfaces, the locations of the separation points, the velocity fields in the wakes, and the vortex formation lengths behind the circular cylinders. In this chapter, some previous and current experimental results for a single circular cylinder and groups of circular cylinders are reviewed. First, the characteristics of the vortex shedding behind a single infinite circular cylinder in cross-flow are presented. Then the flow structure around a single *finite* circular cylinder is described. Vortex shedding from two staggered infinite circular cylinders is discussed in the third part. The focus in the fourth part is on the previous research studies of flow around two staggered *finite* circular cylinders.

2.2 Single Infinite Circular Cylinder

Before discussing the flow around a finite circular cylinder or a group of cylinders, it is worthwhile to present a brief review of flow around a single isolated infinite cylinder. An infinite cylinder refers to the cylinder whose height (or length) is sufficient for the

flow field to be considered two-dimensional over a significant portion of its height. The flow over this portion is not affected by the end boundary conditions. Many authors, including Coutanceau and Defaye (1991), Szepessy (1991), Williamson (1996), Sumer and Fredsoe (1997), and Zdravkovich (1997), have reviewed and summarized the development of the flow around a single infinite cylinder in steady cross flow. The flow behaviour can be divided into flow regimes according to the Reynolds number based on the cylinder diameter and defined as $\mathrm{Re}_D = \rho_\infty U_\infty D/\mu_\infty$, where ρ_∞ is the freestream density and μ_∞ is the freestream dynamic viscosity.

In the creeping flow regime, where $\mathrm{Re}_D < 5$, the flow structure is symmetrical on the front side and back side of the cylinder (Fig. 2.1).

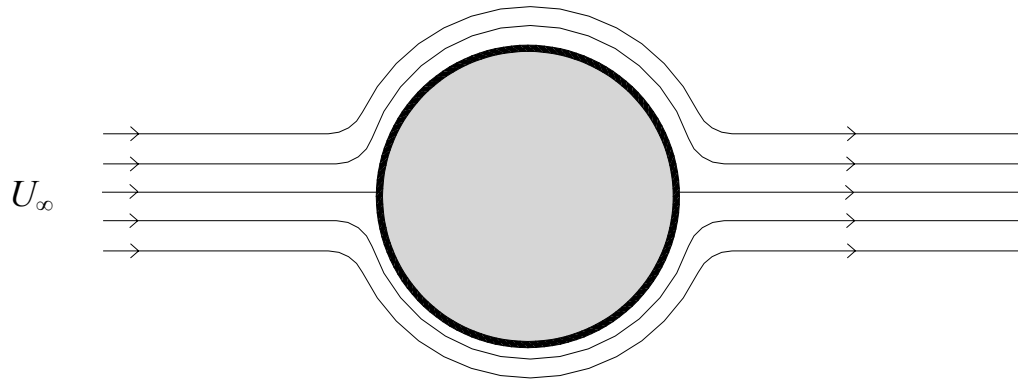

Figure 2.1. Creeping flow regime for $\mathrm{Re}_D < 5$.

As Re_D is increased beyond 5, the flow begins to separate at the rear stagnation point and the flow pattern changes to the steady twin vortex regime where two steady symmetric vortices are formed behind the cylinder. These vortices grow in size with

increasing Re_D (Fig. 2.2). Williamson (1996) combined the creeping flow regime and steady twin vortex regime into one regime and named it the laminar steady regime. On the other hand, Coutanceau and Defaye (1991) subdivided the flow into four regimes according to the various flow states before laminar vortex shedding begins.

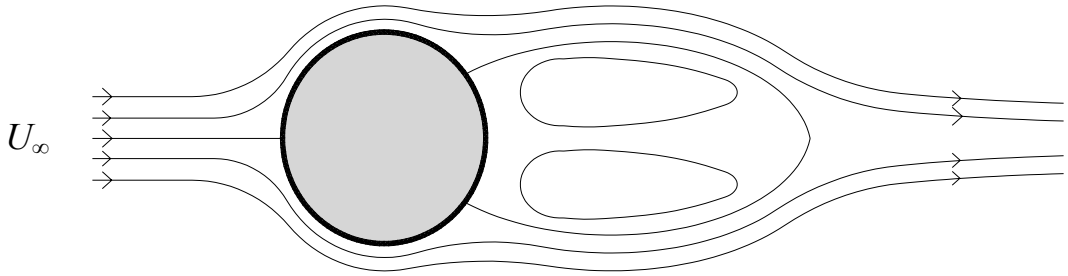

Figure 2.2. Steady twin vortex regime for $5 < Re_D < 40$.

When the Re_D is further increased beyond 40, oscillations begin to occur at the end of the recirculation region and increase in strength and amplification with increasing Re_D. As the instabilities increase in strength, they break the balance between the two attached vortices, strengthening one vortex and weakening the other so that the large one can break up from the recirculation region and be shed downstream into the wake. Then, the small vortex becomes larger and a new vortex is formed on the other side. This process represents the familiar periodic alternate vortex formation and shedding process, known as Kármán vortex shedding, which is observed for a wide range of Re_D (Fig. 2.3).

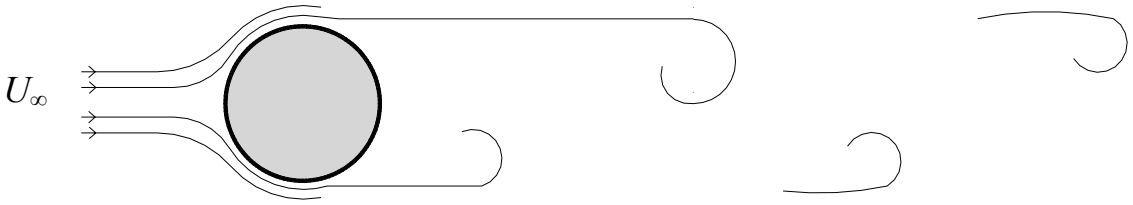

Figure 2.3. Laminar vortex shedding regime for $40 < Re_D < 150$.

With Re_D increasing beyond 150, the flow develops into an irregular vortex shedding regime where the separated shear layers transition to turbulence before roll-up into Kármán vortices. This leads to turbulent fluctuations of the wake (Fig. 2.4).

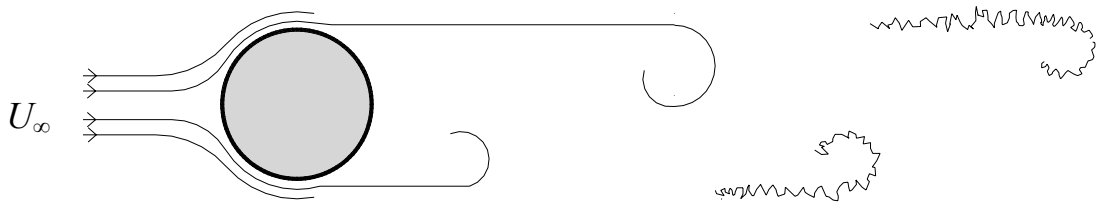

Figure 2.4. Irregular vortex shedding regime at $150 < Re_D < 350$.

As Re_D continues to increase into the lower subcritical regime, the transition point of the shear layer from laminar to turbulent flow moves even closer to the cylinder (Fig. 2.5). The transition of the flow state with increasing Re_D continues to be seen for $Re_D < 4 \times 10^4$, after which the flow is generally independent of Re_D until $Re_D = 2 \times 10^5$, which marks the end of the subcritical regime. Williamson (1996) identifies two flow regimes

within this range of Re_D, namely a regime with increasing disorder in the fine-scale three-dimensionalities, and a shear-layer transition regime.

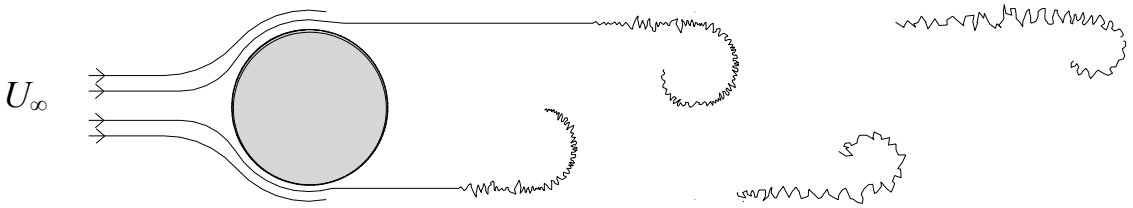

Figure 2.5. Lower subcritical regime at $350 < Re_D < 2\times10^5$.

As the flow enters the critical regime with Re_D between 2×10^5 and 7×10^5, the transition point comes close to the boundary layer separation point on the surface of the cylinder, causing the reattachment of separated flow back onto the cylinder surface after laminar separation (Fig. 2.6).

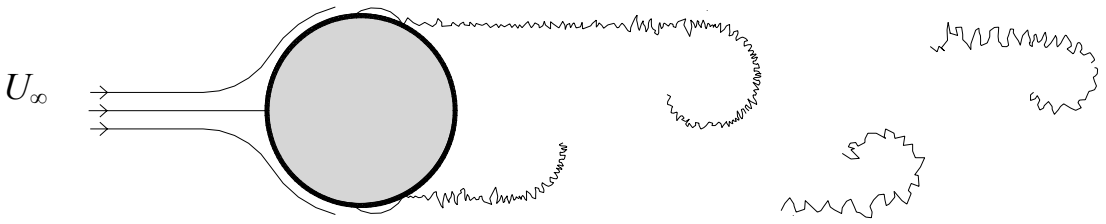

Figure 2.6. Critical regime for $2\times10^5 < Re_D < 7\times10^5$.

In the supercritical regime with Re_D between 7×10^5 and 3.5×10^6, the transition of the flow from laminar to turbulent takes place before boundary layer separation (Fig. 2.7).

As a result, the separation point moves backward to 120° from the front stagnation point, because the turbulent boundary layer can bear a larger adverse pressure gradient and therefore delay the onset of boundary layer separation.

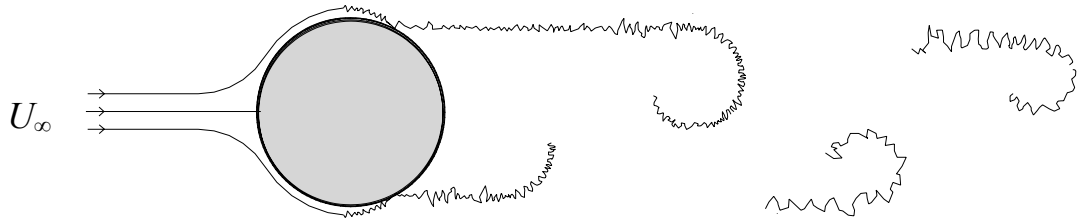

Figure 2.7. Supercritical regime for $7\times10^5 < \mathrm{Re}_D < 3.5\times10^6$.

Proceeding to the postcritical regime, the transition point keeps moving forward, causing the separation point to move along to the front surface of the cylinder. Coutanceau and Defaye (1991) named this regime the transcritical regime since they found that the transition from laminar to turbulent flow moved upstream of the laminar separation and the separation bubble, caused by the turbulent reattachment, disappeared in this Re_D regime. A noteworthy point is that the flow around the engineering structures shown in Figs. 1.1 to 1.4 lie mostly within the critical to postcritical regimes.

2.3 Single Finite Circular Cylinder

As shown in Fig. 2.8, the flow structure around a finite circular cylinder is strongly three-dimensional and more complicated compared to an infinite circular cylinder. For the finite circular cylinder, the flow over the free end and the flow around

the base (cylinder-wall junction) contribute to strong three-dimensionality of the flow field (Park and Lee, 2000, 2003). The tip flow can interact with the regular Kármán vortex shedding, which may suppress the vortex shedding process (for small-aspect-ratio cylinders) or even change the vortex shedding frequency (or Strouhal number).

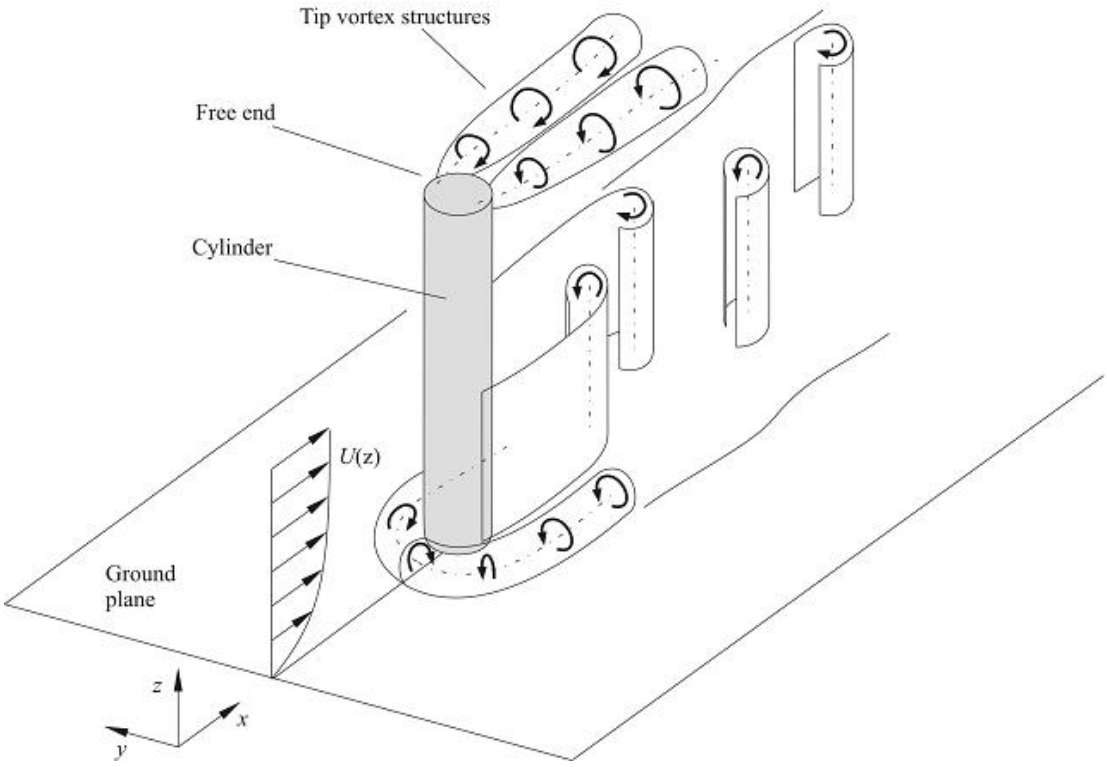

Figure 2.8. Flow around a single finite circular cylinder.

Okamoto and Yagita (1973) used wind tunnel experiments to investigate the characteristics of vortex shedding behind a single finite circular cylinder in cross-flow. The aspect ratio of the finite cylinder was changed from AR = 1 to 12.5 and the Reynolds number was in the range of $1.7\times10^3 \le \mathrm{Re}_D \le 1.5\times10^4$. When the aspect ratio was less than 6, no vortex street occurred behind the cylinder. Their experimental results also

revealed that the vortex shedding frequency decreased along the height of the cylinder from base to the free end for cylinders with AR > 7.

Okamoto and Sunabashiri (1992) studied aspect ratio effects on the flow structure around a single finite circular cylinder with AR = 0.5, 1, 2, 4, 7 and 23.75, and at Re_D = $2.5\times10^4 - 4.7\times10^4$. They reported that the cylinders with AR = 1 and 2 shed the vortices symmetrically; this changed to anti-symmetric vortex shedding as AR increased to 4 – 7. The vortex shedding frequency decreased with increasing AR in the symmetric vortex shedding region and reached a minimum value at AR = 3 – 4. After that, the vortex shedding frequency changed to increase at higher AR. They also found that the recirculation region behind the cylinder kept enlarging with increasing AR, but the length of the recirculation region reached a maximum value near AR = 4 and then changed to decrease as AR further increased. The effects of the horseshoe vortex and the downwash flow from the free end were weakened as the AR increased.

Rooney et al. (1995) measured the vortex shedding frequency behind single finite circular cylinders with AR = 2, 4.67, 7.33, 9.33 and 10.67. Their Reynolds numbers were in the range of $7.3\times10^3 \leq Re_D \leq 2.0\times10^4$. From their experimental results, Rooney et al. (1995) reported that the Strouhal number increased with AR in the range of $5.33 \leq AR \leq 11.33$. For the range $0.67 \leq AR \leq 5.33$, the Strouhal number increased at first and then decreased. Besides, the strength of the vortices shed from a cylinder also seemed to be related to the AR. In the range of $0.67 \leq AR \leq 2$ and $5.33 \leq AR \leq 7.33$, the peaks of the

power spectra turned out to be weak, but for $2.67 \leq AR \leq 4.67$, and $AR > 7.33$, sharp and strong peaks were detected behind the cylinder. Another notable point they mentioned was a sudden drop in the vortex shedding frequency taking place around the height $z/H = 0.6$ for the high-AR cylinders. The low frequency near the free end was called the "free end frequency", and remained constant regardless of AR. This free end frequency was also observed by Farivar (1981), Zdravkovich et al. (1989) and Park and Lee (2000).

Luo et al. (1996) carried out measurements on flow behavior around a single finite circular cylinder by measuring the pressure distribution on the surface of the cylinder. Three finite cylinders with different aspect ratios of AR = 4, 6 and 8 were chosen for their experiments at $Re_D = 3.33 \times 10^4$. The results suggested that the local aerodynamic force was highly dependent on vertical location along the height of the finite cylinder, in particular for the region near the free end. Besides, the downwash flow from the free end elongated the vortex formation region and created a less negative wake pressure, resulting in a decrease in the mean drag force on the cylinder. It was also found that the free end effect could extend to the whole cylinder for the low-AR cylinders and only affect the upper part of the cylinders with high AR.

Park and Lee (2000) investigated the free end effect on the near wake flow structure behind a finite circular cylinder by measuring the wake velocity and the pressure distribution on the cylinder surface. Wind tunnel experiments were conducted at $Re_D = 2.0 \times 10^4$ and three finite cylinders with different aspect ratios of AR = 6, 10 and 13 were tested. Flow visualization was also carried out in a water tunnel to observe the flow

structure around the cylinder. Based on the experimental data, Park and Lee (2000) pointed out that the strong downwash flow induced by the counter-rotating twin vortices trailing the free end led to the formation of a three-dimensional wake. They also discovered that as AR was reduced, the vortex formation region behind the single finite cylinder enlarged and the associated vortex shedding frequency decreased. Investigation of the free end effect on the near wake structure showed that there was no periodic vortex shedding near the free end due to the interaction between the downwash flow and the vortices shed from the two sides of the cylinder. Another notable point brought up in their work was that a 24-Hz frequency component was detected near the free end, which seemed to be closely related to the counter-rotating vortices generated at the free end.

Sumner et al. (2004) measured the wake velocity and streamwise vorticity fields behind finite circular cylinders with AR = 3, 5, 7 and 9 in a wind tunnel at $Re_D = 6\times10^4$. They observed a counter-rotating vortex pair near the free end, which caused the downwash flow, and another pair of vortices near the base of the cylinder, which induced the upwash flow. An aspect ratio effect on the flow structure was also observed, that the base vortices were absent for a finite cylinder with low AR, corresponding to a completely different flow structure from those cylinders with high AR. In addition, no vortex shedding was measured along the height of a finite cylinder with low AR, indicating that Kármán vortex shedding was replaced by arch vortex shedding (Okamoto and Sunabashiri 1992; Taniguchi et al. 1981).

Adaramola et al. (2006) studied the turbulent wake structure of a single finite

circular cylinder with small aspect ratios of AR = 3, 5, 7 and 9 in a wind tunnel, at Re_D = 6×10^4. The experimental data showed that the cylinders with AR = 5, 7 and 9 had a similar wake structure, with a downwash velocity field between the tip vortices and upwash between base vortex structures, while the wake structure behind the cylinder with AR = 3 showed the absence of the base vortex structures and the associated upwash flow.

Lee et al. (2007) used large-eddy simulation (LES) to examine the flow characteristics of single finite circular cylinders with AR = 2.5 and 10 in order to understand the flow structure of a tripod tower. They reported that the downwash flow from a high-AR cylinder is much stronger than for a low-AR cylinder, and the vortex shedding from the upper region of the long cylinder is not in phase with that of the lower region.

Donnert et al. (2007) used flow visualization and concentration measurements to investigate the mass transfer in the flow around single finite circular cylinders with AR = 2.5 and 5.0. Their experiments were conducted in a water tunnel at $Re_D = 4.4\times10^4$ and 2.2×10^4. Their results confirmed the previous findings about the characteristics of the flow structure around a single finite cylinder.

Afgan et al. (2007) used LES to study the flow around single finite circular cylinders with AR = 6 and 10 at Re_D = 20,000. The simulation results further demonstrated the effects of cylinder tip and base on the flow structure around the single finite cylinder.

2.4 Groups of Two Infinite Circular Cylinders

Previous studies of two staggered infinite circular cylinders in cross-flow (Fig 1.5) have revealed that complex wake and proximity interference effects can occur. Various combinations of the centre-to-centre pitch ratio, P/D, and angle of incidence, α, which are the primary influencing parameters, are able to result in very different flow patterns. When $\alpha = 0°$, the cylinders are arranged in an inline or tandem configuration. When $\alpha = 90°$, the cylinders are arranged in a side-by-side configuration.

2.4.1 Two Tandem Infinite Circular Cylinders

Igarashi (1981) used a wind tunnel to study the flow around two circular cylinders in tandem for $P/D = 1.03$ to 5 and Reynolds numbers in the range of $8.7\times10^3 \le Re_D \le 5.2\times10^4$. Based on the experimental data, he classified seven flow patterns associated with the different pitch ratios and Reynolds numbers, and described the characteristics of each flow pattern. Igarashi (1981) also investigated how the Strouhal numbers and pressure distributions varied with P/D and Re_D. Later, in his second report, Igarashi (1984) focused on the study of the three flow patterns occurring only at small P/D, including flow without reattachment, unstable flow, and "unique" flow. His experiments were conducted in a low speed wind tunnel with $1.15\times10^4 \le Re_D \le 1.03\times10^5$ and $P/D = 1$ to 1.5. The results showed that the flow patterns varied considerably with Re_D.

Ljungkrona et al. (1991) investigated the effects of the freestream turbulence and P/D on the flow behavior around two infinite cylinders arranged in tandem. The two

cylinders were placed at pitch ratios from P/D = 1.25 to 5 and $Re_D = 2.0\times10^4$. The results of the experimental investigation revealed that the effect of turbulence on the flow structure around two cylinders inline was highly dependent on P/D. For $P/D \leq 2$, the turbulence seemed to have strong influence on the flow patterns around the cylinders and further affected the drag coefficient and vortex shedding frequency. But in the range of $2 \leq P/D \leq 5$, no clear influence of the turbulence was seen when the turbulence intensity was varied.

Ljungkrona and Sunden (1993) made flow visualization in the wind tunnel at $Re_D = 3.3\times10^3$ to12×10^3 for two cylinders in an inline arrangement with pitch ratios in the range of $1.25 \leq P/D \leq 4.0$, and studied how the flow pattern changed with the different pitch ratios and Reynolds numbers. The flow visualization results suggested that the flow pattern was highly dependent on P/D and Re_D, and this conclusion was also confirmed by the measurements of pressure distribution on the surfaces of the cylinders.

2.4.2 Two Side-by-Side Infinite Circular Cylinders

Sumner et al. (1999) investigated the flow behavior around two circular cylinders arranged in the side-by-side configuration using flow visualization, thermal anemometry, and PIV. The pitch ratio was varied from P/D = 1 to 4 and the Reynolds number was varied from Re_D = 500 to 3000. In their work, three flow patterns were defined: single bluff-body vortex shedding at small P/D, biased flow at intermediate P/D (from P/D = 1.25 to 2) and synchronized vortex shedding from the two cylinders at large P/D.

Xu et al. (2003) used laser-induced fluorescence flow visualization, PIV and hot-wire techniques to investigate Reynolds number effects on the flow structure of two side-by-side circular cylinders arranged from P/D = 1 to 1.7. The Reynolds number based on the cylinder diameter was in the range of Re_D = 150 to 1000. They reported that for $P/D \leq 1.25$, only one frequency was detected behind the two cylinders and it seemed to be independent of Re_D. As P/D increased to $1.25 \leq P/D \leq 1.6$, the same single dominant frequency was still found at lower Re_D, however, another high frequency occurred at a higher Re_D, implying that the increase in the Re_D made the flow patterns change. When $P/D \geq 1.6$, Re_D had no further effect on the vortex shedding frequency and thus there were always two frequencies detected. The flow visualization further showed that there was only one vortex street behind the two cylinders at lower Re_D while at higher Re_D a two-street flow structure was observed.

2.4.3 Two Staggered Infinite Circular Cylinders

Gu and Sun (1999) investigated the flow characteristics of two infinite circular cylinders arranged in staggered configurations in a wind tunnel at $Re_D = 2.2\times10^5 - 3.3\times10^5$ where the pitch ratio was varied from P/D = 1.1 to 3. Based on their experimental data, Gu and Sun (1999) classified the flow patterns into three types, namely wake interference, shear layer interference, and neighborhood interference.

Sumner et al. (2000) further revealed a wider range of flow patterns for two staggered infinite circular cylinders in cross-flow, through the use of flow visualization,

thermal anemometry and PIV, at Re_D = 850 to 1900. The cylinders were arranged at pitch ratios of P/D = 1 to 4 and incidence angles from α = 0° to 90°. Nine flow patterns were identified, including single bluff-body flow pattern 1 and 2 (SBB1 and SBB2); base-bleed flow pattern (BB), where the narrow gap between two circular cylinders placed at very small pitch ratios permits a base-bleed flow to occur; shear layer reattachment flow pattern (SLR), where the flow through the gap between the two circular cylinders is prevented by the formation of a separated shear layer from the inside surface of the upstream cylinder; induced separation flow pattern (IS), where the vortex from the upstream cylinder induces flow separation on the downstream cylinder when it forms close to the downstream cylinder; synchronized vortex shedding flow pattern (SVS) where the flow through the gap between the two cylinders is deflected away from the flow axis, resulting in two different near-wake regions behind two cylinders; vortex impingement flow pattern (VI), where either one or two rows of vortices from the upstream cylinder impinge on the downstream cylinder; and vortex splitting, pairing and enveloping flow patterns (VPE, VPSE), where a counter-rotating vortex pair is found at the exit of the gap between two circular cylinders, and the vortex pair is then split or enveloped by a Kármán vortex from outer shear layer of the upstream cylinder.

Akbari and Price (2005) used a numerical simulation to study the flow patterns around two staggered circular cylinders in cross-flow at Re_D = 800 and identified five flow patterns identified by Sumner et al. (2000), including the shear layer reattachment flow pattern, the vortex pairing and enveloping flow pattern, the vortex impingement

flow pattern, and flow patterns involving Kármán vortex shedding from both cylinders.

Sumner et al. (2005) measured the mean aerodynamic forces and vortex shedding frequencies for two staggered infinite circular cylinders, for P/D = 1.125 to 4.0 and α = 0° to 90°. The Reynolds number based on the cylinder diameter was in the range of Re_D = 3.2×10^4 to 7.2×10^4. They classified the staggered configurations by the pitch ratio into closely spaced staggered configurations (P/D < 1.5), moderately spaced staggered configurations ($1.5 \le P/D \le 2.5$), and widely spaced staggered configurations ($P/D > 2.5$), according to the behaviour of the mean aerodynamic forces and the Strouhal numbers (see Fig. 2.9).

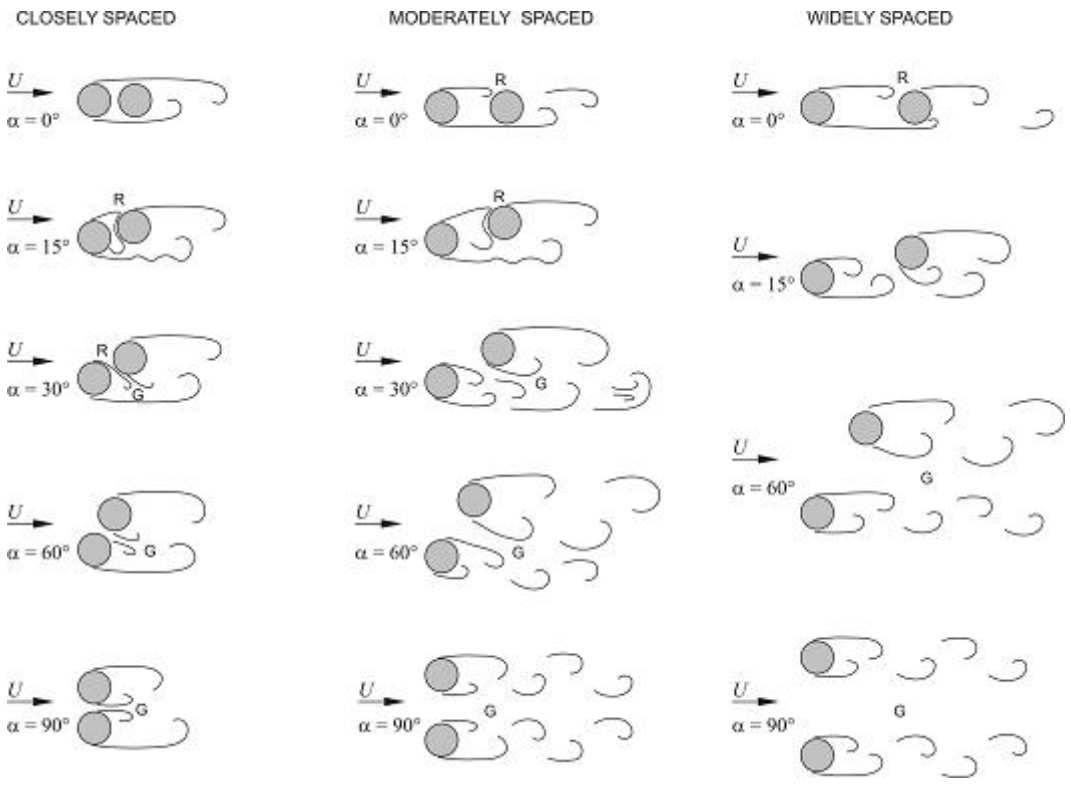

Figure 2.9. Overview of flow patterns for two staggered infinite circular cylinders of equal diameter in steady cross-flow (from Sumner et al. (2000, 2005)).

2.5 Groups of Two Finite Circular Cylinders

There are several studies in the literature that focus on the flow around small groups of finite circular cylinders. These are grouped into tandem, side-by-side and staggered configurations in the following sub-sections.

2.5.1 Two Tandem Finite Circular Cylinders

Luo et al. (1996) carried out an investigation of the flow around two finite circular cylinders in a tandem arrangement by measuring the pressure distributions on the surfaces of the cylinders. Cylinders with different aspect ratios, of AR = 4, 6 and 8, were arranged in tandem at pitch ratios of P/D = 1, 1.64, 3 and 5, at a Reynolds number of about $Re_D = 3.33\times10^4$. Luo et al. (1996) reported that the flow structure of the two tandem finite circular cylinders was different from that of two tandem infinite circular cylinders, and the flow pattern could vary along the height of the finite cylinder. At small P/D, reattached flow was detected both near the free end and the base of the cylinder due to the influence of the downwash flow and the horseshoe vortex, while a distinct wake structure was found at the middle section behind the cylinder. A similar situation happened for intermediate P/D, but in this case, reattached flow occurred at the middle section of the cylinder whereas co-shedding flow was found near the free end.

Palau-Salvador et al. (2007) used LES to model the flow structure around two finite circular cylinders of AR = 2.5 arranged in tandem at $Re_D = 1500$ with $P/D = 2$. At this pitch ratio, the flow structure showed the characteristics of the reattachment flow

pattern with no vortex shedding in the gap between the two cylinders. A strong downward flow was detected in the gap which induced the flow from the top of the cylinders to fill the wake behind the upstream cylinder. The flow behind the downstream cylinder was complicated and different from the flow structure behind a single finite cylinder.

2.5.2 Two Side-by-Side Finite Circular Cylinders

Park and Lee (2003) investigated the flow structure around two finite circular cylinders of AR = 6 arranged in the side-by-side configuration using flow visualization and hot-wire anemometry in a wind tunnel at $Re_D = 2\times10^4$. The pitch ratio was in the range of $1 \le P/D \le 2$. From their experimental results, they discovered that the two cylinders behaved like a single bluff-body when in contact (at $P/D = 1$). For $P/D > 1.25$, the flow passing through the gap between the two cylinders became stronger and interacted with the shear layers shed from the two cylinders, forming the biased flow pattern. When the two side-by-side cylinders were arranged at $P/D = 2$, there was no interaction between the two inner shear layers shed from the two cylinders and the biased flow pattern was replaced by a symmetric shedding flow pattern behind the two cylinders. Also, the vortex formation region behind each cylinder became smaller when the gap flow became stronger.

Liu and Cui (2006) applied the Multiple Relaxation Time lattice Boltzmann method to the study of two finite cylinders in side-by-side configuration. They demonstrated the effects of the free end and pitch ratio on the interference between the

two side-by-side cylinders.

2.5.3 Two Staggered Finite Circular Cylinders

There are several studies in the literature of the flow around two finite circular cylinders in a staggered configuration. One of the earlier studies, by Zdravkovich (1979), measured the pressure distribution along the height of two staggered circular cylinders of AR = 4.6 in cross-flow at selected pitch ratios and incidence angles. They also studied the free end effect on the flow structure.

Sarode et al. (1981) investigated the aerodynamic forces acting on a single finite circular cylinder of AR = 1 to 10, and also two finite circular cylinders, at $Re_D = 2.2\times10^4$. The two finite cylinders were arranged in tandem and side-by-side configurations only, at P/D = 1 to 8. For two cylinders arranged in tandem, the drag force on the downstream cylinder highly depended on P/D and was considerably less than the case of a single finite cylinder. For the side-by-side configuration, the drag force on each of the cylinders was quite similar to that of the single finite cylinder for $P/D > 2$.

Taniguchi et al. (1982) investigated the interference between two staggered finite circular cylinders in cross-flow at selected P/D and α by measuring the pressure distribution on the cylinders' surfaces. Two identical finite circular cylinders with AR = 3 were arranged in staggered configurations in a wind tunnel at Re_D = 14,192. Based on the behavior of the mean drag and lift coefficients, the flow pattern was broadly divided into three regimes based on incidence angle: $0° \le \alpha \le 30°$, $30° \le \alpha \le 120°$, and $120° \le \alpha \le$

180°. When $P/D \geq 4.0$ and $0° \leq \alpha \leq 120°$, the time-averaged aerodynamic forces on the two cylinders were similar to the case of a single finite cylinder, indicating the interference between the two cylinders was fairly small at those configurations.

Kareem et al. (1996) investigated the interference effect on two finite circular cylinders of AR = 10 in cross-flow by measuring the aerodynamic forces on the upstream and downstream cylinders. Measurements were made for staggered configurations of P/D = 2, 3, 4, 5, 6 and 7, and incidence angles of α = 0°, 10°, 20°, 30°, 40°and 90°. They found that for smaller pitch ratios, $P/D < 3$, the vortex shedding from both cylinders was weakened. When the downstream cylinder was located at $P/D > 3$, the vortex shedding from the downstream cylinder was enhanced, while the upstream cylinder was hardly affected.

Kronke and Sockel (2007) measured the aerodynamic forces on two staggered finite cylinders in a wind tunnel at $Re_D = 4\times10^4$. They investigated pitch ratios of P/D = 1.5, 2, 3 and 5, and incidence angles between –7.5° and 30°. Their results showed a negative peak was measured for lift coefficient at a critical angle between 7.5° and 12.5° when the two cylinders were arranged at P/D = 1.5 and 2, and a minimum drag coefficient was detected at the same configurations, which was similar to the inner lift peak and minimum drag coefficient for two staggered infinite cylinders found by Sumner et al. (2005). Kronke and Sockel (2007) further demonstrated that elevated freestream turbulence intensity was able to reduce the interference between the two cylinders.

CHAPTER 3
EXPERIMENTAL APPARATUS AND INSTRUMENTATION

3.1 Introduction

All the experiments in this research were conducted in the University of Saskatchewan's low-speed, closed-return wind tunnel. Detailed information about the wind tunnel facility is presented in Section 3.2. The cylinder models used in the research and the experimental set-up are described next in Section 3.3. A description of the instrumentation is given in Section 3.4, including the Pitot probe, the hot-wire anemometry system and the seven-hole pressure probe. Section 3.5 discusses the establishment and assessment of the flat-plate boundary layer in the wind tunnel. Section 3.6 contains a summary of the measurement uncertainty associated with the experiments.

3.2 Wind Tunnel

The closed-return low-speed wind tunnel at the University of Saskatchewan consists of five main components, including the variable-pitch fan, four corners with turning vanes, turbulence-reduction screens, the low-speed test section and the high-speed test section, as shown in Fig. 3.1. The airflow in the wind tunnel is driven by a 75-kW variable-pitch fan, as shown in Fig. 3.2. The fan pushes the air through the wind tunnel. Moving along the upper part of the tunnel (the return passage, Fig. 3.1), the

airflow reaches the first two corners where the flow turns by 180°. A pair of turbulence-reduction screens is located at the start of the lower part of the tunnel (Fig. 3.1) and is used to reduce the turbulence intensity in the freestream. Then the air flows into the low-speed test section. Upon exiting the low-speed test section, the flow passes through a 7:1 contraction where the freestream increases its speed before entering the high-speed test section (with dimensions of 0.91 m (height) × 1.13 m (width) × 1.96 m (length)) where the experimental apparatus was installed (shown in Fig. 3.3). The two sidewalls of the test section are made of Plexiglas so that the experimental apparatus in the test section is visible. The speed of the airflow in the high-speed test section can be varied from U_∞ = 5 to 50 m/s. A freestream velocity of U_∞ = 20 m/s was chosen for this research (to ensure the cylinder Reynolds number was consistent with previous experiments). After passing the high-speed test section, the airflow enters the diffuser (Fig. 3.1) and returns to the fan.

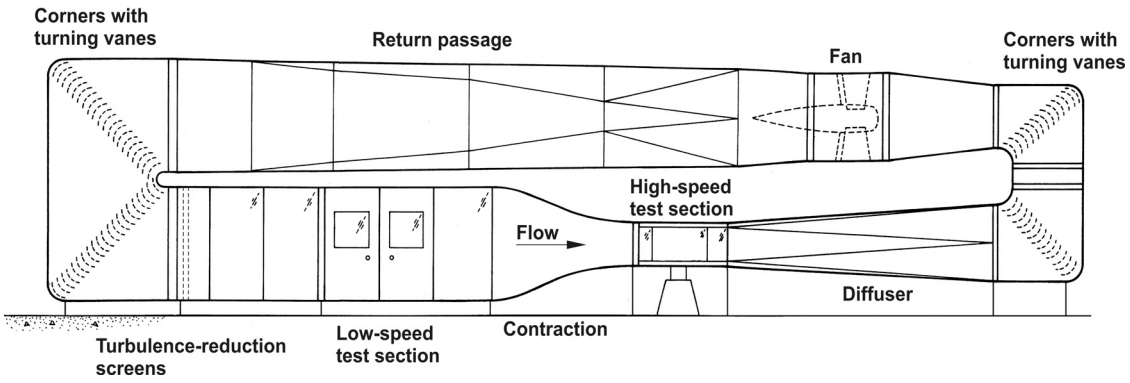

Figure 3.1. The University of Saskatchewan's low-speed wind tunnel.

Figure 3.2. Variable-pitch fan in the upper, return passage of the wind tunnel.

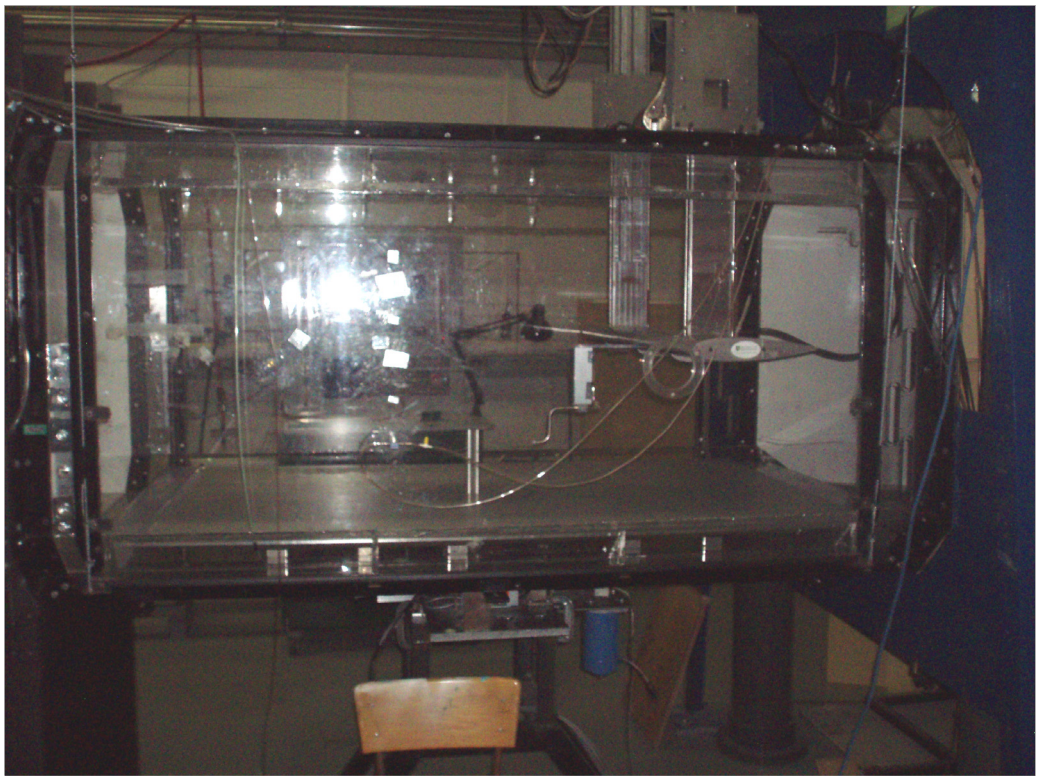

Figure 3.3. High-speed test section of the wind tunnel (flow from left to right).

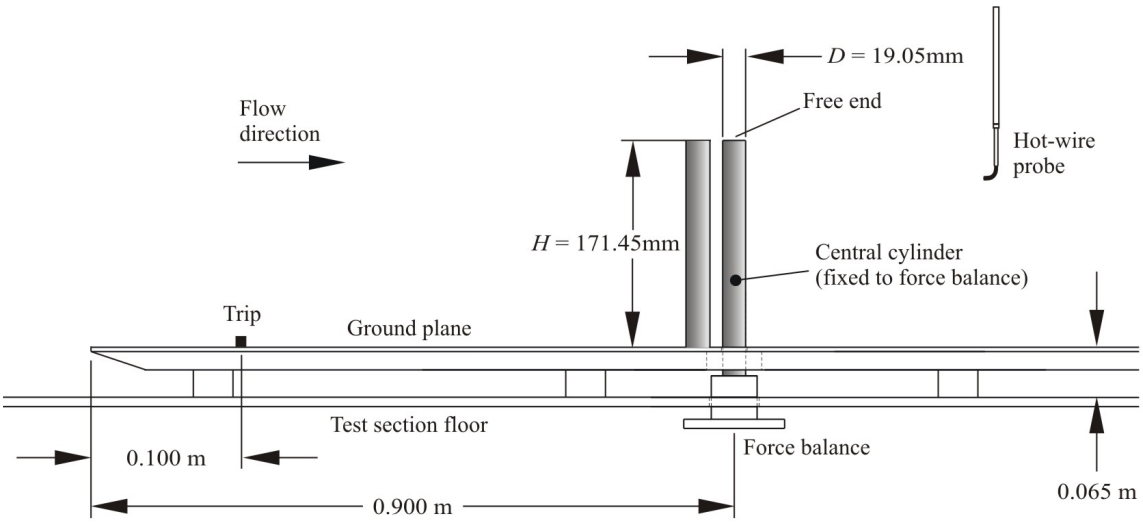

Figure 3.4. Experiment set-up in the wind tunnel for two staggered finite circular cylinders, showing a X-probe hot-wire probe in the wake of the cylinders.

A smooth flat ground plate was installed near the test-section floor (Fig. 3.4) and a special leading edge with the shape of a super-ellipse was designed for the flat plate to minimize the chances of flow separation near the junction of the nosepiece and the plate (Narasimha and Prasad, 1994). A trip was installed downstream of the leading edge of the ground plane (Fig. 3.4), to produce a thick turbulent flat-plate boundary layer at the location of the cylinders. This is discussed further in Section 3.5.

As shown in the Fig. 3.5, a traversing wing, which is controlled by a three-axis computer-controlled traversing system (discussed further in Section 3.4), is used to hold a measuring probe and change the probe's location.

Figure 3.5. The traversing wing in the test section, with a seven-hole probe (Section 3.4.3) mounted in the probe holder. Also shown are the two finite circular cylinders and the turntable (Section 3.3) embedded in the ground plane.

3.3 Cylinder Model and Experimental Setup

Two identical circular cylinders of H = 171.45 mm, D = 19.1 mm, and AR = 9, were arranged in staggered configurations in the test-section (Fig. 3.4). The cylinders were made of aluminum and had a smooth finish. The cylinders' dimensions were chosen to be consistent with previous work reported by Sumner et al. (2004) and Adaramola et al. (2006). The first cylinder, known as the central cylinder, was mounted vertically from a six-component force balance located outside and below the wind tunnel test-section. This cylinder was centrally located in the test-section. The second cylinder, known as the outer cylinder, was mounted onto the turntable shown in Fig. 3.6. The turntable embedded in the ground plane is driven by a timing belt, stepping motor, and

microstep driver. There is small gap reserved between the central cylinder and turntable to avoid resistance when the turntable is moving. Rotation of the turntable made the angle of incidence vary from 0° to 180° at an interval of 1°. In this way, the central cylinder could represent either an upstream or downstream cylinder (Fig. 1.5) over the full range of incidence angle. An incidence increment of 1° and 2° was used, depending on the region of interest. The pitch ratios, P/D = 1.125, 1.25, 1.5, 2, 2.5, 3, 4, and 5, were used in the experiments; a set of mounting holes in the turntable allowed the outer cylinder to be located at different positions giving the above pitch ratios.

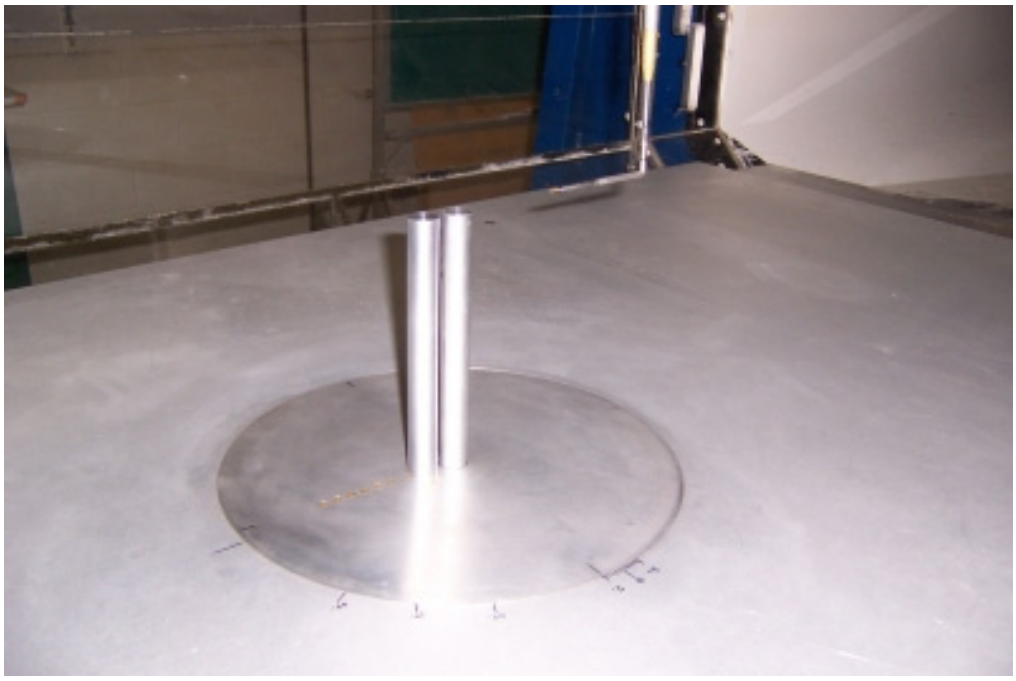

Figure 3.6. Two staggered finite circular cylinders in the test section, showing the turntable embedded in the ground plane. Here, the cylinders are positioned at P/D = 1.125 and the angle of incidence is α = 5°. A single-sensor hot-wire probe (Section 3.4.2) is mounted in the probe holder.

3.4 Instrumentation

Most of the experimental data were acquired with a Pentium 4 computer running Windows XP Professional, a National Instruments PCI-6031E 16-bit multifunction board and LabVIEW software. The board was equipped with a 16-bit A/D converter, 64 analog input channels configured in differential mode, and was capable of sampling at 100,000 samples per second. A second 16-bit multifunction board was also installed in the computer; this National Instruments PCI-6034E data acquisition board was interfaced with a National Instruments SCXI chassis and was dedicated to signals coming from a Scanivalve ZOC-17 pressure scanner. The three-axis traversing wing and the turntable were controlled by stepping motors operated through a National Instruments PCI-7344 four-axis motion controller card, a set of IMS microstep drivers, and the LabVIEW software.

3.4.1 Measurements of Pressure, Temperature, Density and Viscosity

The freestream dynamic pressure, q_∞, was measured with a Pitot-static probe (manufactured by United Sensor, 3.2-mm external diameter) and a Datametrics Barocel differential pressure transducer. The freestream dynamic pressure was obtained from the Pitot-static probe and the freestream velocity, U_∞, was calculated from Bernoulli's equation,

$$P_0 = P_\infty + q_\infty , \tag{3.1}$$

where,

$$q_\infty = \frac{1}{2}\rho_\infty U_\infty^2 \tag{3.2}$$

and P_0 is the stagnation pressure, P_∞ is the freestream static pressure, and ρ_∞ is the freestream air density. The static line from the Pitot-static probe was also connected to a Barocel absolute pressure transducer for measuring P_∞.

A modified United Sensor boundary layer Pitot probe (model BA-.025-12-C-11-.650) with an outer diameter of d_p = 0.60 mm, installed in the traversing wing, was used to measure the mean streamwise velocity profile of the boundary layer on the ground plane (Section 3.5). The boundary layer probe was connected to the positive side of a Validyne differential pressure transducer with the other side linked to the static port of the wall-mounted Pitot-static probe. The local streamwise velocity, u, was calculated based on the local stagnation pressure, P_0, obtained from the boundary layer probe.

All of the above pressures were sampled at a frequency of 500 Hz, and 10,000 samples were used to take average and obtain the time-averaged pressure value.

The freestream temperature, T_∞, was measured by an integrated-circuit-type electronic temperature sensor, and the freestream density, ρ_∞, was derived from the ideal gas equation,

$$P_\infty = \rho_\infty R T_\infty, \tag{3.3}$$

where R is the gas constant (for air R = 287.0 J/kg·K).

The freestream viscosity, μ_∞, was calculated through the Sutherland correlation,

$$\mu_\infty = \frac{bT_\infty^{3/2}}{S + T_\infty}, \tag{3.4}$$

where $b = 1.458\times10^{-6}$ kg/(m·s·K$^{1/2}$) and $S = 110.4$ K for air (White, 2003).

3.4.2 Hot-Wire Anemometer

The vortex shedding frequencies were measured with a TSI 1210-T1.5 single-component hot-wire probe which was connected to a TSI Intelligent Flow Analyzer (IFA)-100 constant-temperature anemometer (Fig. 3.7). The hot-wire anemometer can measure the instantaneous flow velocity (velocity-time signal) by providing electrical current to the hot-wire probe and keeping the wire at a constant temperature. The IFA-100 anemometer has three channels, which can receive voltage signals from three wires simultaneously.

Figure 3.7. Front panel of the TSI IFA-100 constant-temperature anemometer.

The TSI 1210-T1.5 single-component hot-wire probe possesses a tungsten wire coated with platinum. The wire has a diameter of 3.8 μm and a length of 1.27 mm. This single hot-wire probe was connected to the first channel of the IFA-100. The recommended operating resistance and bridge compensation were set on the IFA-100 as given by TSI. The velocity signal was sampled at 5,000 Hz and the sampling time was one second. A low-pass filter (on the IFA) was used to remove frequency content higher than 5 kHz. Power spectra were used to provide the information about how the power of the velocity signal is distributed with respect to frequency. The algorithm applied to calculate the spectra (within LabVIEW) from the velocity signals was based on the Fourier transform. The power spectra of the velocity signal fluctuations shown later in this thesis were the averaged results of 250 spectra measured by the hot-wire probe. The peaks in the power spectra correspond to the vortex shedding frequencies, which are identified automatically by the LabVIEW software. However, for some particular cases, the peaks in the power spectra had to be searched manually.

For the vortex shedding frequency measurements, the hot-wire probe was located behind the central cylinder at a fixed streamwise and cross-stream position, $x/D = 3$ and $y/D = 1$, with the wall-normal position allowed to change from $z/H = 0.05$ to 1.05 at an interval of $\Delta z/H = 0.05$ to measure the vortex shedding frequencies along the height of the cylinder. The outer cylinder was only rotated in the way by which the probe was always located outside the two cylinders. The single-wire probe was calibrated in the wind tunnel with a pitot-static probe (Section 3.4.1) as the velocity reference.

Twenty-four different velocities were used for the probe calibration. A fourth-order polynomial calibration curve was used and the expression was as follows,

$$U_\infty = c_1 + c_2 E + c_3 E^2 + c_4 E^3 + c_5 E^4 \tag{3.5}$$

where U_∞ is the mean velocity calculated through equations (3.1) and (3.2), c_1 to c_5 are calibration constants, and E is the voltage output from the anemometer.

A TSI model 1243-20 boundary layer X-probe was used for the boundary layer measurements. This probe has two sensing wires and was oriented to measure the streamwise velocity component, u, and the wall-normal velocity component, w. The probe was connected to two channels of the IFA-100. For each channel, the recommended operating resistance and bridge compensation were set on the IFA as given by TSI. The sensors of the X- probe were made of platinum wire with a diameter of 50.8 μm and 1.02 mm sensing length. The velocity signal was sampled at 10,000 Hz and the sampling time was ten seconds. The boundary layer X-probe was also calibrated with a Pitot-static probe (Section 3.4.1) and an automated variable-angle calibrator (Sumner, 2002). Nine different freestream velocities were applied in the wind tunnel test section for the calibration. The yaw angle of the probe, α, controlled by a stepping motor, was varied between – 32.4° and +32.4° at a constant increment of 8.1°. Each pair of U_∞ and α corresponded to a unique voltage pair (E_1, E_2) measured by the anemometer. Two, two-dimensional, third-order polynomial equations were used to express the relation between the voltage output and the flow velocity,

$$U_\infty = a_1 + a_2 x + a_3 y + a_4 x^2 + a_5 xy + a_6 y^2 + a_7 x^3 + a_8 x^2 y + a_9 xy^2 + a_{10} y^3 \qquad (3.6)$$

$$\tan\alpha = b_1 + b_2 x + b_3 y + b_4 x^2 + b_5 xy + b_6 y^2 + b_7 x^3 + b_8 x^2 y + b_9 xy^2 + b_{10} y^3 \qquad (3.7)$$

where $x = E_1 + E_2$, $y = E_1 - E_2$, a_1 to a_{10} and b_1 to b_{10} are calibration constants, and E_1 and E_2 are the voltage outputs from the anemometer. The streamwise velocity component, u, and wall-normal velocity component, w, were obtained from the equations as follows,

$$u = U_\infty \cos\alpha \qquad (3.8)$$

$$w = U_\infty \sin\alpha \qquad (3.9)$$

3.4.3 Seven-Hole Probe

The mean velocity field in the wake of the cylinders was measured with a conical-shaped seven-hole pressure probe with a cone angle of 30° and diameter of 3.45 mm. The probe has a central pressure port on the tip of the probe surrounded by six outer pressure ports, as shown in Fig. 3.8. Each of the pressure ports corresponds to one of seven close-packed 1-mm-diameter stainless steel tubes fitted into an outer stainless steel sleeve. The probe was manufactured at the University of Saskatchewan.

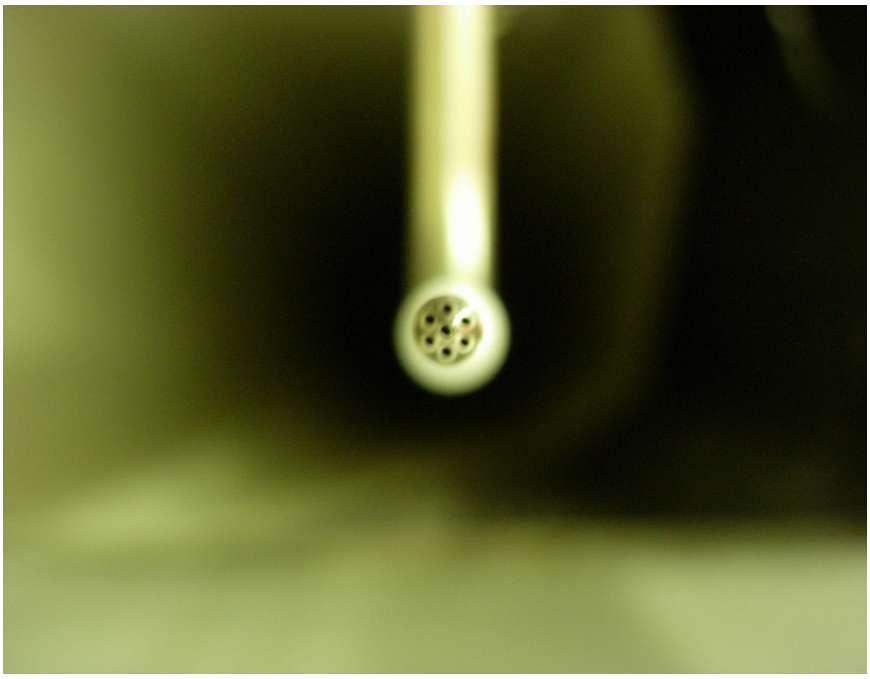

Figure 3.8. Seven-hole pressure probe.

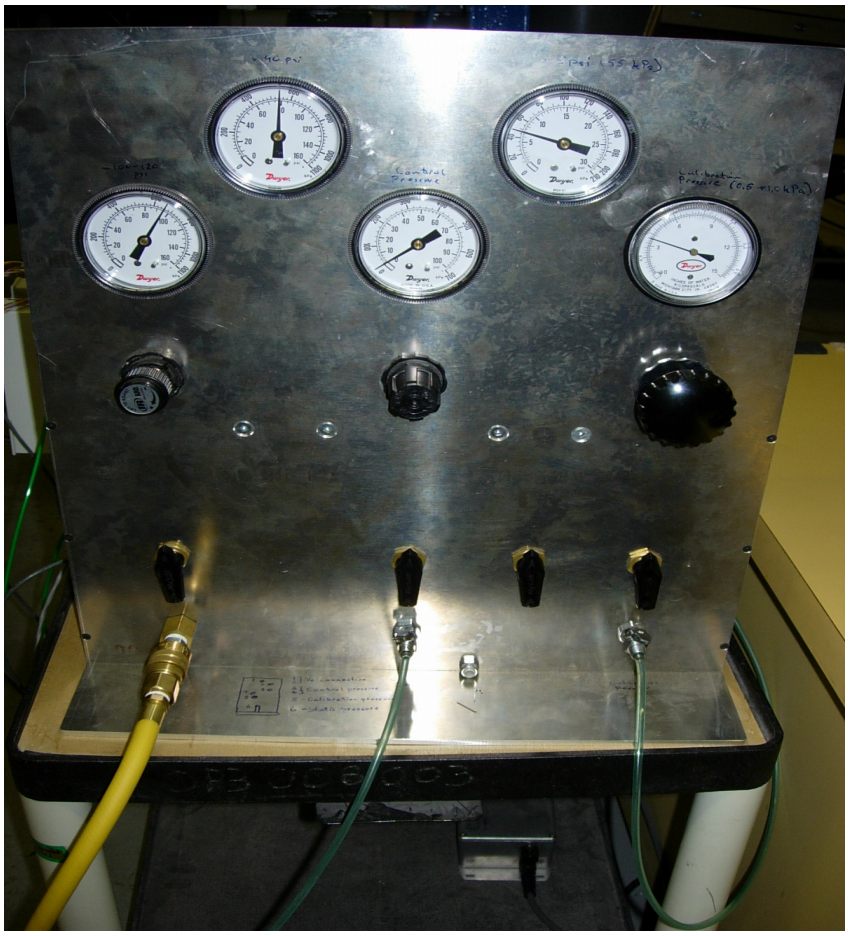

Figure 3.9. Control panel used to zero and calibrate the ZOC-17 pressure scanner.

Once calibrated, the seven-hole probe can measure the local time-averaged velocity vector (i.e. the mean velocity components u, v and w, where u is streamwise velocity component, v is cross-stream velocity component and w is wall-normal velocity component). The probe can measure the velocity vector at very high flow angles, up to 80° from the probe axis.

The seven pressures were measured with a Scanivalve ZOC-17 pressure scanner, shown in Figs. 3.9 and 3.10. A Barocel differential pressure transducer was used to check the calibration of the Scanivalve ZOC-17 pressure scanner. The probe was calibrated in

situ using an automated variable-angle calibrator, with a calibration grid spacing of 8.1° over a flow angle range of ±72.9°, and a direct-interpolation calibration data-reduction method was applied according to the recommendations of Sumner (2002). Similar to the Pitot-static probe and boundary layer Pitot probe, the seven-hole probe was configured to sample the pressure signals at a frequency of 500 Hz and 10,000 samples were used to obtain the time-averaged values.

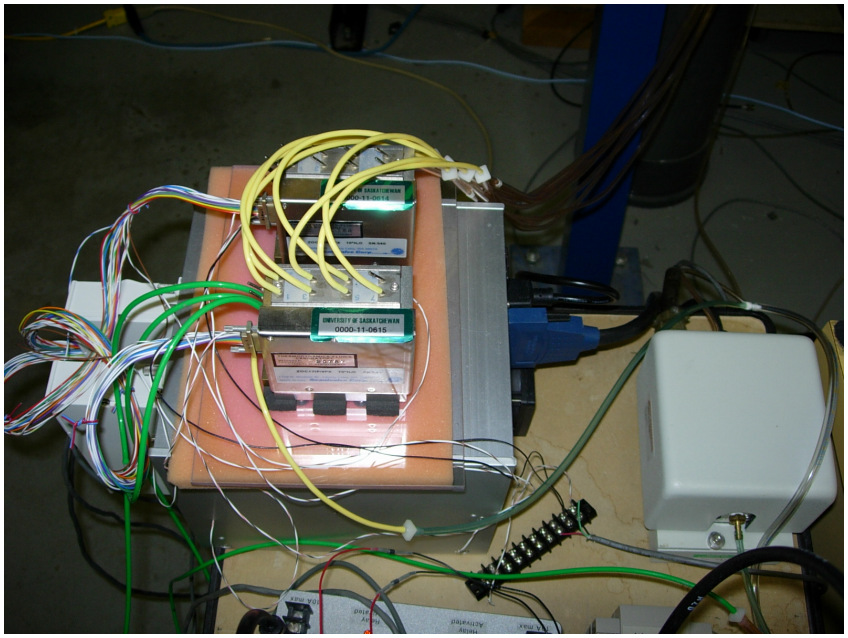

Figure 3.10. Scanivalve ZOC-17 pressure scanner used to measure the seven pressures from the seven-hole probe.

3.5 Boundary Layer Measurements

In order to build a thick and fully developed boundary layer at the location of the staggered finite circular cylinders, a trip was installed on the flat plate near the leading edge. A common problem encountered in generating a thick and fully developed boundary layer is inadequate space for the flow to develop on the flat plate. The initial

tests showed that the available length of the test section was limited and it was not long enough for a thick boundary layer to develop.

Therefore, a suitable "trip" was necessary to be chosen and installed on the flat plate to build the desired boundary layer. A trip creates an additional disturbance which can (i) make the transition from laminar flow to turbulent flow occur earlier and (ii) artificially thicken the boundary layer. The size and location of the trip were varied to seek the desired boundary layer thickness. The following trips were tested in the experiments, a rough strip, 8-32 NC, 1/4-20 NC, 5/16-18 NC, 1/2-13 NC threaded rods, and a 0.375-inch square rod. The trips were individually fastened by double-sided tape on the flat plate at 50 mm, 100 mm, and 200 mm from the leading edge.

To assess the performance of the trips, different parameters of the boundary layer were calculated from the experimental data obtained with the boundary layer Pitot tube, including the boundary layer thickness, displacement thickness, momentum thickness and shape factor. The boundary layer thickness, δ, is the distance from the ground plane where the velocity is zero to the point where the velocity is 99 percent of the freestream velocity. The displacement thickness, δ^*, is defined as the thickness of the flow outside the boundary layer which has the same mass flow rate as the retarded part of the flow in the boundary layer (Fox and McDonald, 1992),

$$\delta^* = \int_0^{\infty} \left(1 - \frac{u}{U_{\infty}}\right) \mathrm{d}z \approx \int_0^{\delta} \left(1 - \frac{u}{U_{\infty}}\right) \mathrm{d}z \,. \tag{3.10}$$

The momentum thickness, θ, is defined as the thickness of the flow outside the boundary

layer which has the same amount of momentum flux as the reduction of momentum flux in the boundary layer due to the existence of the viscosity (Fox and McDonald, 1992),

$$\theta = \int_0^{\infty} \frac{u}{U_{\infty}}\left(1 - \frac{u}{U_{\infty}}\right)\mathrm{d}z \approx \int_0^{\delta} \frac{u}{U_{\infty}}\left(1 - \frac{u}{U_{\infty}}\right)\mathrm{d}z \,. \tag{3.11}$$

The shape factor is defined as $H = \delta^*/\theta$. The Reynolds number based on the momentum thickness, is defined as $\mathrm{Re}_{\theta} = \rho_{\infty} U_{\infty} \theta / \mu_{\infty}$. The mean velocity profile for a turbulent boundary layer on a smooth flat plate can be approximated by the "1/7-power" profile expression (Fox and McDonald, 1992),

$$\frac{u}{U_{\infty}} = \left(\frac{z}{\delta}\right)^{\frac{1}{7}} . \tag{3.12}$$

The first group of boundary layer measurements was conducted without a trip installed. The purpose of these experiments was to look at the flow downstream of the "superellipse" leading edge. The mean velocity profiles on the centerline of the flat plate were measured at four different locations, 0 mm, 50 mm, 100 mm and 200 mm downstream from the joint of the super ellipse leading edge contour and the flat plate. As seen from the mean streamwise velocity profiles in Fig. 3.11, no reliable velocities could be measured from z = 0 to 8 mm at the joint location, and the same situation occurred in the wall-normal direction from z = 0 to 5 mm at the location of 50 mm downstream from the joint, indicating that negative local dynamic pressure, caused by the flow separation, was measured by the Pitot probe at those positions. In addition, it was also seen that the reverse flow region decreased in size downstream. The velocity profile 100 mm downstream from the joint showed that the flow direction near the ground turned back to

freestream direction and the separation ended. Through the observation of the streamwise velocity profiles, it was concluded that there was flow separation at the leading edge of the plate and the separation ended between 50 mm and 100 mm downstream from the joint.

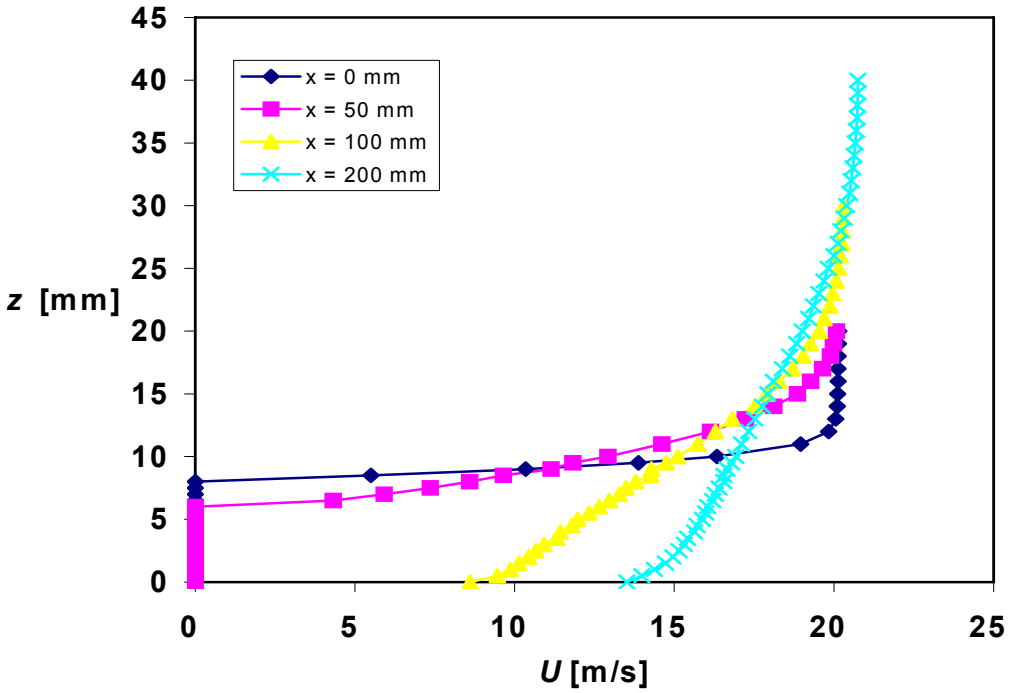

Figure 3.11. Mean velocity profiles obtained without the trip at 0 mm, 50 mm, 100 mm and 200 mm from the location of the joint between the super ellipse leading edge contour and the flat plate body.

In the second group of experiments, the boundary layer mean velocity profile was measured without the trip at five locations on the test section centerline at x = 0 mm, x = -200 mm, x = -400 mm, x = 200 mm and x = 400 mm, where x = 0 mm now refers to the eventual location of the central cylinder, to examine the boundary layer at and around the eventual location of the central cylinder. The mean velocity profiles are shown in Fig.

3.12. The boundary layer thickness, displacement thickness, and momentum thickness increased in the streamwise direction as shown in the Table 3.1. The shape factor remained constant in the streamwise direction. From Table 3.1, it was seen that δ/H = 0.34 at the location of the cylinder, which was lower than the desired value of δ/H = 0.5 (Adaramola et al., 2006). Therefore, a trip was needed to artificially thicken the boundary layer.

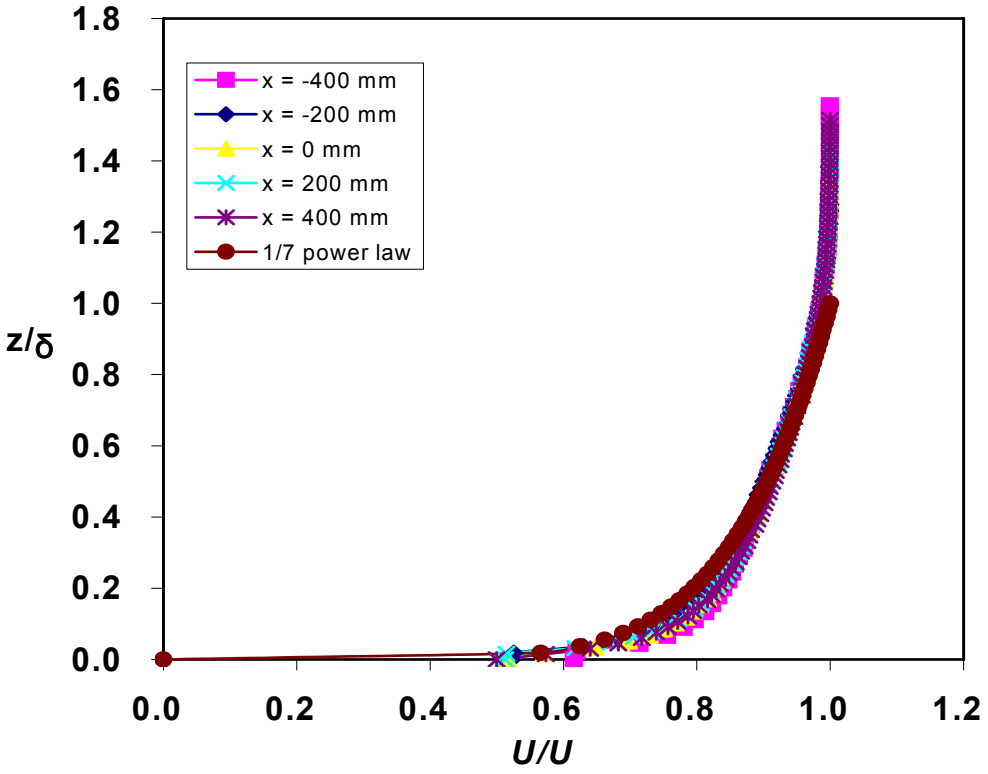

Figure 3.12. Mean velocity profiles obtained without the trip measured at the locations of x = -200 mm, x = -400 mm, x = 0 mm, x = 200 mm and x = 400 mm.

Table 3.1. Boundary layer parameters measured without the trip at different locations (corresponding to the data in Fig. 3.12).

x (mm)	Re_θ	δ (mm)	δ^*(mm)	θ (mm)	H	δ / H
-400	5113	45	5.1	4.2	1.2	0.26
-200	6574	54	6.9	5.4	1.3	0.31
0	6817	59	7.0	5.6	1.3	0.34
200	7304	63	7.6	6.0	1.3	0.37
400	7548	66	7.7	6.2	1.3	0.38

In the third group of experiments, different trips were used to attempt to increase δ/H. The mean velocity profiles and boundary layer parameters are shown in Fig. 3.13 and Table 3.2. First, a rough strip was installed on the flat plate at 40 mm downstream from the leading edge, but the boundary layer showed no difference from the one without the strip, which meant the rough strip did not create a sufficient disturbance to affect the boundary layer development. Then, an 8-32 NC threaded rod was installed at 200 mm downstream from the leading edge and the mean velocity profile was measured at x = 0 mm. As seen in Fig. 3.13 and Table 3.2, δ did not increase and only the shape of the mean velocity profile changed slightly, implying that the rod did not significantly influence the boundary layer at the cylinder location. Therefore, the rod was moved forward to 50 mm downstream from the leading edge. However, the result showed the opposite effect of a trip, that the boundary layer became thinner, which was probably because the trip was close to or within the separation bubble. After changing to a larger 1/4-20 NC threaded rod placed at two locations of 50 mm and 200 mm downstream from the leading edge, there was still no apparent improvement of δ at the eventual cylinder position. In

summary, the threaded rods were too thin compared to the local boundary layer thickness and thus were totally submerged in the boundary layer. At last, a 1/2-13 NC threaded rod was installed 200 mm from the plate leading edge. The mean velocity profile was again measured at x = 0 and δ increased by 10 mm, but the mean velocity profile looked irregular due to the large size of the rod, which produced strong disturbance and made the boundary layer incorporate some "wake" effects.

Table 3.2 Boundary layer parameters with different trips measured at the eventual cylinder position.

	δ (mm)	δ^* (mm)	θ (mm)	H	Re_θ	δ / H
No trip	59	7.0	5.6	1.3	6817	0.34
Rough strip at 40 mm from leading edge	58	7.2	5.7	1.27	6939	0.34
8-32 NC rod at 50 mm from leading edge	55	7.0	5.3	1.3	6430	0.32
8- 32 NC rod at 200 mm from leading edge	60	7.9	6.3	1.3	7604	0.35
1/4-20 NC rod at 50 mm from leading edge	55	6.9	5.4	1.3	6575	0.32
1/4-20 NC rod at 200 mm from leading edge	61	9.1	7.0	1.3	8488	0.36
1/2-13 NC rod at 200 mm from leading edge	69	11.1	8.4	1.3	10147	0.40

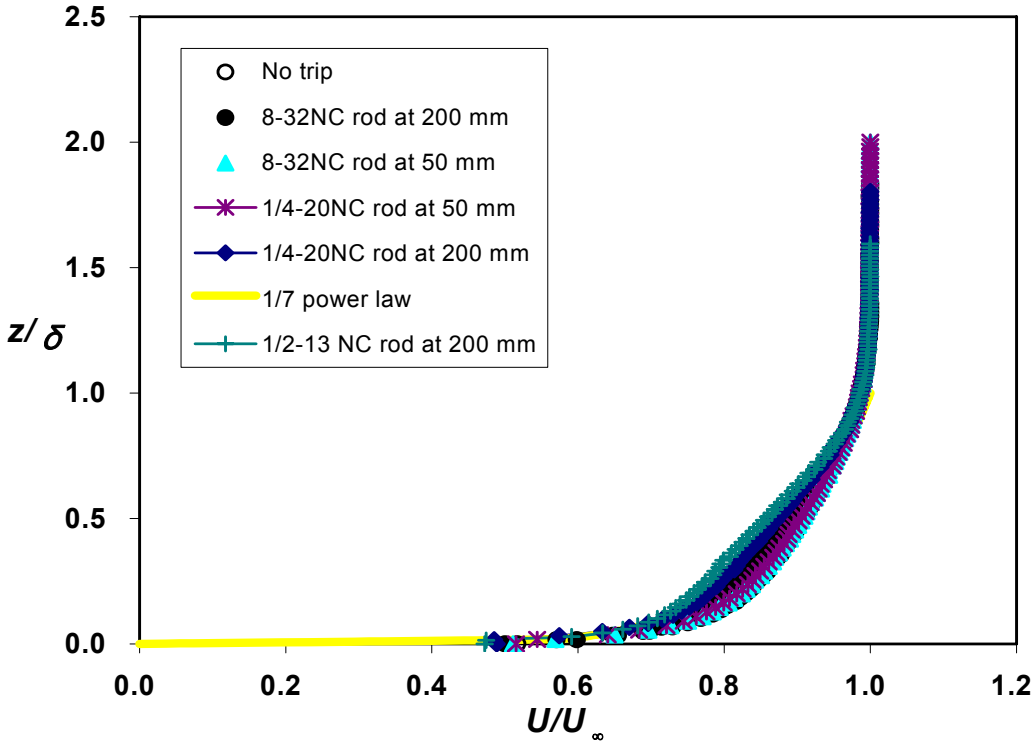

Figure 3.13. Mean velocity profiles measured at the eventual cylinder position with different trips.

The fourth group of experiments was carried out with a 0.375-inch square rod installed 100 mm downstream from the plate leading edge. The mean velocity profile was measured at x = -400 mm, x = -200 mm, x = -100 mm, x = 0 mm, x = 200 mm and x = 400 mm, and the results are presented in Fig. 3.14, Fig. 3.15, and Table 3.3. As shown in Table 3.3, the boundary layer thickness, displacement thickness, and momentum thickness increased in the streamwise direction except at x = -100 mm. The shape factor remained constant and the ratio δ/H approached the desired value of 0.5. Based on these results, the 0.375-inch square rod located at 100 mm downstream from the leading edge was chosen to be the trip used to generate the boundary layer.

Table 3.3 Boundary layer parameters measured around the eventual cylinder position.

	δ (mm)	δ^* (mm)	θ (mm)	H	Re_θ	δ/H
No trip at x = 0 mm	59	7.0	5.6	1.3	6817	0.34
x = 100 mm (with rough strip at 40 mm from the leading edge)	65	8.9	6.9	1.3	8378	0.38
Rod at 50 mm from leading edge measurements at x = 0 mm	59	7.7	6.1	1.3	7325	0.34
Rod at 100 mm from leading edge measurements at x = -400 mm	49	6.9	5.5	1.3	6671	0.29
Rod at 100 mm from leading edge measurements at x = -200 mm	62	9.1	7.0	1.3	8511	0.36
Rod at 100 mm from leading edge measurements at x = -100 mm	65	8.8	7.0	1.3	8451	0.38
Rod at 100 mm from leading edge measurements at x = 0 mm	68	9.3	7.3	1.3	8826	0.40
Rod at 100 mm from leading edge measurements at x = 200 mm	72	9.2	7.4	1.3	8923	0.42
Rod at 100 mm from leading edge measurements at x = 400 mm	76	9.4	7.6	1.3	9141	0.44

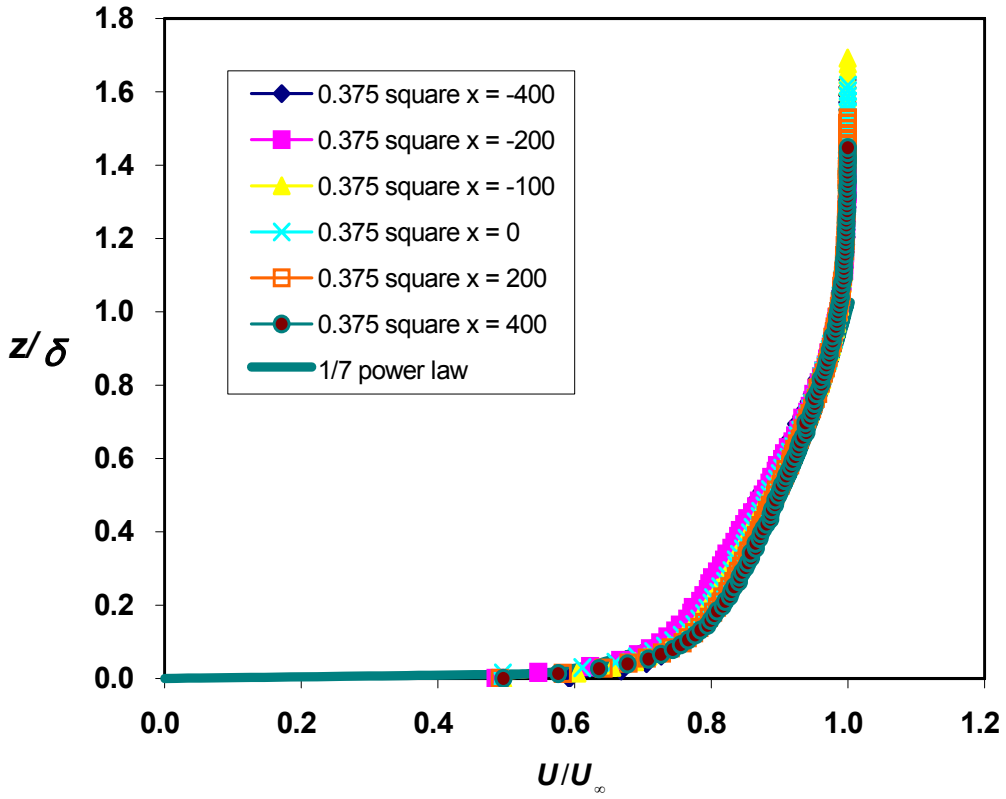

Figure 3.14. Mean velocity profile with 0.375-inch square rod at x = -400 mm, x = -200 mm, x = -100 mm, x = 0 mm, x = 200 mm and x = 400 mm.

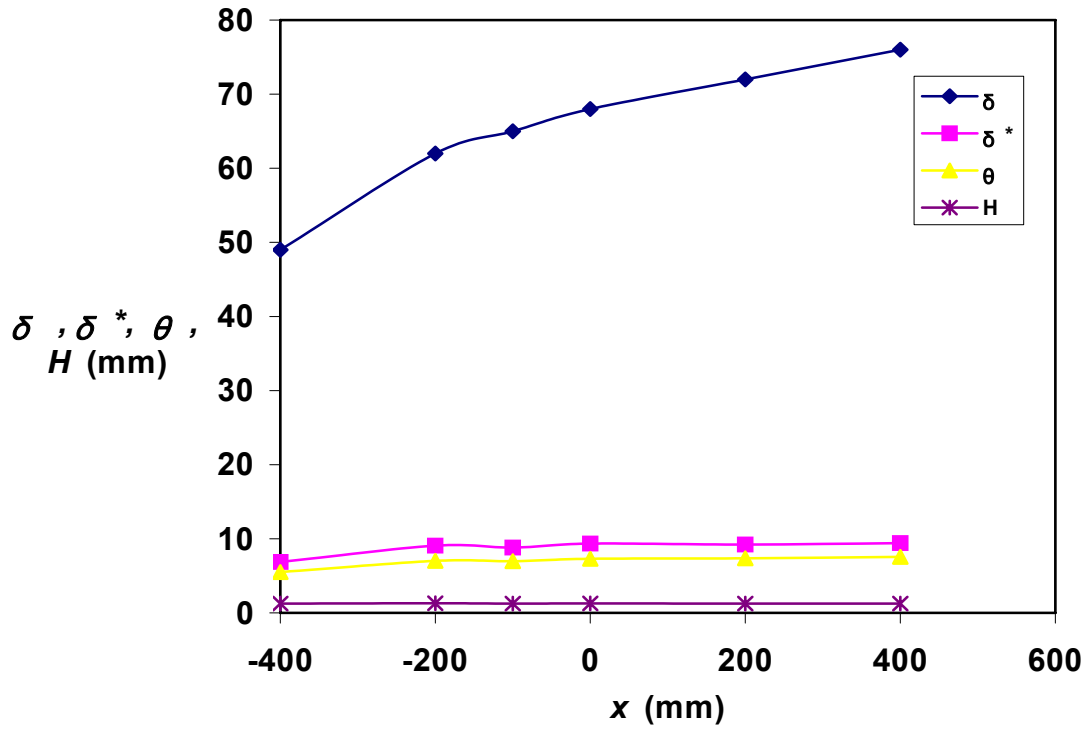

Figure 3.15. δ, δ^*, θ, H vs. streamwise position, x, parameters measured with 0.375-inch square rod installed at the location of 100 mm from the plate leading edge.

The final boundary layer results were measured with the TSI model 1243-20 boundary layer cross-flow X-probe and a TSI IFA-100 anemometer (described in Section 3.4.2), and were similar to that measured by the boundary layer Pitot probe. A summary of the results is given in the Table 3.4. The mean velocity profile in the boundary layer is shown in Fig. 3.16, while Fig. 3.17 and Fig. 3.18 show the turbulence intensities in streamwise and wall-normal directions, respectively. The Reynolds shear stress is shown in Fig. 3.19. These figures all indicated that the flow at x = 0 was still developing and became fully developed at the location of x = 600 mm.

Table 3.4 Boundary layer parameters measured at the eventual cylinder position with a 0.375-inch square rod at location of 100 mm from the leading edge by the hot-wire probe.

x (mm)	δ (mm)	δ * (mm)	θ (mm)	H (= δ */ θ)	Re_θ	δ /H
-400	49	6.0	5.0	1.2	6470	0.29
-200	56	5.9	5.0	1.2	6470	0.33
-100	58	6.0	5.1	1.2	6600	0.34
0	63	6.5	5.6	1.2	7246	0.37
200	68	6.7	5.8	1.2	7505	0.40
400	70	6.8	5.9	1.2	7635	0.41
500	71	6.5	5.7	1.1	7376	0.41
600	74	6.9	6.0	1.2	7764	0.43

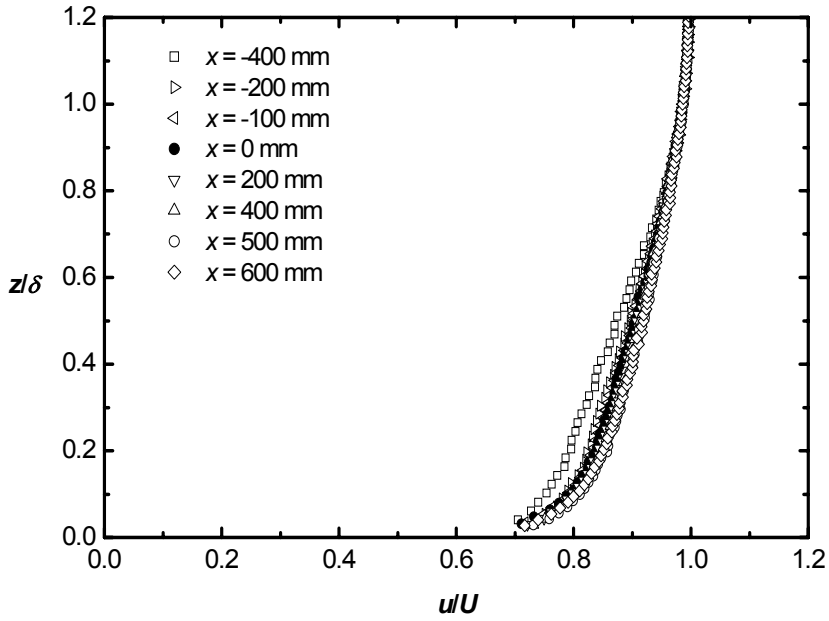

Figure 3.16. Mean streamwise velocity profile of the boundary layer measured with the hot-wire probe at the locations of x = -400, -200, -100, 0, 200, 400, 500, 600 mm.

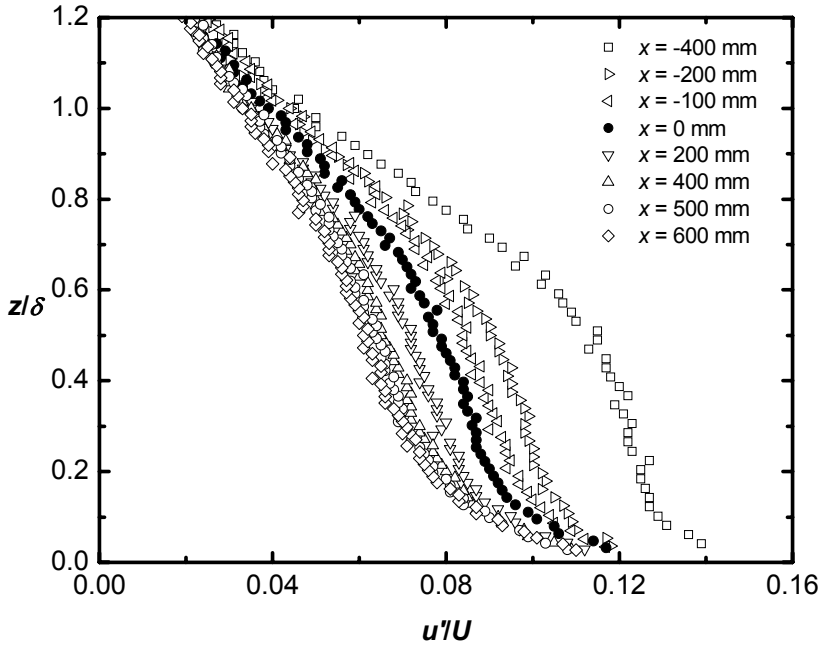

Figure 3.17. Streamwise turbulent intensity measured with the hot-wire probe at the locations of x = -400, -200, -100, 0, 200, 400, 500, 600 mm.

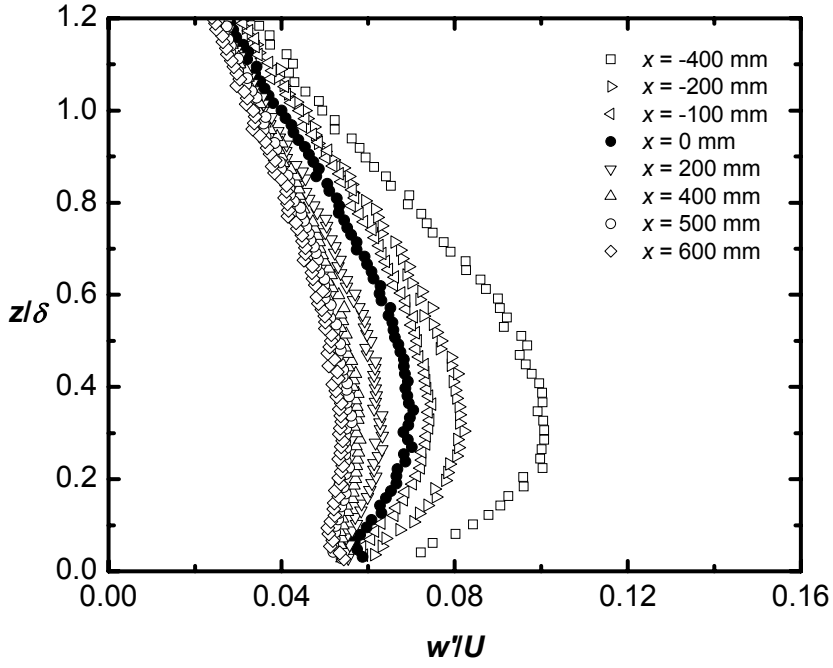

Figure 3.18. Turbulent intensity in the wall-normal direction measured with the hot-wire probe at the locations of x = -400, -200, -100, 0, 200, 400, 500, 600 mm.

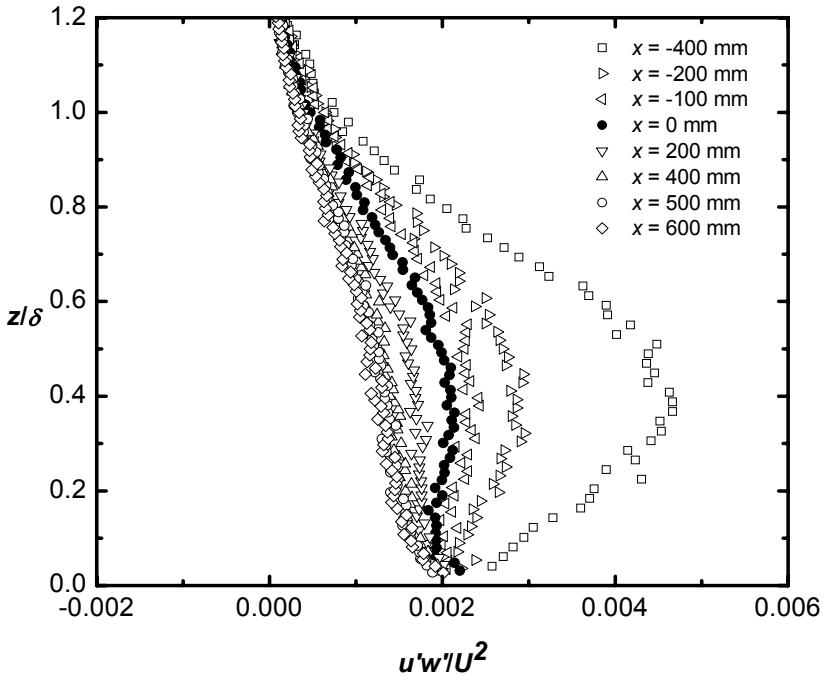

Figure 3.19. Reynolds shear stress measured with the hot-wire probe at the locations of x = -400, -200, -100, 0, 200, 400, 500, 600 mm.

3.6 Measurement Uncertainty

In this thesis, the wind tunnel measurements (results) are subject to different sources of uncertainty, from instrumentation, data acquisition and data analysis. A final result, R, is typically the combination of different measured variables, x_i. The contribution of the uncertainty in each variable to the result can be calculated by

$$\sigma_R = \left[\sum_1^n \left(\frac{\partial R}{\partial x_i} \sigma_{x_i} \right)^2 \right]^{\frac{1}{2}}, \tag{3.13}$$

where σ_R is the uncertainty of the result R, $\partial R/\partial x_i$ is the sensitivity of the variable x_i, and σ_{x_i} is the uncertainty of the variable x_i.

The measurement uncertainty can be broadly classified into two types, the

precision or random errors, P, and the bias or systematic errors, B. The two types of errors should be analyzed and calculated separately,

$$B = \left[B_1^2 + B_2^2 + B_3^2 + ... + B_n^2\right]^{1/2}, \tag{3.14}$$

$$P = \left[P_1^2 + P_2^2 + P_3^2 + ... + P_n^2\right]^{1/2}, \tag{3.15}$$

where B is the total bias error, B_1 to B_n are the bias errors from individual variables or measurements, P is the total precision error, and P_1 to P_n are the precision errors from individual variables or measurements. The total uncertainty, U, is calculated as

$$U = \left[B^2 + \left(tP\right)^2\right]^{1/2}, \tag{3.16}$$

where t is the two-tailed Student t number for the 95% confidence level (in this research, t = 2).

Based on equation (3.13), the calculations of the uncertainties in the different variables in the experiments are presented as follows, with the results summarized in Table 3.5 at the end of the Chapter. The individual bias and precision errors in Table 3.5 come from a number of sources, including instrument specifications, calibration curves, and the previous experience of the research group.

The freestream density is calculated through the ideal gas equation shown earlier in equation (3.3). The uncertainty of the freestream density is determined by

$$\sigma_{\rho_\infty} = \left[\left(\frac{\partial \rho_\infty}{\partial P_\infty}\sigma_{P_\infty}\right)^2 + \left(\frac{\partial \rho_\infty}{\partial T_\infty}\sigma_{T_\infty}\right)^2\right]^{\frac{1}{2}}, \tag{3.17}$$

$$\sigma_{\rho_\infty} = \left[\left(\frac{1}{RT_\infty}\sigma_{P_\infty}\right)^2 + \left(\frac{P_\infty}{RT_\infty^2}\sigma_{T_\infty}\right)^2\right]^{\frac{1}{2}}. \tag{3.18}$$

The freestream velocity is calculated from equation (3.2). The uncertainty in the freestream velocity is

$$\sigma_{U_\infty} = \left[\left(\frac{\partial U_\infty}{\partial q_\infty} \sigma_{q_\infty} \right)^2 + \left(\frac{\partial U_\infty}{\partial \rho_\infty} \sigma_{\rho_\infty} \right)^2 \right]^{\frac{1}{2}}, \tag{3.19}$$

$$\sigma_{U_\infty} = \left[\left(\frac{1}{\sqrt{2 q_\infty \rho_\infty}} \sigma_{q_\infty} \right)^2 + \left(\sqrt{\frac{q_\infty}{2 \rho_\infty^3}} \sigma_{\rho_\infty} \right)^2 \right]^{\frac{1}{2}}. \tag{3.20}$$

The freestream viscosity, μ_∞, is calculated through the Sutherland correlation, shown earlier in equation (3.4). Its uncertainty is expressed as

$$\sigma_{\mu_\infty} = \frac{\partial \mu_\infty}{\partial T_\infty} \sigma_{T_\infty}, \tag{3.21}$$

$$\sigma_{\mu_\infty} = \frac{1.5 b T_\infty^{\frac{1}{2}} (S + T_\infty) + b T^{\frac{3}{2}}}{(S + T_\infty)^2} \sigma_{T_\infty}. \tag{3.22}$$

The Strouhal number is defined as

$$St = \frac{fD}{U_\infty}. \tag{3.23}$$

The uncertainty in Strouhal number is determined by

$$\sigma_{St} = \left[\left(\frac{\partial St}{\partial f} \sigma_f \right)^2 + \left(\frac{\partial St}{\partial D} \sigma_D \right)^2 + \left(\frac{\partial St}{\partial U_\infty} \sigma_{U_\infty} \right)^2 \right]^{\frac{1}{2}}, \tag{3.24}$$

$$\sigma_{St} = \left[\left(\frac{D}{U_\infty} \sigma_f \right)^2 + \left(\frac{fD}{U_\infty^2} \sigma_{U_\infty} \right)^2 \right]^{\frac{1}{2}}. \tag{3.25}$$

The Reynolds number based on the cylinder diameter is defined as

$$\mathrm{Re}_D = \frac{\rho_\infty U_\infty D}{\mu_\infty}. \tag{3.26}$$

The uncertainty in the Reynolds number is calculated through

$$\sigma_{\mathrm{Re}_D} = \left[\left(\frac{\partial \mathrm{Re}_D}{\partial \rho_\infty} \sigma_{\rho_\infty} \right)^2 + \left(\frac{\partial \mathrm{Re}_D}{\partial D} \sigma_D \right)^2 + \left(\frac{\partial \mathrm{Re}_D}{\partial U_\infty} \sigma_{U_\infty} \right)^2 + \left(\frac{\partial \mathrm{Re}_D}{\partial \mu_\infty} \sigma_{\mu_\infty} \right)^2 \right]^{\frac{1}{2}}, \quad (3.27)$$

$$\sigma_{\mathrm{Re}_D} = \left[\left(\frac{U_\infty D}{\mu_\infty} \sigma_{\rho_\infty} \right)^2 + \left(\frac{\rho_\infty D}{\mu_\infty} \sigma_{U_\infty} \right)^2 + \left(\frac{\rho_\infty U_\infty D}{\mu_\infty^2} \sigma_{\mu_\infty} \right)^2 \right]^{\frac{1}{2}}. \quad (3.28)$$

Table 3.5 Summary of the variable uncertainty.

Variable	Typical Value	Bias Error	Precision Error	Total Uncertainty
Diameter of the cylinder (D)	0.01905 m	± 0.000 mm	± 0.000mm	± 0.000 m
Height of the cylinder (H)	171.45 mm	± 0.000 mm	± 0.000 mm	± 0.000 mm
Streamwise coordinate (x)	57.153 mm	± 0.000 mm	± 0.500 mm	± 0.500 mm
Cross-stream coordinate (y)	-19.048 mm	± 0.000 mm	± 0.500 mm	± 0.500 mm
Wall-normal coordinate (z)	85.731 mm	± 0.000 mm	± 0.500 mm	± 0.500 mm
Vortex shedding frequency (f)	168 Hz	± 0 Hz	± 1 Hz	± 1.190%
Freestream dynamic pressure (q_∞)	223.869 Pa	± 0 Pa	± 1.119 Pa	± 1.000%
Freestream static pressure (P_∞)	96.0 kPa	± 240.065 Pa	± 240.065 Pa	± 0.559%
Freestream temperature (T_∞)	298.700 K	± 0 K	± 0.5 K	± 0.335%
Freestream dynamic viscosity (μ_∞)	1.84×10^{-5} Ns/m^2	± 0 Ns/m^2	± 6.87×10^{-8} Ns/m^2	± 0.747%
Freestream density (ρ_∞)	1.120 kg/m^3	± 0.003 kg/m^3	± 0.003 kg/m^3	± 0.652%
Freestream velocity (U_∞)	19.993 m/s	± 0.201 m/s	± 0.058 m/s	± 1.165%
Strouhal number, St	0.160	± 0.002	± 0.001	± 1.663%
Reynolds number (Re_D)	2.32×10^4	± 240.752	± 130.129	± 1.529%

CHAPTER 4

RESULTS AND DISCUSSION

4.1 Introduction

In this chapter, the main results of the research are presented and are divided into three parts: (i) vortex shedding from a single finite circular cylinder (Section 4.2), (ii) vortex shedding from two staggered finite circular cylinders (Section 4.3), and (iii) velocity field measurements in the combined wake of two staggered finite circular cylinders (Section 4.4). Section 4.3, on vortex shedding from two staggered finite circular cylinders, is subdivided into the measurements *at the mid-height* of the two staggered circular cylinders (Section 4.3.1) and measurements *along the height* of the circular cylinders (Section 4.3.2).

4.2 Vortex Shedding from a Single Finite Circular Cylinder

For the single finite circular cylinder, Strouhal number measurements were made along the height of the cylinder and the hot-wire probe was fixed at $x/D = 3$ and $y/D = 1$, with the wall-normal position allowed to vary from $z/H = 0.05$ to 1.05 at an interval of $\Delta z/H = 0.05$. The measurements were made at a freestream velocity of $U_\infty = 20$ m/s, corresponding to a Reynolds number of $\mathrm{Re}_D = 2.4\times10^4$.

From Fig. 4.1, a notable variation in the shape and strength of the peaks in the power spectra along the height of the cylinder is observed. The Strouhal number was

about St = 0.16 and remained constant from the bottom to the tip of the cylinder. Sharp and strong peaks were measured around the mid-height of the cylinder ($z/H = 0.5$) which were similar in shape to what would typically be observed for the vortex shedding from an infinite cylinder. Broader peaks were found near the base of the cylinder in the flat-plate boundary layer (for $z/H < 0.4$, where $\delta/H \approx 0.4$) resulting from the interference from the boundary layer and horseshoe vortex on the Kármán vortex shedding. As the free end is approached, the shape of the power spectra becomes irregular and the peaks change to be weaker and wider, which indicates that the regular Kármán vortex shedding was disturbed by the downwash flow from the free end and the tip flow field, which is strongly three-dimensional. These results are in agreement with Okamoto and Sunabashiri (1992), Park and Lee (2000), Sumner et al. (2004), Adaramola et al. (2006), and others.

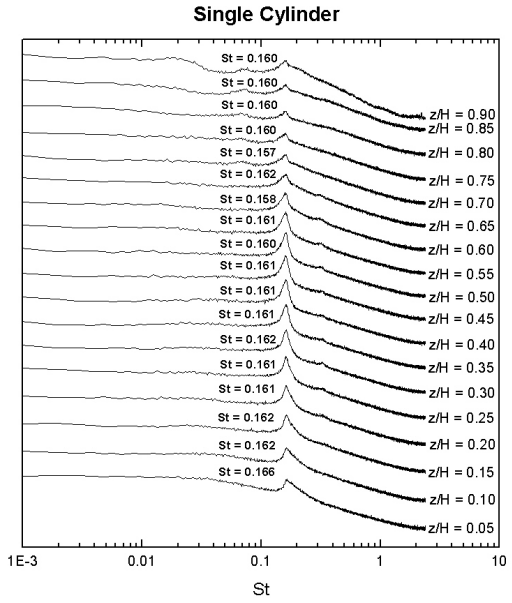

Figure 4.1. The power spectra along the height of a single finite circular cylinder, Re_D =

2.4×10^4, AR = 9, δ/H = 0.4, probe positioned at x/D = 3 and y/D = 1.

4.3 Vortex Shedding from Two Staggered Finite Circular Cylinders

In this section, vortex shedding from two staggered finite circular cylinders is shown from two points of view. First, measurements of the vortex shedding frequency were conducted only at the mid-height of two staggered finite circular cylinders; the results and discussion of these experiments are presented in Section 4.3.1. Second, the vortex shedding frequencies were measured along the heights of the two staggered finite circular cylinders, but only for selected staggered-cylinder configurations; the results and discussion of these experiments are presented in Section 4.3.2.

4.3.1 Strouhal Number Measurements at Mid-Height

For the Strouhal number measurements at the mid-height of two staggered finite circular cylinders, the hot-wire probe was positioned at x/D = 3, y/D = 1 and z/H = 0.5 for most measurements. However, y/D was also varied for some cases where it was difficult to find a peak or the peak was very weak or absent. The experimental data showed that the Strouhal number behaviour could be broadly classified according to pitch ratio, similar to Sumner et al. (2005) for two staggered *infinite* cylinders, into closely spaced configurations (P/D = 1.125, 1.25), moderately spaced configurations (P/D = 1.5, 2, 2.5, 3) and widely spaced configurations (P/D = 4, 5). For two *finite* circular cylinders, the present experiments showed that moderately spaced behaviour extends to P/D = 3, which

is a higher range of P/D than two *infinite* circular cylinders (P/D = 2.5) as a result of a longer vortex formation length (defined as the point downstream of the cylinder where the velocity fluctuation level has grown to a maximum (Williamson, 1996)) and larger interference region for finite cylinders than infinite cylinders.

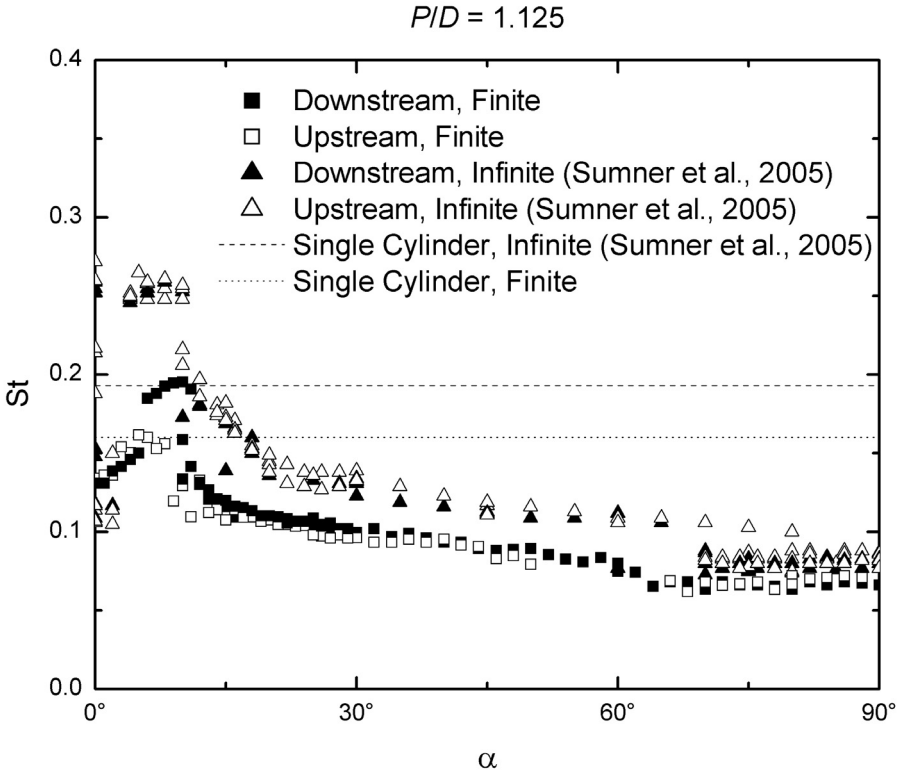

Figure 4.2. Strouhal number data for two closely spaced staggered circular cylinders, P/D = 1.125, z/H = 0.5. Open symbols: upstream cylinder; solid symbols: downstream cylinder; triangle symbols: infinite cylinders; square symbols: finite cylinders. For two staggered finite circular cylinders, $Re_D = 2.4\times10^4$, AR = 9, δ/H = 0.4. For two staggered infinite circular cylinders, $Re_D = 3.2\times10^4$-7.3×10^4.

4.3.1.1 Closely Spaced Staggered Configurations (P/D = 1.125, 1.25)

From the graphs of Strouhal number versus incidence angle for P/D = 1.125 and 1.25 in Figs. 4.2 and 4.3, respectively, it is observed that the St data measured behind the

downstream cylinder agree fairly well with the data from the upstream cylinder for most incidence angles from α = 0° to 90° except for the region around a "critical incidence angle" of $\alpha \approx 10°$. For two *infinite* circular cylinders at closely and moderately spaced staggered configurations, the critical incidence angle is defined as the incidence angle where the mean drag coefficient on the upstream cylinder reaches a local maximum value and a maximum inward-directed mean lift coefficient (known as the "inner lift peak") and a local minimum mean drag coefficient are experienced by the downstream cylinder (Zdravkovich and Pridden 1977; Sumner et al., 2005). In addition, the Strouhal number attains a local maximum value at the critical incidence angle (Akosile and Sumner, 2004; Sumner et al., 2005). Here, for the two *finite* circular cylinders in closely and moderately spaced staggered configurations, in the absence of any force measurements (this will be a subject for future research), the critical incidence angle is identified as the incidence angle where the St obtains a local maximum value.

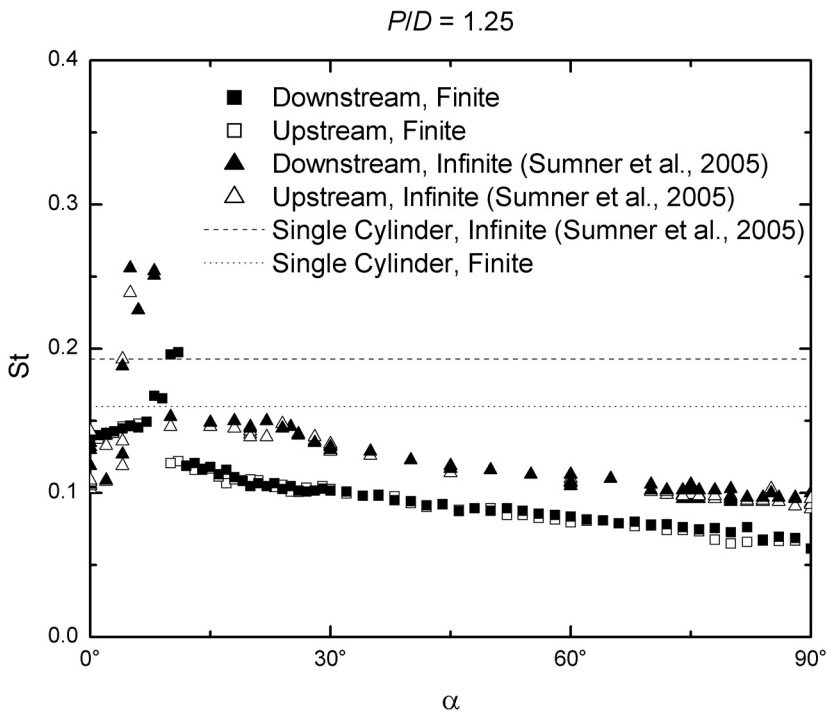

Figure 4.3. Strouhal number data for two closely spaced staggered circular cylinders, P/D = 1.25, z/H = 0.5. Symbols as in Figure 4.2. For two staggered finite circular cylinders, $Re_D = 2.4\times10^4$, AR = 9, δ/H = 0.4. For two staggered infinite circular cylinders, $Re_D = 3.2\times10^4$-7.3×10^4.

At the outset, it is observed in Figs. 4.2 and 4.3 that the Strouhal numbers for the staggered *finite* circular cylinders are smaller than those of the staggered *infinite* circular cylinders. This is consistent with single-cylinder behavior. The smaller St is caused by the downwash flow separated from the free end. The downwash flow descending into the wake behind the cylinders lengthens the vortex formation region and reduces the vortex shedding frequency (Park and Lee, 2000).

Figures 4.2 and 4.3 show that the same St is measured behind both cylinders, implying the vortices shed from the outer shear layer of the upstream cylinder and outer shear layer of the downstream cylinder come from a single vortex shedding process.

The characteristics of the vortex shedding behind the two finite cylinders for P/D = 1.125 and 1.25 are consistent with the results of closely spaced *infinite* circular cylinders, indicating the two finite circular cylinders also behave as a single bluff body at the mid-height position (z/H = 0.5). Similar to the results of two staggered *infinite* cylinders, a critical incidence angle of $\alpha \approx 10°$ exists for both P/D = 1.125 and 1.25, where the St reaches a local maximum value. When α is greater than the critical value, St is lower than that of a single finite circular cylinder (St = 0.16, Section 4.2) and decreases gradually with increasing α. At higher α, the gap space normal to the flow direction between the two cylinders is broader, which leads to more oncoming flow passing through the gap, and the base-bleed flow pattern (BB) is formed (Sumner et al., 2000). The strong base-bleed flow from the gap between the cylinders interacts with the two shear layers, resulting in an increase in the vortex formation length and the slow reduction in St.

Compared with the Strouhal number behaviour of the two staggered *infinite* cylinders in Figs. 4.2 and 4.3, the St of the *finite* cylinders has less scatter at small incidence angles and corresponds to a more "stable" vortex shedding process than the infinite cylinders. The critical angle of $\alpha \approx 10°$ for the finite cylinders is higher than the critical angle of $\alpha \approx 9°$ for the infinite cylinders at P/D = 1.125 and 1.25 configurations.

For P/D = 1.125 (Fig. 4.2), the appearance of the base-bleed flow between the two *infinite* circular cylinders when they are at $\alpha \approx 70°$ causes a streamwise stretch of the near-wake region and a lengthening of the vortex formation length, leading to a sudden drop of the St values, which is shown as a discontinuity in the Strouhal number (Sumner

et al., 2000, 2005). However, for the *finite* circular cylinders, there is no sharp discontinuity in the St data at $\alpha \approx 70°$. Instead, the St of the finite cylinders smoothly shifts to the lower value at $\alpha \approx 60°$, indicating that the base-bleed flow may have less influence on the vortex shedding behaviour of the finite cylinders than for the infinite cylinders, and the flow pattern changes more gradually for the finite cylinders when the base-bleed flow starts to penetrate into the gap between the two cylinders and enters the near-wake region.

The vortex shedding peaks measured behind the upstream cylinder and downstream cylinder, shown in the power spectra in Figs. 4.4 and 4.5, are strong and sharp when α is lower than the critical incidence angle, and become weak and broad-banded as the near-wake region behind the two cylinders gets wider at higher α. Especially for $\alpha > 70°$, where the base-bleed flow begins to occur and creates a broader near-wake region and a longer vortex formation length behind the two cylinders, the vortex shedding process is significantly weakened and the vortex shedding peaks are very weak. A similar behavior of the vortex shedding peaks was also detected for the *infinite*-cylinder cases at high α (Sumner et al., 2005).

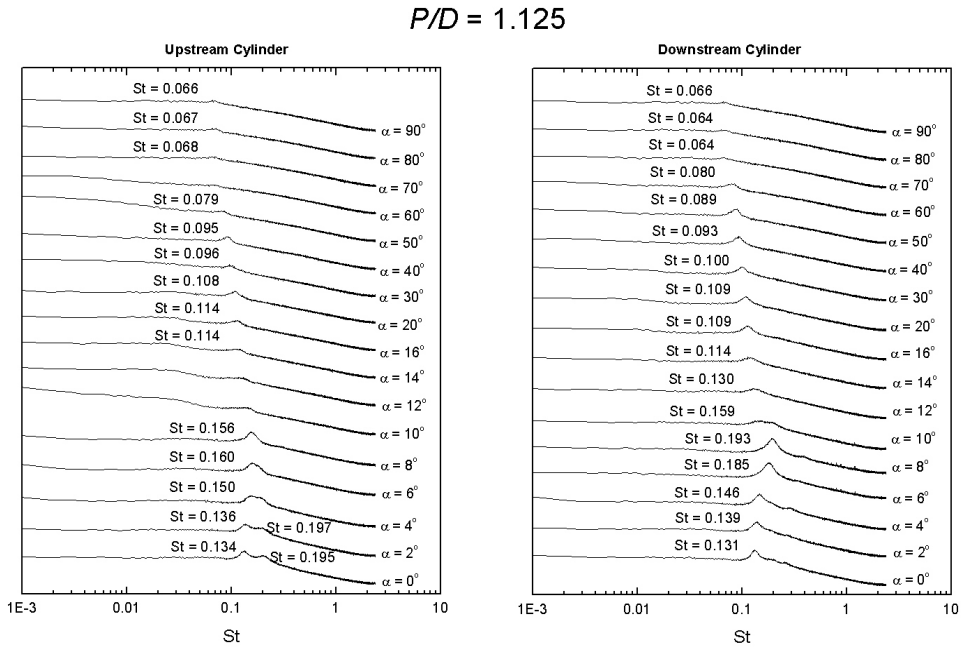

Figure 4.4. Selected power spectra, as a function of incidence angle, for closely spaced staggered cylinders: P/D = 1.125, z/H = 0.5, $Re_D = 2.4\times10^4$. Each spectrum represents 250 averages. The vertical (logarithmic) scale is arbitrary, but the same scale is used for each spectrum.

For P/D = 1.125 (Fig. 4.4), there is no peak at α = 10° and 12° (near the critical incidence angle), and two peaks are observed behind the upstream cylinder when the cylinders are in tandem (α = 0°) due to the transition of the flow pattern along the height of the cylinder (this is discussed later in Section 4.3.2.1). This phenomenon was not seen from the results of two tandem *infinite* cylinders (Sumner et al., 2005), and suggests that a flow pattern transition may have occurred, caused by the influence of the base and free end of the finite cylinder. For P/D = 1.25 (Fig. 4.5), no detectable peak is measured behind the upstream cylinder at α = 8°.

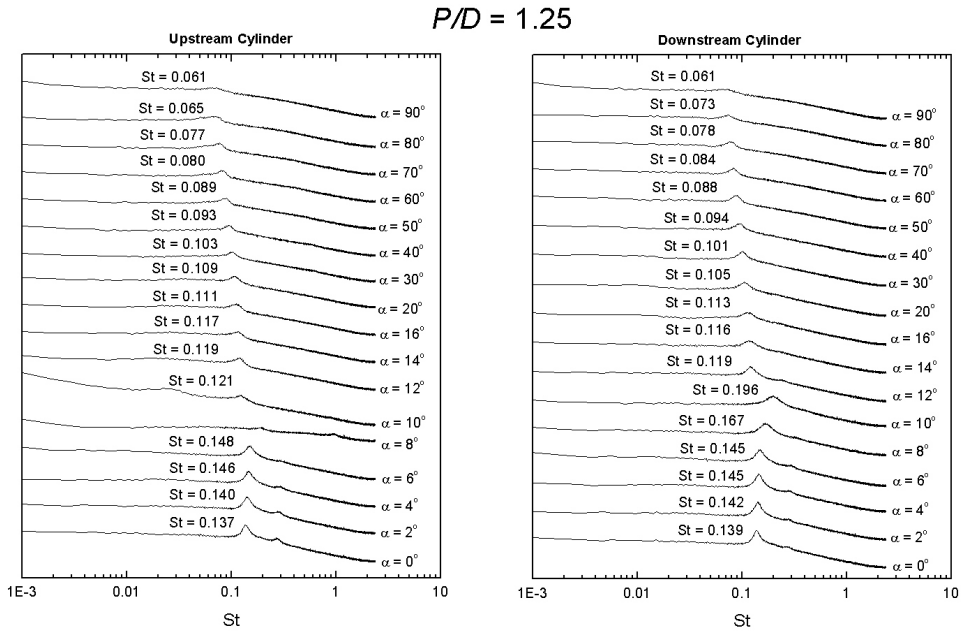

Figure 4.5. Selected power spectra, as a function of incidence angle, for closely spaced staggered cylinders: $P/D = 1.25$, $z/H = 0.5$, $\mathrm{Re}_D = 2.4\times10^4$. Each spectrum represents 250 averages. The vertical (logarithmic) scale is arbitrary, but the same scale is used for each spectrum.

4.3.1.2 Moderately Spaced Configurations (P/D = 1.5, 2, 2.5, 3)

The behavior of the Strouhal number data measured behind two staggered circular cylinders at moderate pitch ratios, shown in Fig. 4.6 ($P/D = 1.5$), Fig. 4.7 ($P/D = 2$), Fig. 4.8 ($P/D = 2.5$) and Fig. 4.9 ($P/D = 3$), is quite different from that of the closely spaced cylinders for a wide range of incidence angles. When the two cylinders are nearly in tandem and the incidence angle is small (Figs. 4.6 to 4.9), the St measured behind the upstream cylinder and downstream cylinder still remain the same and increase as α approaches the critical incidence angle of $\alpha \approx 12°$, where the two Strouhal numbers from the upstream cylinder and downstream cylinder become distinct. Based on what is seen

for the two staggered *infinite* cylinders, this variation of the St behaviour corresponds to the flow pattern transition from the shear layer reattachment flow pattern (SLR) to induced separation flow pattern (IS) (Sumner et al., 2000).

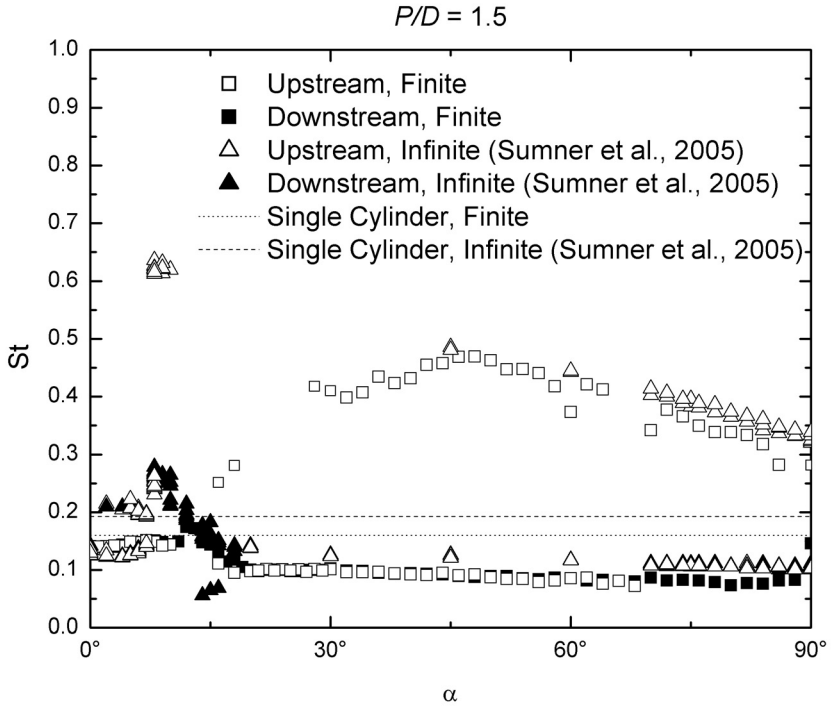

Figure 4.6. Strouhal number data for two moderately spaced staggered circular cylinders, P/D = 1.5, z/H = 0.5. Symbols as in Figure 4.2. For two staggered finite circular cylinders, $Re_D = 2.4\times10^4$, AR = 9, δ/H = 0.4. For two staggered infinite circular cylinders, $Re_D = 3.2\times10^4$-7.3×10^4.

As α becomes higher than the critical angle (Figs. 4.6 to 4.9), the St of the upstream cylinder keeps increasing while the St of the downstream cylinder begins to decrease, indicating that unlike the closely spaced configuration, where the two cylinders shed vortices as a group, for the moderate spaced configurations, Kármán vortex shedding occurs separately and distinctly from both cylinders for most α. The distinction between the St values from the upstream cylinder and downstream cylinder is caused by

the different flow patterns compared to those of closely spaced cylinders (Kiya et al., 1980; Gu and Sun, 1999; Sumner et al., 2000). The two cylinders at moderate pitch ratios are further spaced so that more approach flow can penetrate into the gap between the cylinders at higher incidence angles. The gap flow is deflected toward the upstream cylinder and results in two distinct near-wake regions behind the upstream cylinder and downstream cylinder. The upstream cylinder has a short and narrow near-wake region due to the deflection of the gap flow and therefore vortex shedding from the upstream cylinder occurs at a Strouhal number much higher than the single cylinder. Accordingly, the vortex shedding from the wide near-wake region behind the downstream cylinder corresponds to a Strouhal number lower than that of the single cylinder (Sumner et al., 2000, 2005).

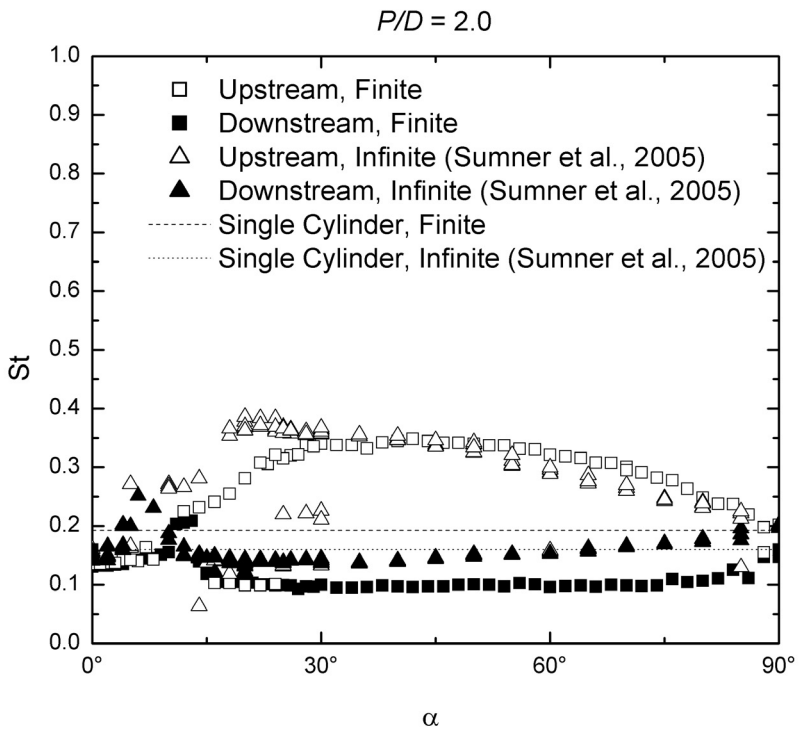

Figure 4.7. Strouhal number data for two moderately spaced staggered circular cylinders, P/D = 2, z/H = 0.5. Symbols as in Figure 4.2. For two staggered finite circular cylinders, Re_D = 2.4×10^4, AR = 9, δ/H = 0.4. For two staggered infinite circular cylinders, $Re_D = 3.2\times10^4$-7.3×10^4.

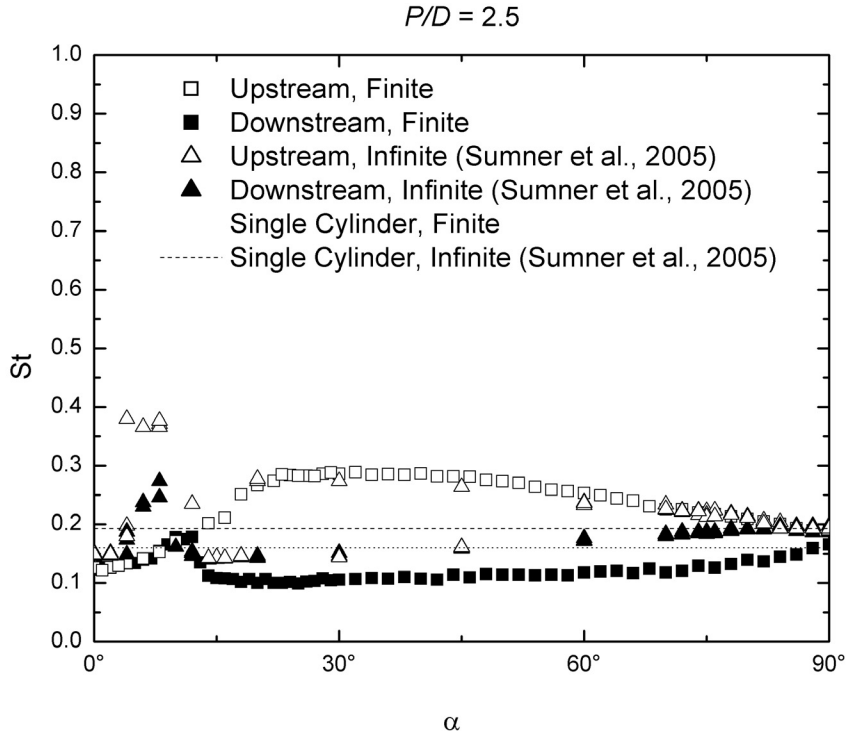

Figure 4.8. Strouhal number data for two moderately spaced staggered circular cylinders, P/D = 2.5, z/H = 0.5. Symbols as in Figure 4.2. For two staggered finite circular cylinders, $Re_D = 2.4\times10^4$, AR = 9, δ/H = 0.4. For two staggered infinite circular cylinders, $Re_D = 3.2\times10^4$-7.3×10^4.

The general behaviour of the Strouhal number for the two moderately spaced staggered finite cylinders (Figs. 4.6 to 4.9) is still similar to the infinite cylinders except that for two infinite cylinders at P/D = 1.5 (Fig. 4.6) and 2.5 (Fig. 4.8), there are maximum values of St = 0.63 and St = 0.37, respectively, detected at the critical angles (Sumner et al., 2005), which is not seen for the case of finite cylinders. For P/D = 1.5 (Fig. 4.6), St measured behind the upstream cylinder continues to increase when α is larger than the critical incidence angle until $\alpha \approx 45°$ where the St attains a maximum value of St = 0.47 and then drops gradually to St = 0.28 as α reaches 90°. It can be

imagined that when the two cylinders are arranged at $\alpha \approx 45°$ and $P/D = 1.5$ (Fig. 4.6), the deflection angle of the gap flow reaches a maximum value at which a very short and narrow near-wake region is constrained behind the upstream cylinder by the gap flow, leading to a maximum vortex shedding frequency. In contrast, the St measured behind the downstream cylinder drops to St = 0.09 when α becomes larger than the critical incidence angle and almost remains the same value all the way to $\alpha = 90°$, only rising slightly to St = 0.1 with α approaching to 90°. Similar phenomena happen for $P/D = 2$, 2.5 and 3 (Figs. 4.7, 4.8, and 4.9, respectively). However, due to the two cylinders being spaced further apart, both the maximum value of the St, and the incidence angle where the maximum St is obtained, decrease. Compared to the results of two moderately spaced *infinite* circular cylinders, the St values measured from the upstream *finite* cylinder are close to those of the upstream infinite cylinder, but the values of St for the downstream cylinder are lower for the finite-cylinder case.

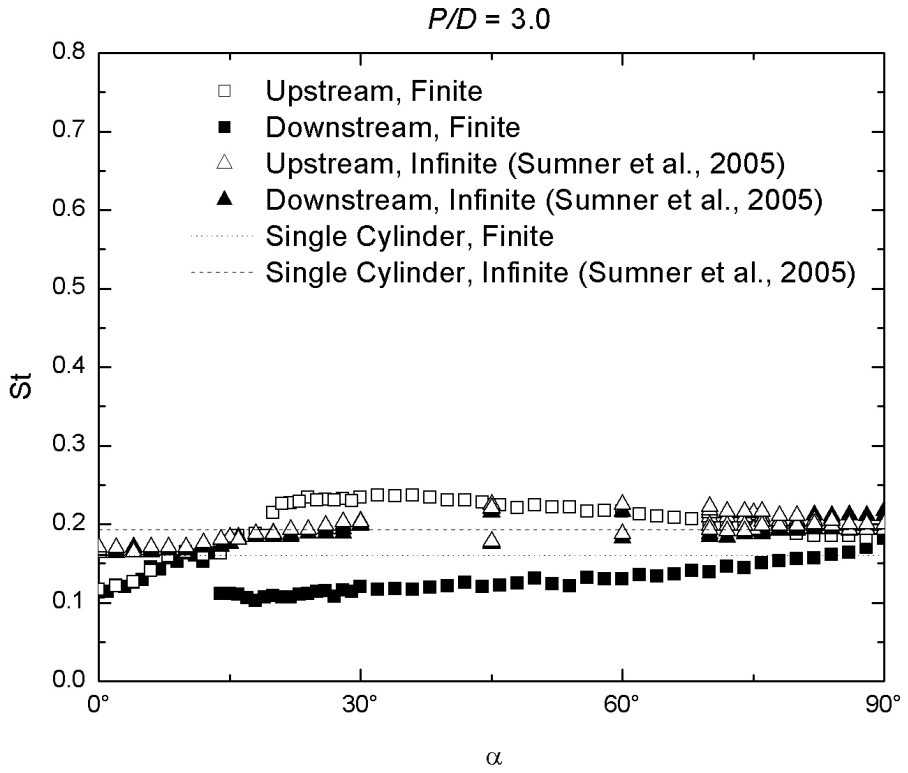

Figure 4.9. Strouhal number data for two moderately spaced staggered circular cylinders, P/D = 3, z/H = 0.5. Symbols as in Figure 4.2. For two staggered finite circular cylinders, $Re_D = 2.4\times10^4$, AR = 9, δ/H = 0.4. For two staggered infinite circular cylinders, $Re_D = 3.2\times10^4$-7.3×10^4.

Regarding the power spectra, Fig. 4.10 (P/D = 1.5) and Fig. 4.11 (P/D = 2) show that two peaks are measured behind the upstream cylinder for a wide range of α higher than the critical angle, and the lower Strouhal number of the two peaks equals the Strouhal number measured behind the downstream cylinder. With P/D increasing, the difference between the Strouhal numbers of the upstream cylinder and downstream cylinder becomes smaller, which means that the interference between the two cylinders is weakened due to the two cylinders becoming further apart.

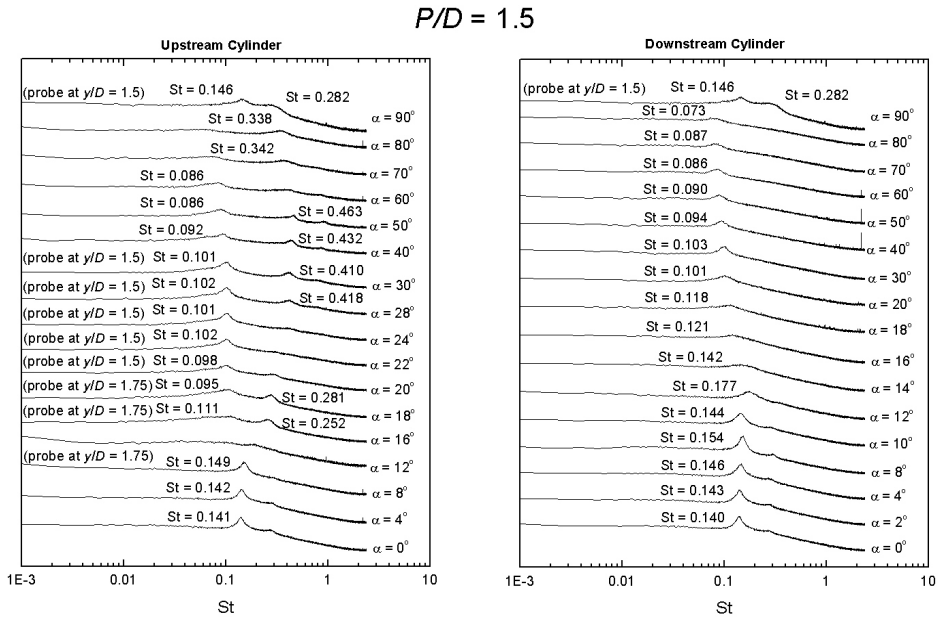

Figure 4.10. Selected power spectra, as a function of incidence angle, for moderately spaced staggered cylinders: P/D = 1.5, z/H = 0.5, Re_D = 2.4×10^4. Each spectrum represents 250 averages. The vertical (logarithmic) scale is arbitrary, but the same scale is used for each spectrum.

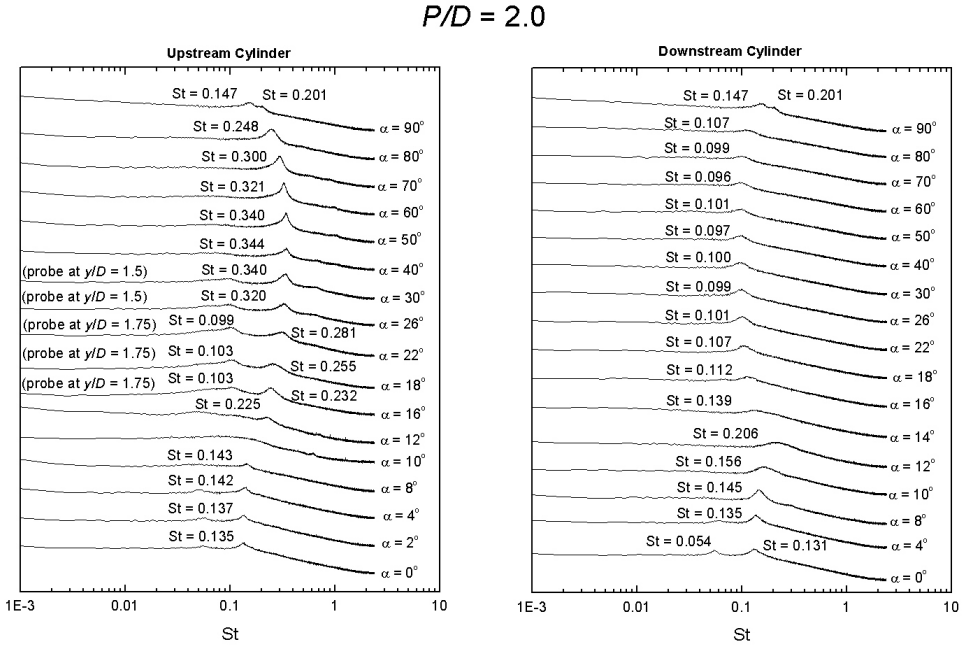

Figure 4.11. Selected power spectra, as a function of incidence angle, for moderately spaced staggered cylinders: P/D = 2, z/H = 0.5, Re_D = 2.4×10^4. Each spectrum represents 250 averages. The vertical (logarithmic) scale is arbitrary, but the same scale is used for each spectrum.

For the moderately spaced configurations, it is seen from Fig. 4.10 (P/D = 1.5), Fig. 4.11 (P/D = 2), Fig. 4.12 (P/D = 2.5) and Fig. 4.13 (P/D = 3), that the vortex shedding peaks measured behind the upstream and downstream cylinders are weak and broad-banded, or even disappear, around the critical incidence angle. For P/D = 1.5 (Fig. 4.10), strong peaks are detected behind the two cylinders at small angles of incidence ($\alpha < 12°$), where the shear layer from the upstream cylinder can reattach onto the downstream cylinder, leading to the same vortex shedding frequency for both cylinders. As a result, the two cylinders still behave similar to a single bluff body. A similar phenomenon occurs at P/D = 2, 2.5, and 3 (Figs. 4.11 to 4.13), but the peaks in the power spectra of the upstream cylinder are very weak and more broad-banded, indicating that a weakened vortex shedding process occurs behind the upstream cylinder. This result is consistent with the characteristics of the shear layer reattachment flow pattern (SLR) reported by Sumner et al. (2000).

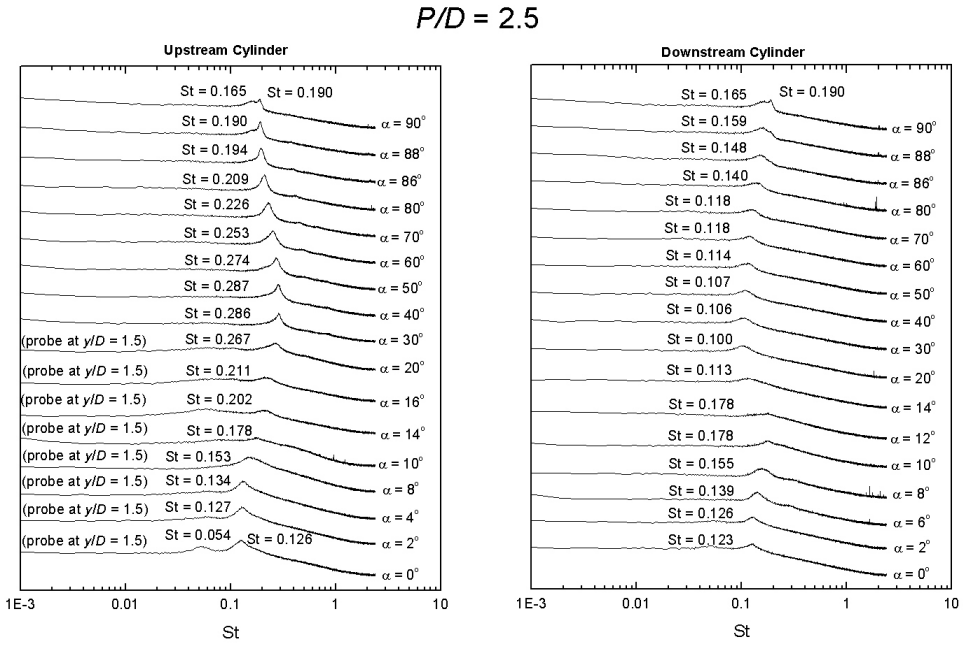

Figure 4.12. Selected power spectra, as a function of incidence angle, for moderately spaced staggered cylinders: P/D = 2.5, z/H = 0.5, $Re_D = 2.4\times10^4$. Each spectrum represents 250 averages. The vertical (logarithmic) scale is arbitrary, but the same scale is used for each spectrum.

With α increasing, the inner shear layer from the upstream cylinder can no longer reattach on the downstream cylinder. Instead, it is deflected into the gap between the two cylinders and forms the induced separation flow pattern (IS) (Sumner et al., 2000). Then the flow further develops into the vortex pairing, splitting and enveloping flow patterns (VPE, VPSE) (Sumner et al., 2000) at large α, signified by the stronger and sharper peaks in the power spectra. For P/D = 1.5 (Fig. 4.10) and P/D = 2 (Fig. 4.11), the outer shear layer shed from the upstream cylinder is highly deflected away from the flow axis when α is between 15° and 30°; the hot-wire probe had to be moved further to y/D = 1.5 and y/D = 1.75 to capture the vortex shedding peaks. In addition, two distinct Strouhal numbers are measured behind the upstream cylinder for these two pitch ratios. Based on the

measurement location, the higher Strouhal number generally is related to the vortex shedding from the upstream cylinder and the lower Strouhal number broadly corresponds to vortex shedding from the downstream cylinder. For P/D = 2.5 (Fig. 4.12) and P/D = 3 (Fig. 4.13), there is only one peak found behind upstream cylinder, as the downstream cylinder now is further away from the upstream cylinder and the deflection angle of the gap flow toward the upstream cylinder is smaller at the larger pitch ratios.

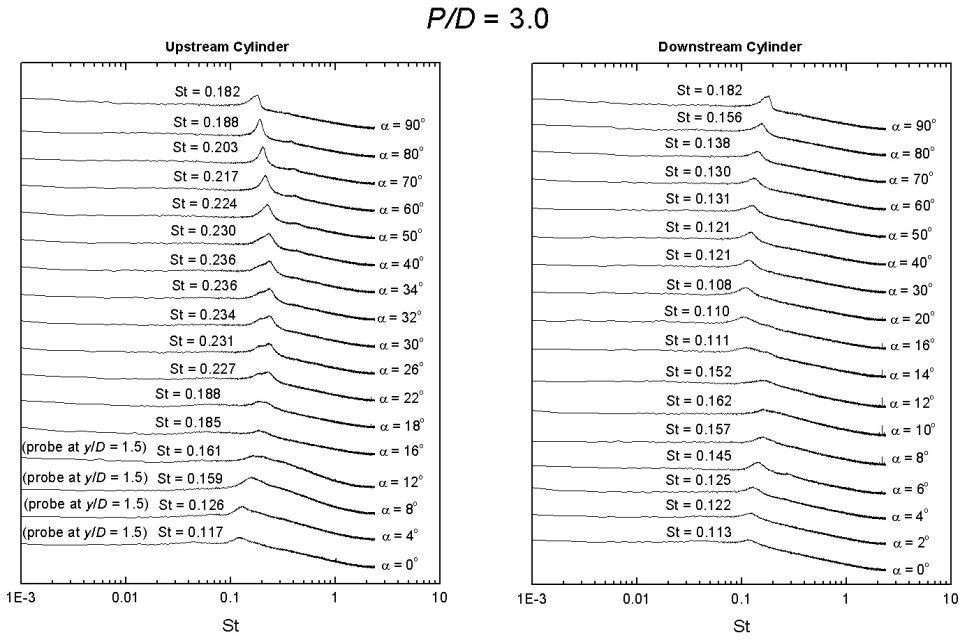

Figure 4.13. Selected power spectra, as a function of incidence angle, for moderately spaced staggered cylinders: P/D = 3, z/H = 0.5, $Re_D = 2.4\times10^4$. Each spectrum represents 250 averages. The vertical (logarithmic) scale is arbitrary, but the same scale is used for each spectrum.

For P/D = 1.5, 2 and 2.5 (Figs. 4.10, 4.11, and 4.12, respectively), when the two cylinders are arranged side-by-side (corresponding to α = 90°), two peaks are measured. This is consistent with the results of Sumner et al. (1999, 2000) that the gap flow is biased towards one of the cylinders, resulting in one cylinder with a narrow near-wake

region and the other cylinder with a wide near-wake region. As P/D increases, the two Strouhal numbers become closer in value and change to a single St at $P/D = 3$, indicating the biased flow pattern disappears and there is no strong interaction between the vortex shedding from the two cylinders (a synchronized vortex shedding flow pattern (SVS) result (Sumner et al., 2000)).

4.3.1.3 Widely Spaced Configurations (P/D = 4, 5)

For widely spaced staggered configurations, the behavior of the Strouhal number data, shown in Fig. 4.14 ($P/D = 4$) and Fig. 4.15 ($P/D = 5$), becomes less complex. There is no apparent critical incidence angle and generally the same Strouhal numbers are measured behind the upstream cylinder and downstream cylinder, except from $30° < \alpha < 90°$ for $P/D = 4$ (Fig. 4.14) and from $45° < \alpha < 82°$ for $P/D = 5$ (Fig. 4.15), although the difference between the two St values is small. Over the range of α where two St numbers are measured, the higher St is associated with the vortex shedding from the upstream cylinder and the lower St is associated with vortex shedding from the downstream cylinder. Overall, the Strouhal numbers remain close to the value of a single finite circular cylinder (St = 0.16). The results indicate that there still exists some interference between the two cylinders, but the two cylinders behave more independently and shed vortices more like two isolated, single finite circular cylinders due to the fact that one cylinder now is far away from the other.

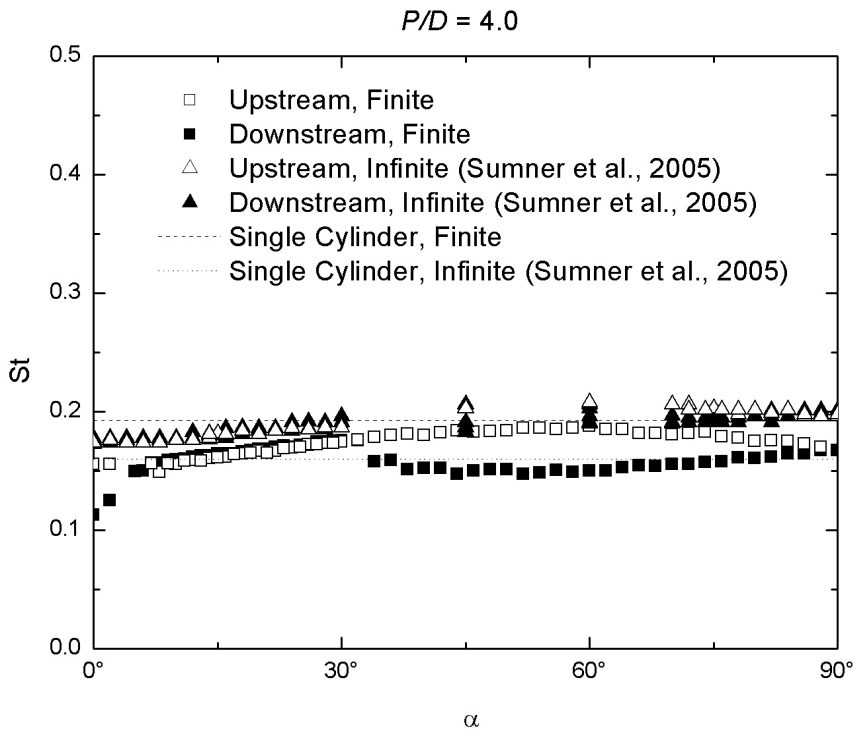

Figure 4.14. Strouhal number data for two widely spaced staggered circular cylinders, $P/D = 4$, $z/H = 0.5$. Symbols as in Figure 4.2. For two staggered finite circular cylinders, $Re_D = 2.4\times10^4$, AR = 9, $\delta/H = 0.4$. For two staggered infinite circular cylinders, $Re_D = 3.2\times10^4$-7.3×10^4.

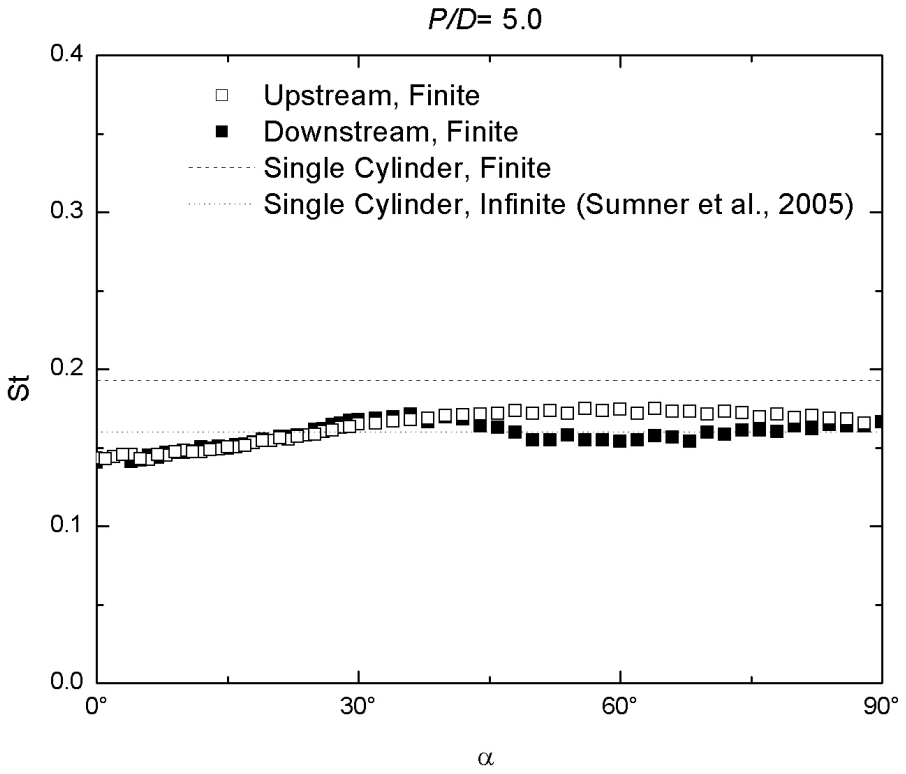

Figure 4.15. Strouhal number data for two widely spaced staggered circular cylinders, $P/D = 5$, $z/H = 0.5$, $Re_D = 2.4\times10^4$, AR = 9, $\delta/H = 0.4$. Symbols as in Figure 4.2.

It is noted that for $P/D = 3$, two staggered *infinite* cylinders illustrate the widely spaced behavior (Sumner et al., 2005) while the *finite* cylinders still behave similar to moderately spaced cylinders. This difference is caused by the variation of the vortex formation length along the height of the finite cylinder. Since the St of the finite cylinders is measured at the mid-height, where the vortex formation length attains its maximum value and is longer than that of the infinite cylinder, the two finite cylinders have a longer interference region at mid-height, which delays the switchover from the moderately spaced behavior to the widely spaced behavior.

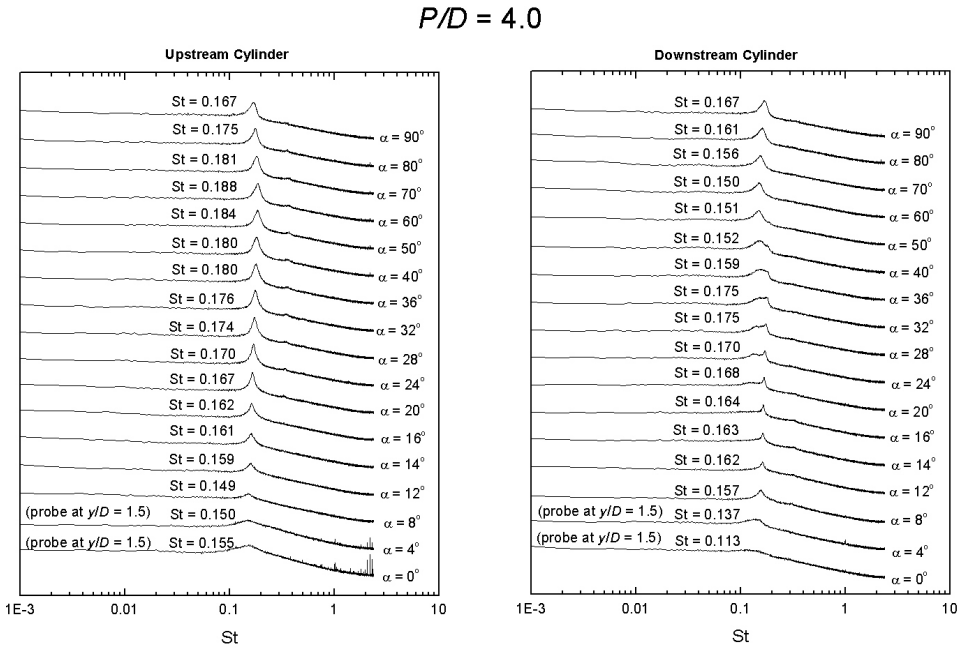

Figure 4.16. Selected power spectra, as a function of incidence angle, for widely spaced staggered cylinders: P/D = 4, z/H = 0.5, $Re_D = 2.4\times10^4$. Each spectrum represents 250 averages. The vertical (logarithmic) scale is arbitrary, but the same scale is used for each spectrum.

Concerning the power spectra, the two configurations of P/D = 4 and 5 both possess the characteristic of the widely spaced configuration that weak vortex shedding peaks (Figs. 4.16 and 4.17) are obtained behind the downstream cylinder at α =12°-14°. This is similar to what was observed by Sumner et al. (2005) for two widely spaced *infinite* cylinders, and is the evidence of the "outer lift peak" (where the mean lift coefficient on the downstream cylinder attains a local maximum value with incidence angle (Zdravkovich and Pridden, 1977; Sumner et al., 2005)).

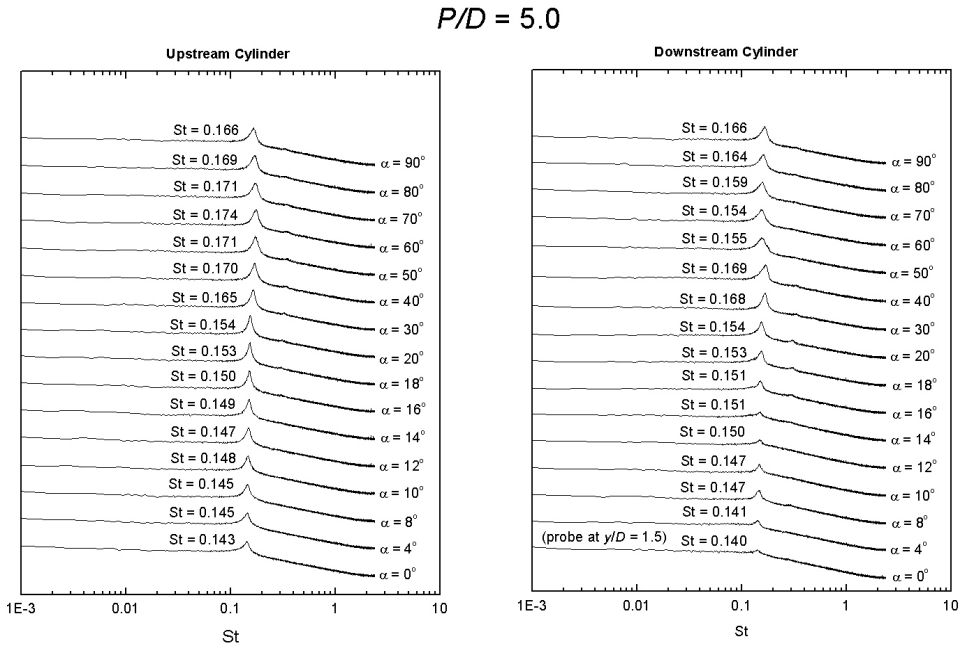

Figure 4.17. Selected power spectra, as a function of incidence angle, for widely spaced staggered cylinders: P/D = 5, z/H = 0.5, $Re_D = 2.4\times10^4$. Each spectrum represents 250 averages. The vertical (logarithmic) scale is arbitrary, but the same scale is used for each spectrum.

For the power spectra measured behind two cylinders at P/D = 4 (Fig. 4.16), broad-banded peaks are seen at the tandem and nearly tandem configurations behind both cylinders and are caused by the weakened or suppressed vortex shedding from the upstream cylinder. The probe had to be moved to find discernable peaks. The peaks are strong at higher incidence angles where the flow pattern changes to the synchronized vortex shedding flow pattern (SVS) (Sumner et al., 2000). There is a transition of the peaks from high St to low St between α = 20° and 40° behind the downstream cylinder, showing the transition process of the flow pattern from vortex impingement (VI) to synchronized vortex shedding (SVS) (Sumner et al., 2000).

For $P/D = 5$ (Fig. 4.17), the peaks of the power spectra are strong all the way from $\alpha = 0°$ to 90° for the upstream cylinder, but for the downstream cylinder weak and broad-banded peaks are observed for $\alpha < 20°$. The strong vortex shedding from the upstream cylinder and its suppression behind the downstream cylinder at small α coincides with the vortex impingement flow pattern (VI) (Sumner et al., 2000).

4.3.2 Strouhal Number Measurements along the Heights of the Cylinders

The most essential distinction between the flow patterns of the infinite circular cylinder and the finite circular cylinder is that the flow field around the infinite cylinder can be simply treated as two-dimensional while the flow structure for the finite cylinder is strongly three-dimensional due to the existence of its base (cylinder-wall junction) and free end. The free end causes the formation of a pair of counter-rotating vortices, which induces strong "downwash" flow from the top of the finite cylinder. This "downwash" flow extends in the near-wake region and interacts with the regular vortex shedding from the two sides of the cylinder, resulting in weakened or suppressed vortex shedding and a three-dimensional flow structure near the free end of the cylinder. On the other hand, the regular vortex shedding around the base of the finite cylinder is affected by the flat-plate boundary layer and the steady horseshoe vortex structure generated at the base of the cylinder. These two factors both contribute to the highly three-dimensional and complicated flow behavior behind the finite cylinder.

When two finite circular cylinders are arranged in staggered configuration, the

interaction between two “downwash” flows from the two cylinders, along with the strong flow interference happening at the bases of the two cylinders, makes the flow pattern even more complex and challenging to investigate. Until now, limited studies have been done for the two finite cylinders, especially arranged in a staggered configuration.

In this section, results are presented where the Strouhal number is measured along the heights of the two staggered finite circular cylinders, but only at selected incidence angles and pitch ratios representing closely spaced, moderately spaced and widely spaced configurations. The hot-wire probe was fixed at x/D = 3 and y/D = 1, with the wall-normal position allowed to change from z/H = 0.05 to 1.05 at $\Delta z/H$ = 0.05.

4.3.2.1 Closely Spaced Configurations (P/D = 1.125 and 1.25)

When the two finite circular cylinders are arranged in a tandem (or inline) configuration (corresponding to α = 0°) at P/D = 1.125 and 1.25, it is observed in Fig. 4.18 and Fig. 4.19, respectively, that the shape of power spectra varies significantly along the height of the cylinder. For P/D = 1.125 (Fig. 4.18), the peaks of power spectra shift from a high vortex shedding frequency (St = 0.17) near base of the finite cylinder to a low vortex shedding frequency (St = 0.13) around the mid-height of the cylinder, and finally change back to a higher vortex shedding frequency (St = 0.20), but become broad-banded, near the free end. For P/D = 1.25 (Fig. 4.19), the peaks of power spectra shift from St = 0.16 to St = 0.14 at z/H = 0.15 and then remain the same all the way up to the free end of the cylinder, with only the shape of the peak changing. The behaviour of

the peaks and the Strouhal number magnitude indicate that the flow pattern varies along the heights of the cylinders, which was also seen by Luo et al. (1996)

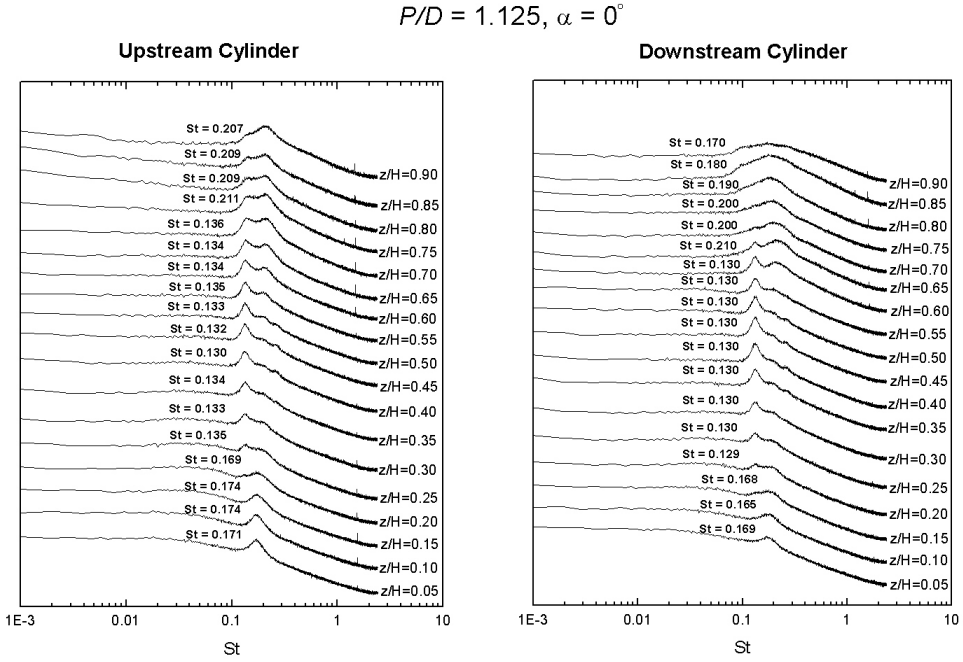

Figure 4.18. Power spectra along the height of upstream and downstream cylinders at P/D = 1.125, α = 0°, $\mathrm{Re}_D = 2.4\times10^4$, AR = 9 and δ/H = 0.4. Each spectrum represents 250 averages. The vertical (logarithmic) scale is arbitrary, but the same scale is used for each spectrum.

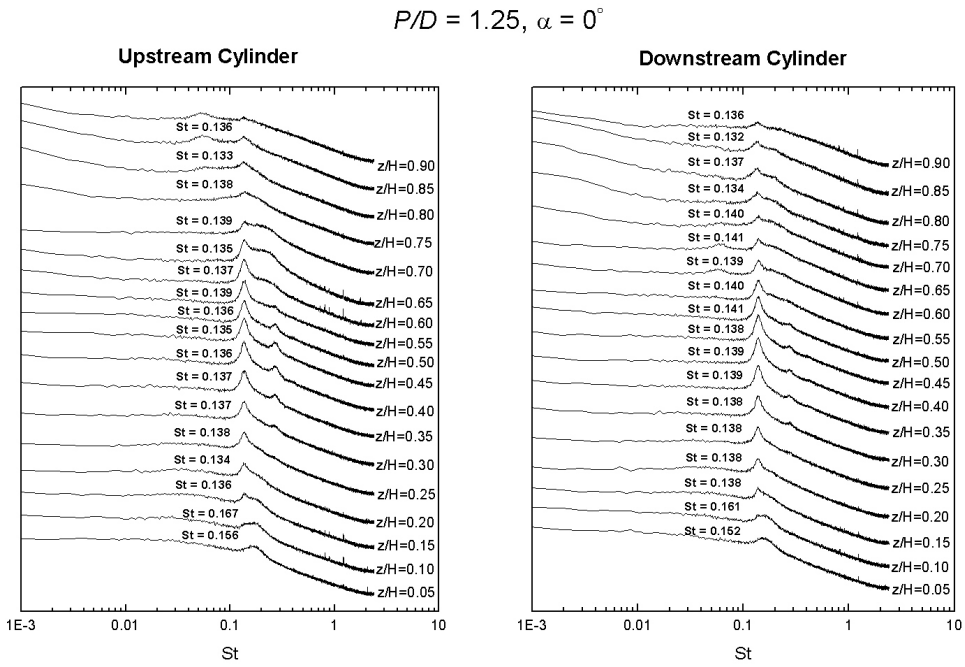

Figure 4.19. Power spectra along the height of upstream and downstream cylinders at P/D = 1.25, α = 0°, $Re_D = 2.4\times10^4$, AR = 9 and δ/H = 0.4. Each spectrum represents 250 averages. The vertical (logarithmic) scale is arbitrary, but the same scale is used for each spectrum.

Based on the velocity field information measured by the seven-hole probe in a vertical plane along the wake centerline of a single finite circular cylinder (Fig. 4.20), it is seen that the length of recirculation region behind the single cylinder varies along the height of the cylinder, with a long region occurring around the middle of the cylinder and a short region found near the base and the free end, as a result of the effects of the "upwash" and "downwash flow".

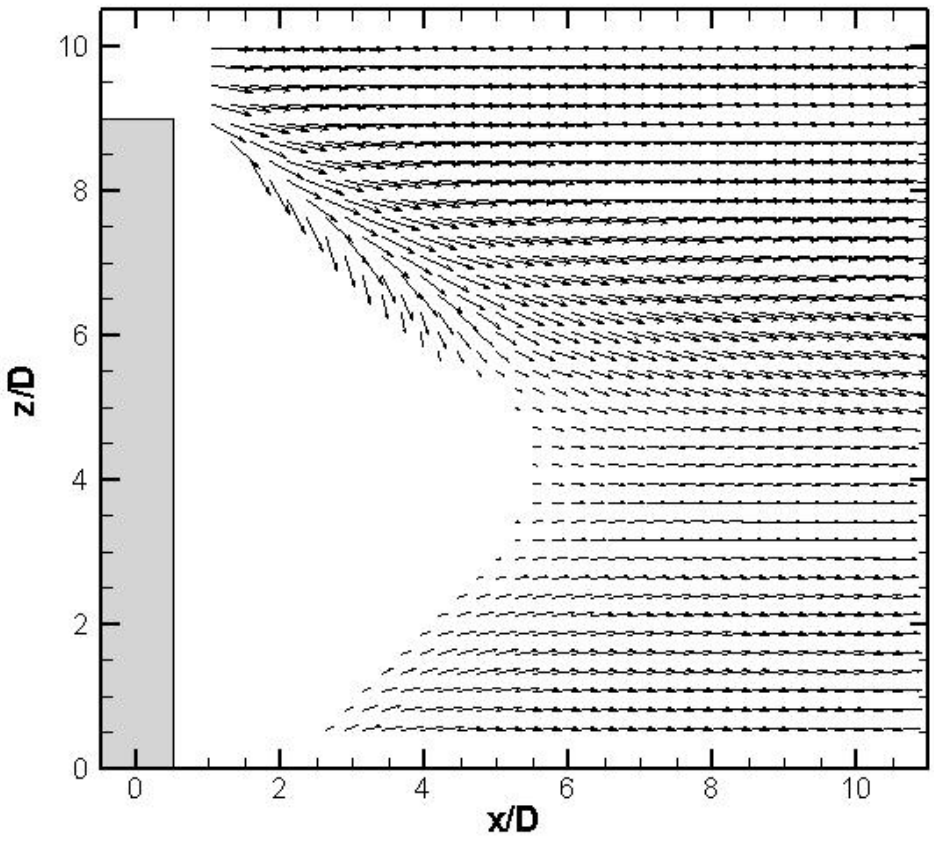

Figure 4.20. Time-averaged velocity field in a vertical plane along the wake centerline behind a single finite circular cylinder, $Re_D = 2.4\times10^4$, AR = 9 and $\delta/H = 0.4$.

When the downstream cylinder is placed close to the upstream cylinder at P/D = 1.125, the regular vortex shedding near the base of the *downstream* cylinder is strongly disturbed by the horseshoe vortex formed at the base of the *upstream* cylinder. It is also under the influence of flat-plate boundary layer, causing broad-banded peaks in the power spectra and a higher vortex shedding frequency near the base of the downstream cylinder. At the same pitch ratio, the "downwash" flow generated at the free end of upstream cylinder is blocked by the downstream cylinder and only part of the flow can travel down into the gap between the two cylinders, while the rest has to move over the downstream

cylinder and then descend to the near wake region; this leads to a complicated flow pattern behind the downstream cylinder.

As seen in the seven-hole-probe measurements in Fig. 4.21, an irregular-shaped discontinuous recirculation region is found behind the downstream cylinder and it is shorter and more uniform than the recirculation region of the single finite circular cylinder. The recirculation region behind the two tandem cylinders at P/D = 1.125 is divided into two parts, broadly corresponding to the two vortex shedding frequencies of St = 0.13 and 0.2, respectively. Furthermore, the "downwash" flow traveling down behind the downstream cylinder (Fig. 4.21) is much weaker than the case of the single cylinder (Fig. 4.20) and only reaches the height of z/D = 6 behind the downstream cylinder. Below the location of z/D = 6 (Fig. 4.21), another flow with downward velocity appears and meets with the upwash flow originated from the base of the cylinder.

As the two tandem cylinders are spaced further apart to P/D = 1.25, the influence of the tip and end becomes weaker and therefore the vortex shedding frequency almost remains the same along the height of the cylinders except for a slight change near the base of the cylinder, as seen in Fig. 4.19.

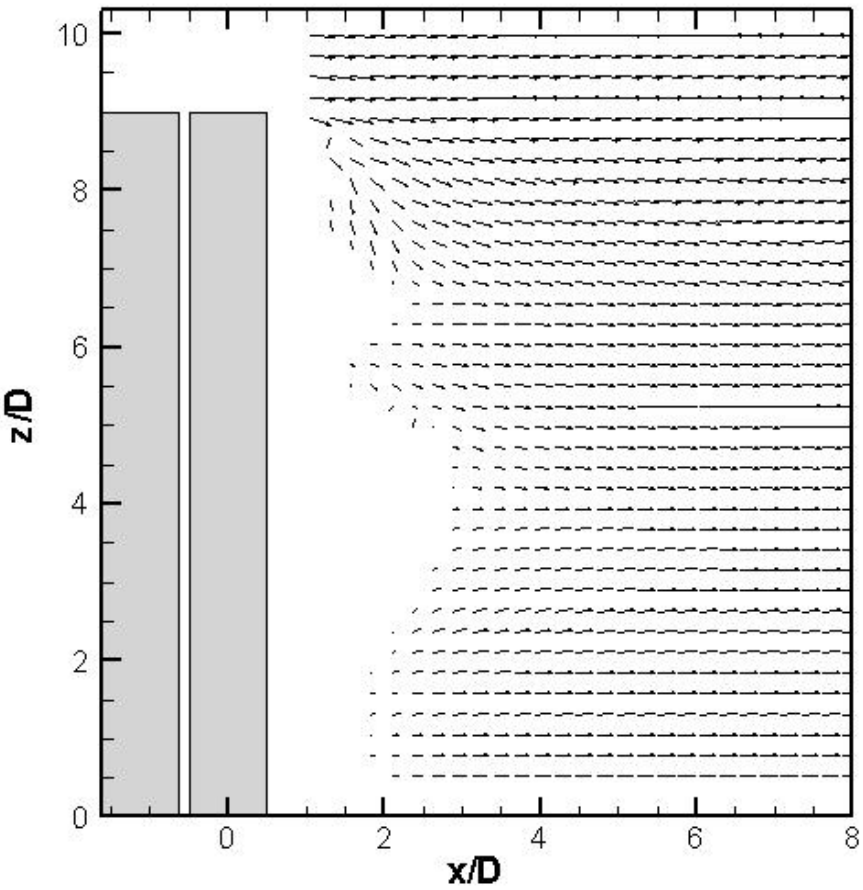

Figure 4.21. Time-averaged velocity field in a vertical plane along the wake centerline, $P/D = 1.125$, $\alpha = 0°$, $Re_D = 2.4\times10^4$, AR = 9 and $\delta/H = 0.4$.

For two closely spaced staggered cylinders at small α, such as at $\alpha = 30°$, as shown in Fig. 4.22 (for $P/D = 1.125$) and Fig. 4.23 (for $P/D = 1.25$), the power spectra along the height of the cylinders show similar characteristics. The peaks of the power spectra are broad-banded and weak near the ground due to the effects of the flat-plate boundary layer and the horseshoe vortex on the Kármán vortex shedding. With increasing z/H, the influence of the boundary layer and the horseshoe vortex becomes negligible and at the middle section of the cylinders the vortices are shedding similar to infinite cylinders. The peaks become sharper than that at the base and the strongest peak is

obtained around the mid-height of the cylinder. As the free end is approached, the "downwash" flow induced by the counter-rotating pair of tip vortices originated at the free end has a complex interaction with the Kármán vortex shedding from both sides of the cylinder, which weakens the vortex shedding and makes it undetected. The peaks of the power spectra near the tip become weaker or even disappear. Weak peaks in the power spectra (Figs. 4.22 and 4.23) mostly are observed below $z/H = 0.25$ and above $z/H = 0.60$ due to the flow interference caused by the base and free end, respectively, indicating that the tip effect can extend to $z/H = 0.60$ and the combined influence of the horseshoe vortex and boundary layer can reach to $z/H = 0.25$, although $\delta/H = 0.4$.

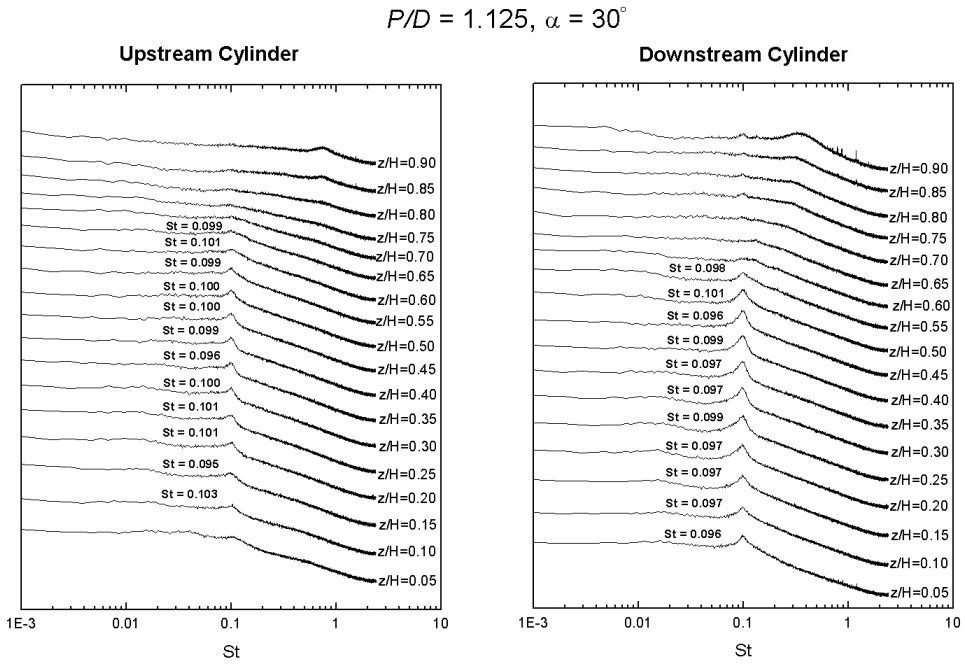

Figure 4.22. Power spectra along the height of upstream and downstream cylinders at $P/D = 1.125$, $\alpha = 30°$, $Re_D = 2.4\times10^4$, AR = 9 and $\delta/H = 0.4$. Each spectrum represents 250 averages. The vertical (logarithmic) scale is arbitrary, but the same scale is used for each spectrum.

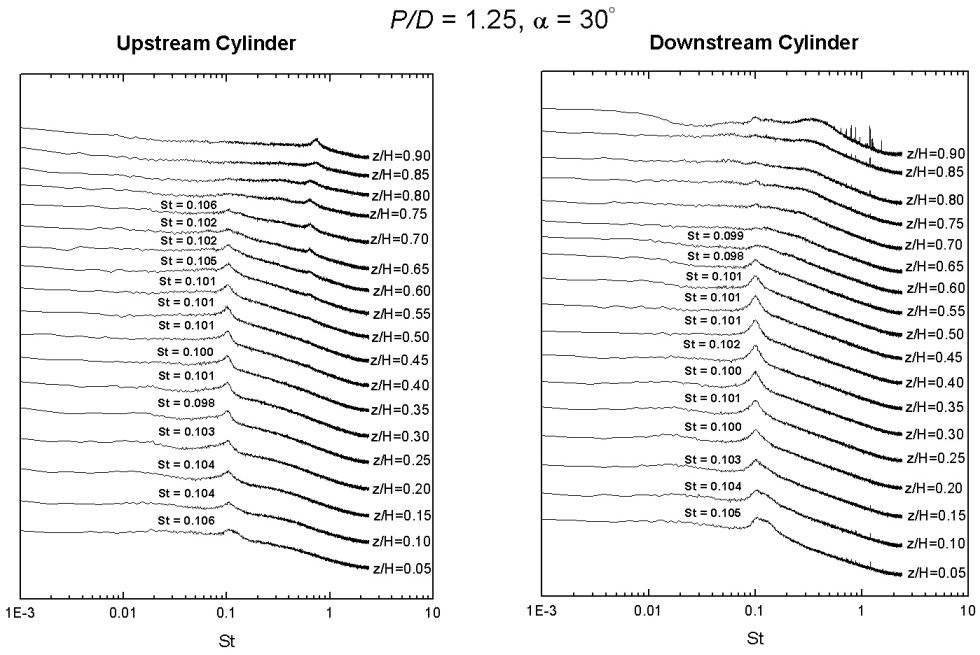

Figure 4.23. Power spectra along the height of upstream and downstream cylinders at P/D = 1.25, α = 30°, $Re_D = 2.4\times10^4$, AR = 9 and δ/H = 0.4. Each spectrum represents 250 averages. The vertical (logarithmic) scale is arbitrary, but the same scale is used for each spectrum.

When the two closely spaced cylinders are placed at large α, as shown in Figs. 4.24, 4.25, 4.26 and 4.27, the peaks of the power spectra are extremely weak along the whole cylinder or there is no peak at all, in particular for the upstream cylinder. This may result from base-bleed flow coming out through the narrow gap between the two cylinders and interacting with the free shear layers, causing a change in the vortex formation length and interruption of the Kármán shedding. The influence of base-bleed flow increases at the higher α and flow can be deflected to either the upstream cylinder or the downstream cylinder. Sumner et al. (2000) revealed a wide variation in the base-bleed flow deflection angle and the strength of the base flow at different α.

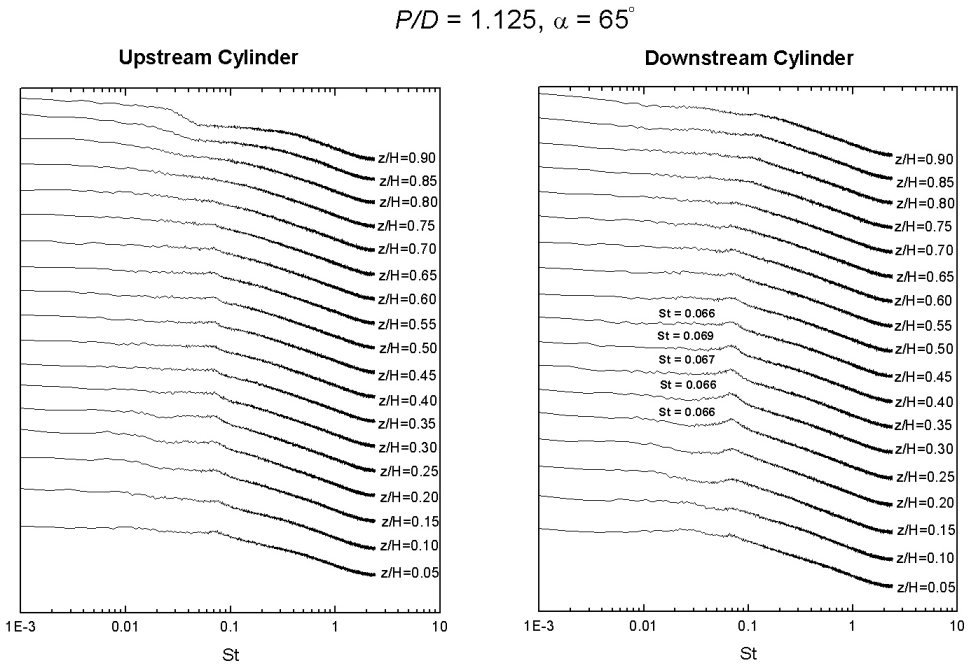

Figure 4.24. Power spectra along the height of upstream and downstream cylinders at P/D = 1.125, α = 65°, $\mathrm{Re}_D = 2.4\times10^4$, AR = 9 and δ/H = 0.4. Each spectrum represents 250 averages. The vertical (logarithmic) scale is arbitrary, but the same scale is used for each spectrum.

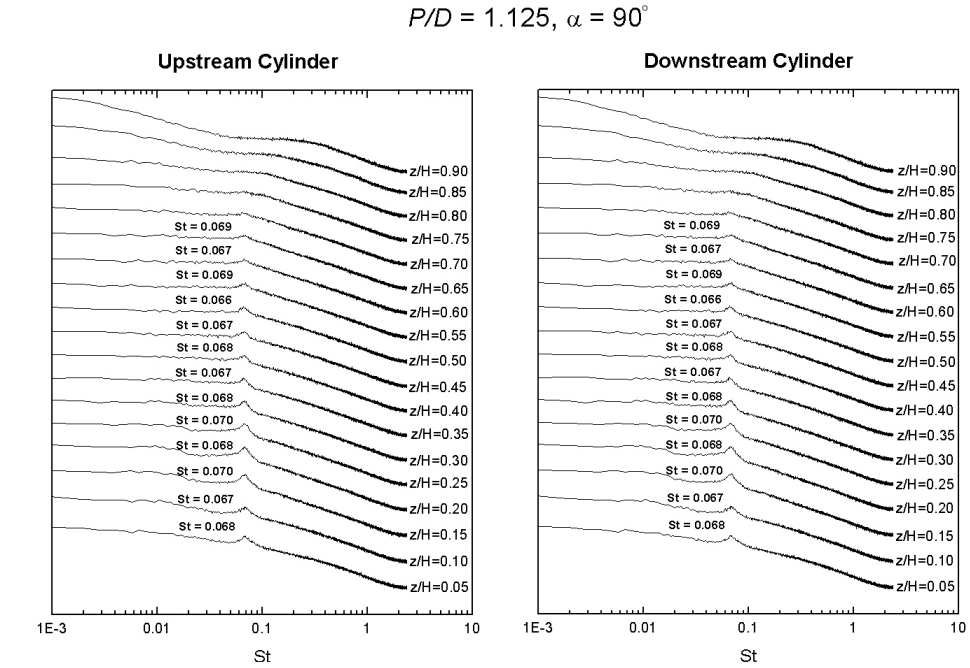

Figure 4.25. Power spectra along the height of upstream and downstream cylinders at P/D = 1.125, α = 90°, $\mathrm{Re}_D = 2.4\times10^4$, AR = 9 and δ/H = 0.4. Each spectrum represents 250 averages. The vertical (logarithmic) scale is arbitrary, but the same scale is used for each spectrum.

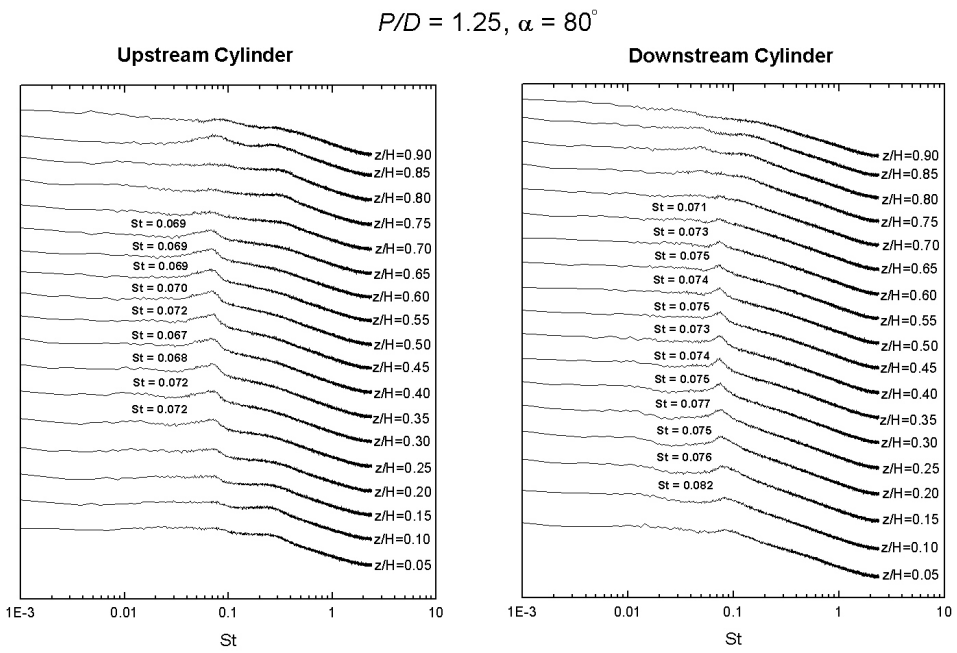

Figure 4.26. Power spectra along the height of upstream and downstream cylinders at $P/D = 1.25$, $\alpha = 80°$, $\mathrm{Re}_D = 2.4\times10^4$, AR = 9 and $\delta/H = 0.4$. Each spectrum represents 250 averages. The vertical (logarithmic) scale is arbitrary, but the same scale is used for each spectrum.

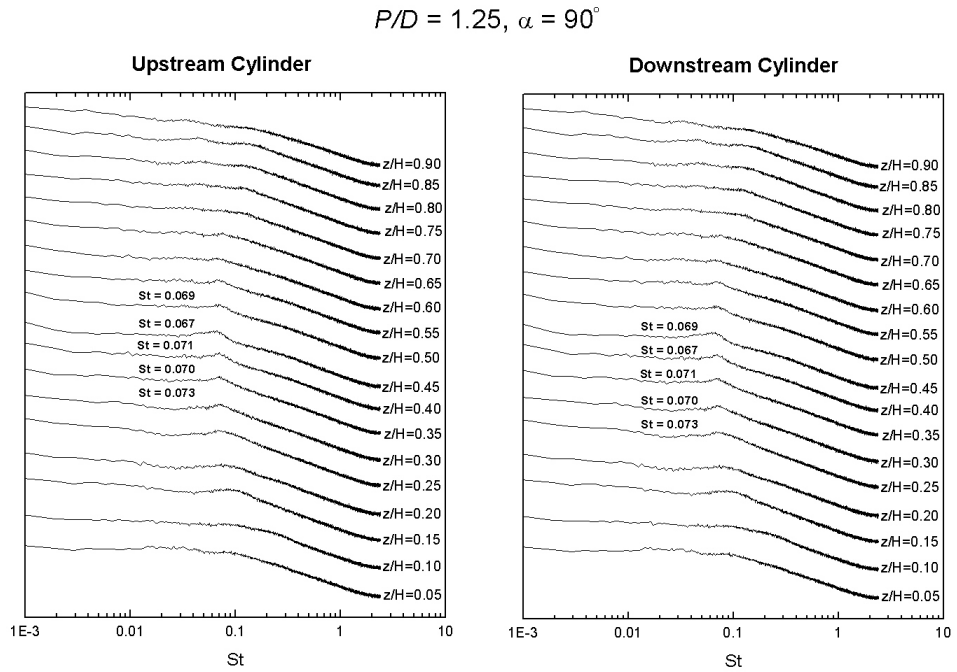

Figure 4.27. Power spectra along the height of upstream and downstream cylinders at $P/D = 1.25$, $\alpha = 90°$, $\mathrm{Re}_D = 2.4\times10^4$, AR = 9 and $\delta/H = 0.4$. Each spectrum represents 250 averages. The vertical (logarithmic) scale is arbitrary, but the same scale is used for each spectrum.

4.3.2.2 Moderately Spaced Configuration (P/D = 2 and 2.5)

As seen in Fig. 4.28 and Fig. 4.29, for the two moderately spaced finite cylinders in the tandem configuration, i.e. at α = 0°, the effect of the ground plane on the downstream cylinder is much weaker than the closely spaced configuration and thus the peaks of the power spectra measured near the ground plane are sharper than the closely spaced configurations, but still weaker than the vortex shedding peaks at the middle section. An obvious distinction from the closely spaced configuration is that for P/D = 2.0 (Fig. 4.28), a low frequency (St = 0.06) is detected near the tip of the cylinder, which may indicate a low-frequency Kármán vortex shedding process. A similar phenomenon is found for P/D = 2.5 (Figs. 4.29). Seeing that the space between the two cylinders at moderately spaced configurations is large enough for the "downwash" flow to descend immediately behind the upstream cylinder, the "downwash" flow meets the front side of the downstream cylinder and interacts with vortex shedding at the upper part of the downstream cylinder, which may be responsible for a low vortex shedding frequency near the tip behind the downstream cylinder.

As seen from the seven-hole-probe wake measurements in the vertical plane along the centerline behind the two tandem cylinders at P/D = 2 (Fig. 4.30), there is also a short and irregularly shaped recirculation region similar to velocity field behind the two closely spaced cylinders (P/D = 1.125, Fig. 4.21). However, for P/D = 2, the downwash behind the downstream cylinder is much stronger than the case of P/D = 1.125.

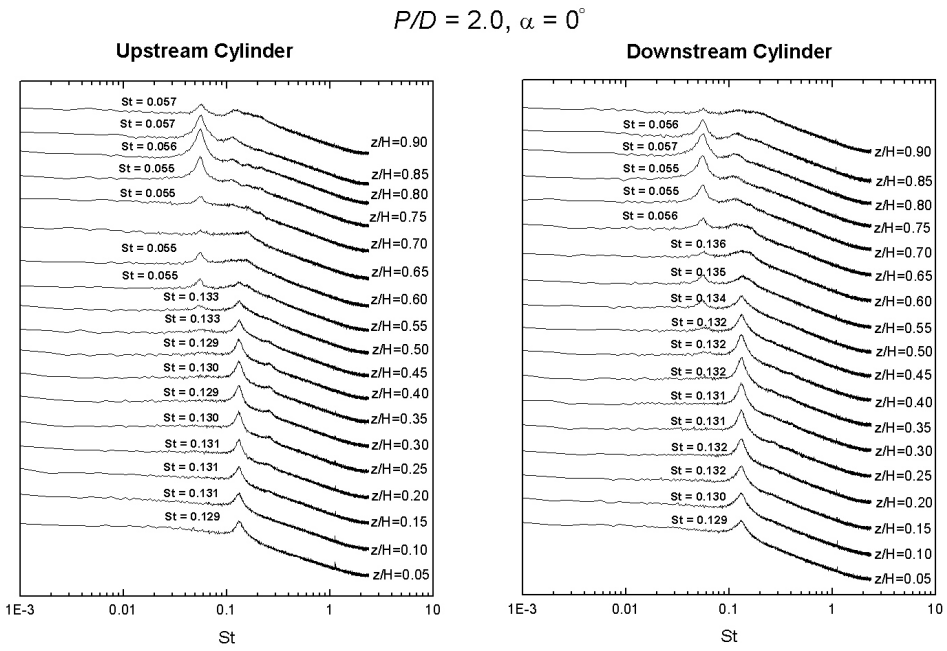

Figure 4.28. Power spectra along the height of upstream and downstream cylinders at P/D = 2, α = 0°, $\mathrm{Re}_D = 2.4\times10^4$, AR = 9 and δ/H = 0.4. Each spectrum represents 250 averages. The vertical (logarithmic) scale is arbitrary, but the same scale is used for each spectrum.

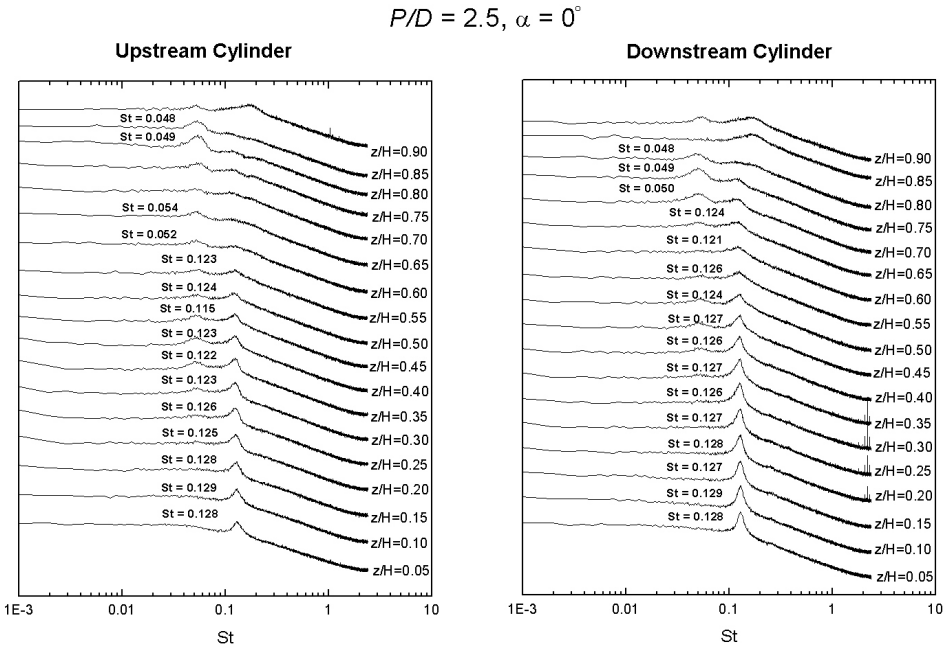

Figure 4.29. Power spectra along the height of upstream and downstream cylinders at P/D = 2.5, α = 0°, $\mathrm{Re}_D = 2.4\times10^4$, AR = 9 and δ/H = 0.4. Each spectrum represents 250 averages. The vertical (logarithmic) scale is arbitrary, but the same scale is used for each spectrum.

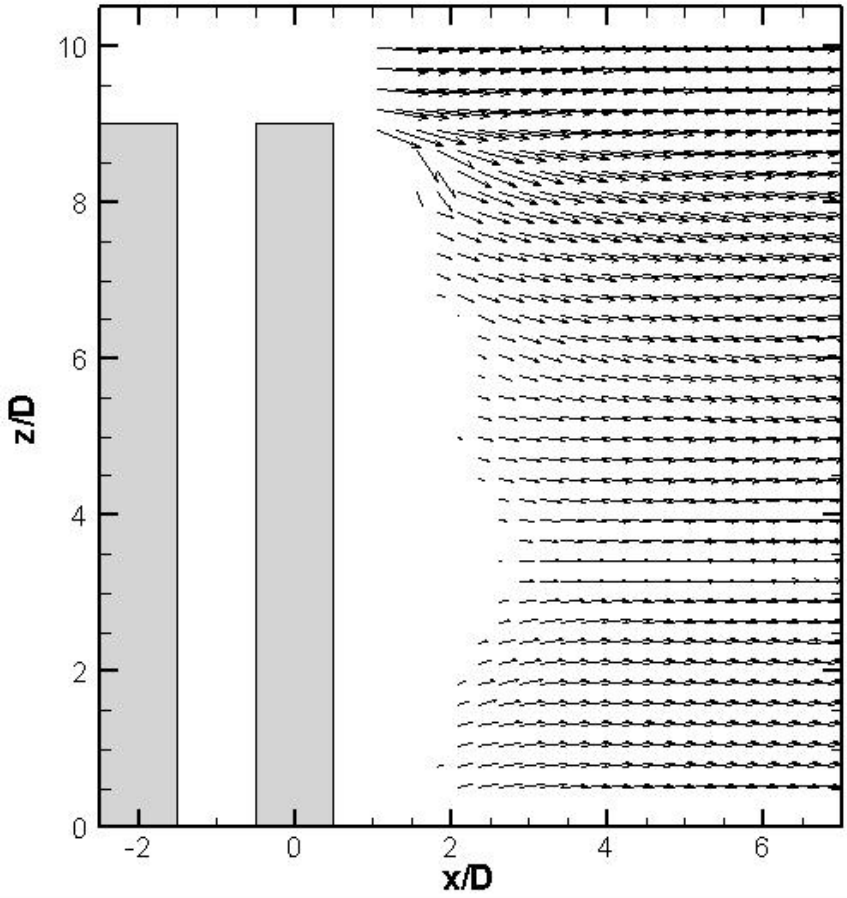

Figure 4.30. Time-averaged velocity field in a vertical plane along the wake centerline, $P/D = 2$, $\alpha = 0°$, $Re_D = 2.4\times10^4$, AR = 9 and $\delta/H = 0.4$.

For $P/D = 2$ and 2.5, when the cylinders are arranged side-by-side ($\alpha = 90°$), Figs. 4.31 and 4.32 show that two peaks are measured at the lower half of the cylinder for $P/D = 2$ and at the middle section for $P/D = 2.5$, where the gap flow is biased towards one of the cylinders alternately, forming the "switching flow pattern". A similar biased flow pattern around the two side-by-side finite cylinders was observed by Park and Lee (2003). However, for $z/H > 0.55$, the two peaks are replaced by a single broad-banded peak, indicating the biased flow pattern no longer persists and is disturbed by the downwash.

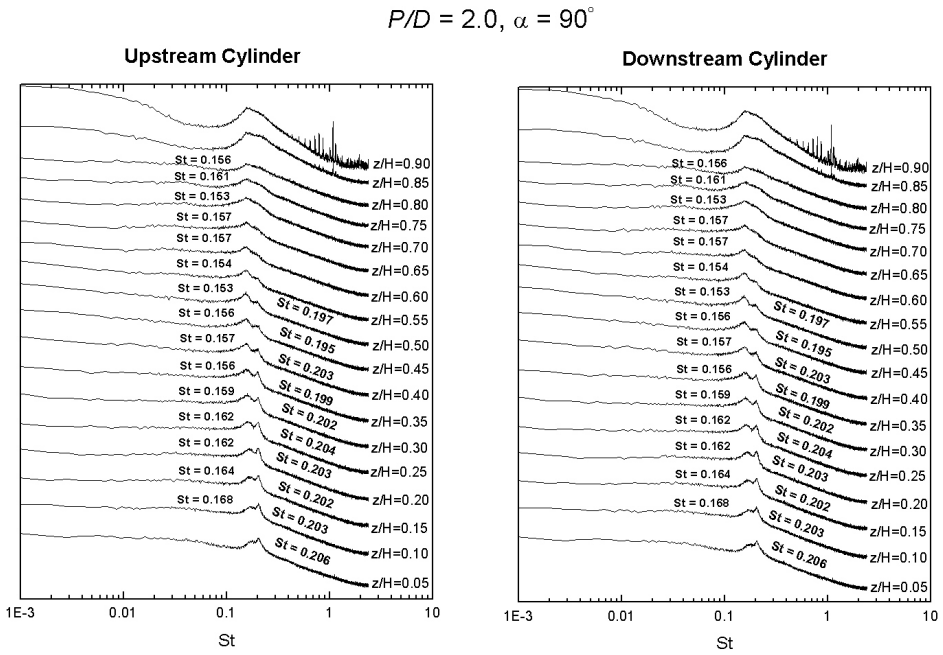

Figure 4.31. Power spectra along the height of upstream and downstream cylinders at P/D = 2, α = 90°, $\mathrm{Re}_D = 2.4\times10^4$, AR = 9 and δ/H = 0.4. Each spectrum represents 250 averages. The vertical (logarithmic) scale is arbitrary, but the same scale is used for each spectrum.

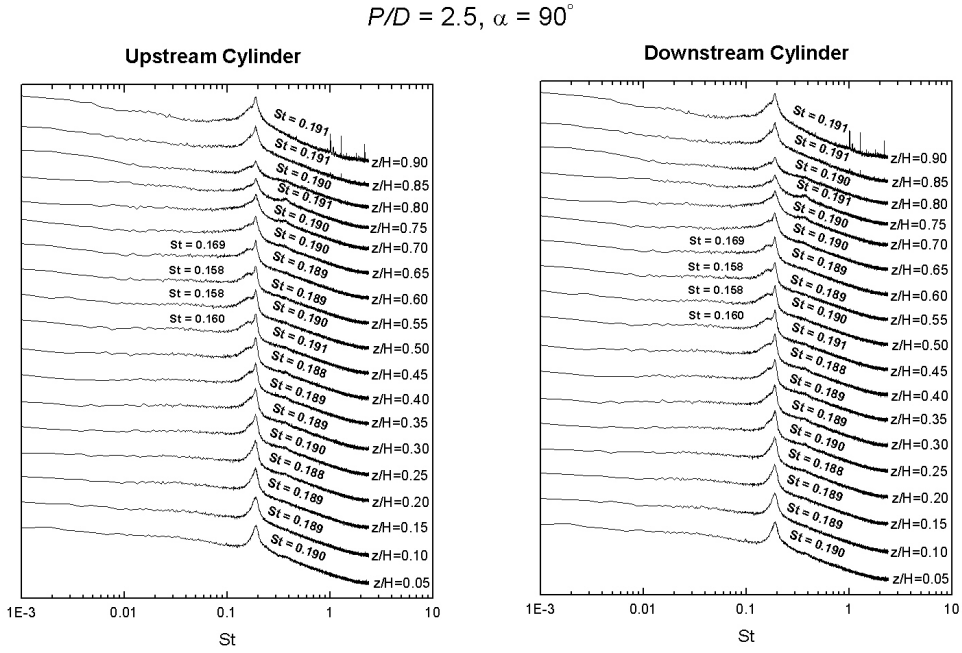

Figure 4.32. Power spectra along the height of upstream and downstream cylinders at P/D = 2.5, α = 90°, $\mathrm{Re}_D = 2.4\times10^4$, AR = 9 and δ/H = 0.4. Each spectrum represents 250 averages. The vertical (logarithmic) scale is arbitrary, but the same scale is used for each spectrum.

Looking at some intermediate staggered configurations, corresponding to $P/D = 2$, $\alpha = 60°$ (Fig. 4.33), and $P/D = 2.5$, $\alpha = 60°$ (Fig. 4.34), the two finite circular cylinders show similar characteristics of the power spectra along the height of the cylinder. Strong peaks are observed around the mid-height and weak peaks or no peaks are found near the base and the free end. A notable variation in the shape of the power spectra is observed around $z/H = 0.6$, showing the effect of the free end. The shape of the power spectra near the tip behaves very strange in some configurations (Figs. 4.33 and 4.34), and it is speculated that the strong broad-banded peaks seen near the free end of the downstream cylinder are caused by the interaction between the tip vortex structures and the downwash flow from the free end, which leads to an observed strong intermittent behavior (Adaramola et al., 2006). Additionally, the transition of the flow pattern occurs along the height of the cylinder and the associated variation in the vortex shedding frequency is observed for some particular cases (Figs. 4.33 and 4.34).

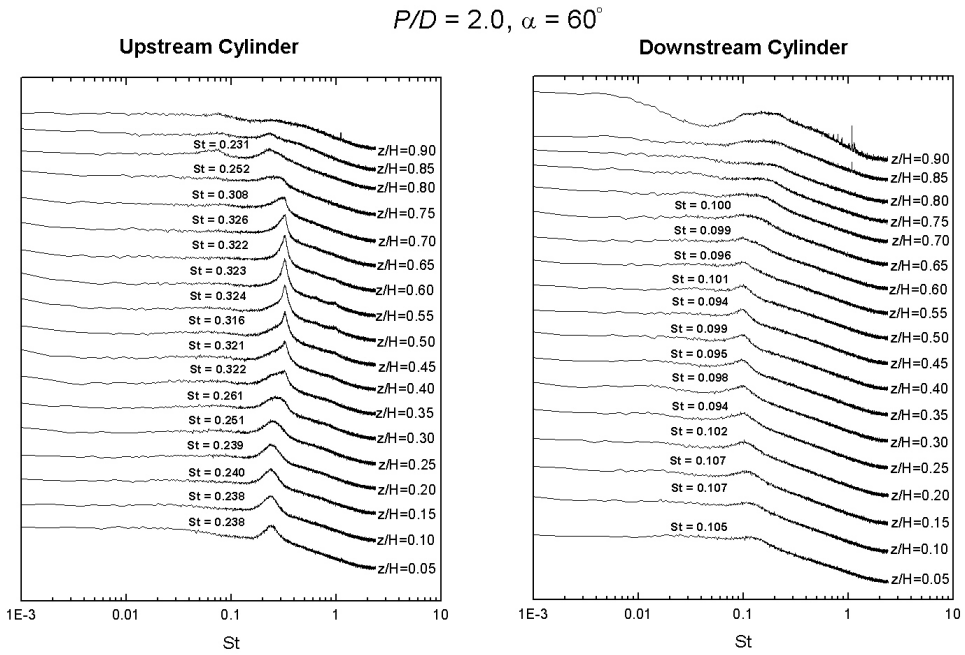

Figure 4.33. Power spectra along the height of upstream and downstream cylinders at $P/D = 2$, $\alpha = 60°$, $\mathrm{Re}_D = 2.4\times10^4$, AR = 9 and $\delta/H = 0.4$. Each spectrum represents 250 averages. The vertical (logarithmic) scale is arbitrary, but the same scale is used for each spectrum.

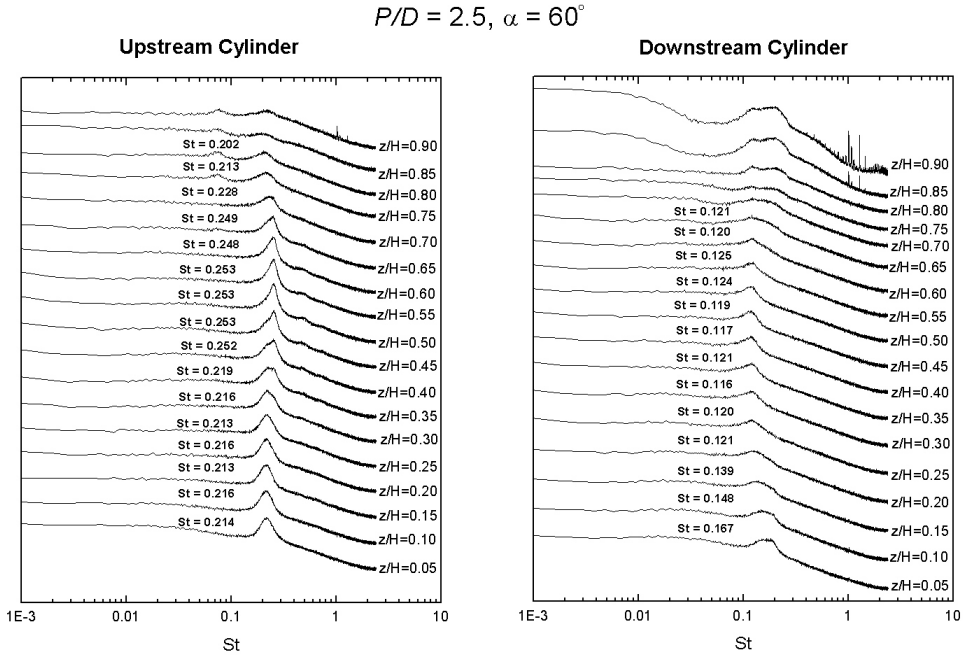

Figure 4.34. Power spectra along the height of upstream and downstream cylinders at $P/D = 2.5$, $\alpha = 60°$, $\mathrm{Re}_D = 2.4\times10^4$, AR = 9 and $\delta/H = 0.4$. Each spectrum represents 250 averages. The vertical (logarithmic) scale is arbitrary, but the same scale is used for each spectrum.

4.3.2.3 Widely Spaced Configuration (P/D = 5)

The power spectra along the height of widely spaced cylinders, shown here for a staggered configuration of $P/D = 5$, behave significantly different from the closely spaced and moderately spaced configurations. Fig. 4.35 shows the power spectra along the height of two staggered circular cylinders at $\alpha = 60°$. It is seen that the power spectra measured behind each cylinder are similar in shape to that of a single finite circular cylinder although the values of the St are not exactly the same since there is still a small interaction between vortex shedding from the two cylinders.

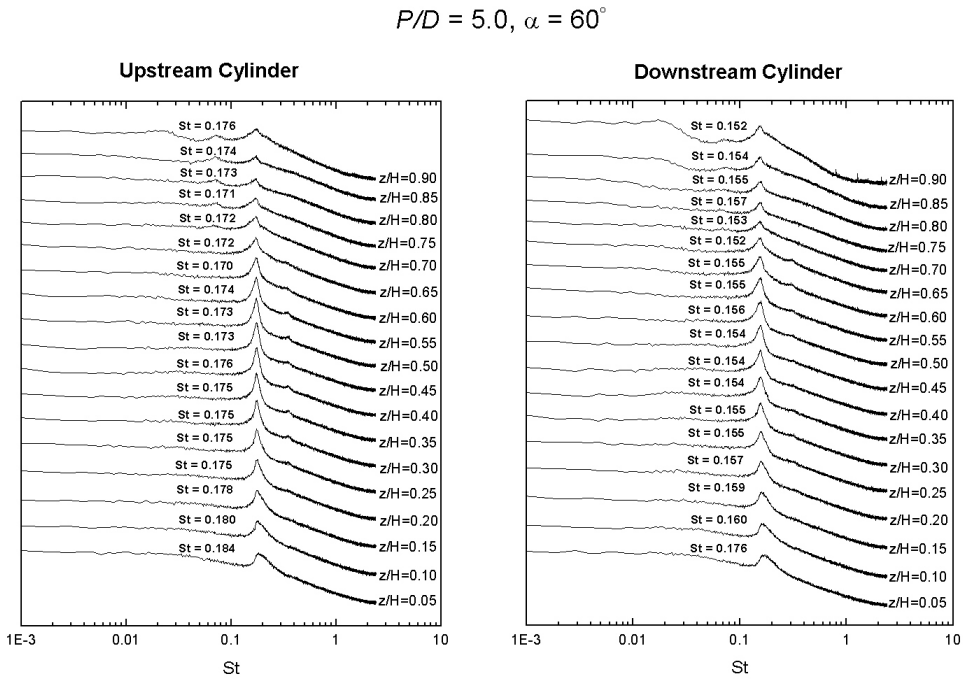

Figure 4.35. Power spectra along the height of upstream and downstream cylinders at $P/D = 5$, $\alpha = 60°$,$Re_D = 2.4\times10^4$, AR = 9 and $\delta/H = 0.4$. Each spectrum represents 250 averages. The vertical (logarithmic) scale is arbitrary, but the same scale is used for each spectrum.

When the two cylinders are arranged in tandem (Fig. 4.36), the power spectra measured from the upstream cylinder shows strong similarity to the single finite cylinder,

whereas for the downstream cylinder, weak peaks are found at the middle section. Based on the wake measurements along the centerline behind a single finite circular cylinder, it is speculated that the mid-height of the downstream cylinder is right at the edge of the recirculation region behind the upstream cylinder and those weak peaks may result from the reduced flow speed in the wake of the upstream cylinder meeting the downstream cylinder. Another notable point is that strong and broad-banded peaks are detected near the free end of the downstream cylinder (Fig. 4.36) and it is believed that those peaks are caused by the compensating flow induced by the "downwash" flow from the freestream.

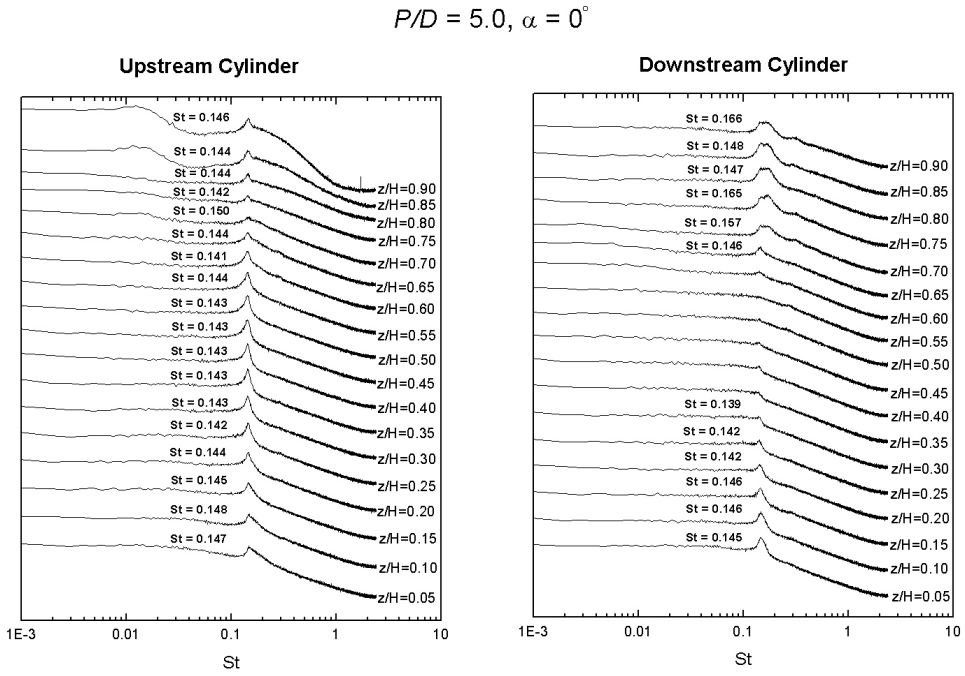

Figure 4.36. Power spectra along the height of the upstream and downstream cylinders at P/D = 5, α = 0°, $Re_D = 2.4\times10^4$, AR = 9 and δ/H = 0.4. Each spectrum represents 250 averages. The vertical (logarithmic) scale is arbitrary, but the same scale is used for each spectrum.

The mean velocity field along the wake centerline behind two tandem cylinders at $P/D = 5$ is shown in Fig. 4.37. Similar to the case of two tandem cylinders at $P/D = 1.125$ and 2 (Figs. 4.21 and 4.30, respectively), an irregularly shaped, discontinuous recirculation region is observed behind the downstream cylinder, however the downwash flow seems to be stronger than the configurations of $P/D = 1.125$ and 2.

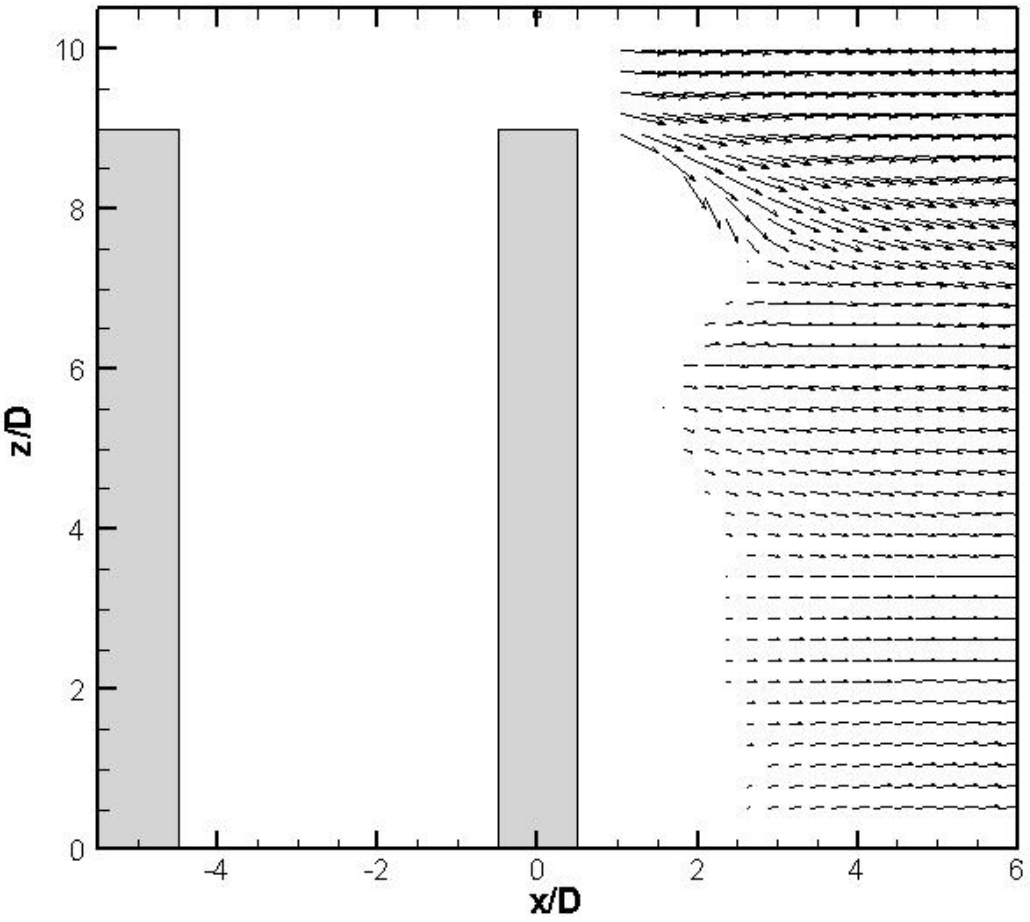

Figure 4.37. Time-averaged velocity field in a vertical plane along the wake centerline, $P/D = 5$, $\alpha = 0°$, $Re_D = 2.4\times10^4$, AR = 9 and $\delta/H = 0.4$.

For two widely-spaced circular cylinders arranged side-by-side, Fig. 4.38 shows that the shape of the power spectra is nearly the same as the single finite circular cylinder with sharp peaks at the middle section, broad-banded peaks near the base and weak peaks

at the free end, indicating that there is almost no interaction between the vortex shedding from the two cylinders.

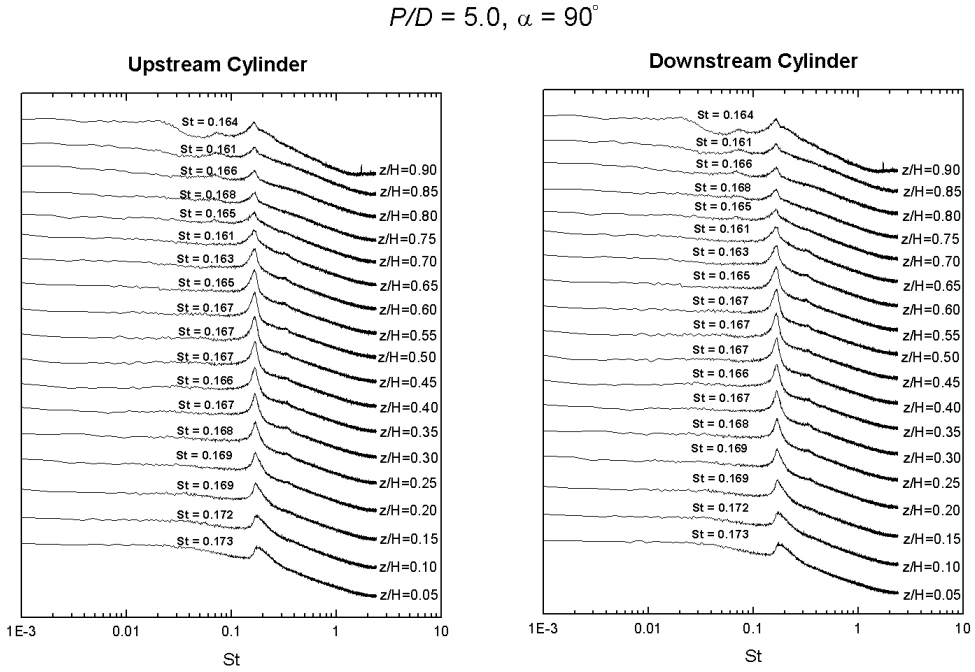

Figure 4.38. Power spectra along the height of the upstream and downstream cylinders at P/D = 5, α = 90°, $Re_D = 2.4\times10^4$, AR = 9 and δ/H = 0.4. Each spectrum represents 250 averages. The vertical (logarithmic) scale is arbitrary, but the same scale is used for each spectrum.

4.4 Wake Measurements

For selected staggered configurations, the time-averaged wake velocity field was measured with a seven-hole probe in order to improve the understanding of the flow structure around the two finite cylinders; several examples have already been shown in Section 4.3, in Figs. 4.21, 4.30, and 4.37. These measurements were carried out for the single finite circular cylinder and two tandem circular cylinders at P/D = 1.125, 2 and 5. The velocity was measured in a vertical plane along the wake centerline (y/D = 0) and in

the cross-stream plane (y-z plane) at x/D = 8 for the single-cylinder and tandem configurations.

4.4.1 Single Finite Circular Cylinder

Figures 4.39 and 4.40 show the time-averaged velocity field measured behind a single finite circular cylinder; non-dimensionalized velocity components ($u^* = u/U_\infty$, $v^* = v/U_\infty$, $w^* = w/U_\infty$) are used in all the figures. The corresponding time-averaged streamwise vorticity, which is represented in dimensionless form as $\omega_x^* = \omega_x D/U_\infty$, is shown in Fig. 4.41, with the in-plane vorticity contours spaced at $\omega_x^* = 0.05$ and with the $\omega_x^* = 0$ contour omitted for clarity. Similar to results reported by Sumner et al. (2004), a strong downwash flow is seen near the tip of the cylinder, as shown in Figs. 4.39 and 4.40, and it weakens along the height of the cylinder towards the base. There is a blank region in Fig. 4.39 where the flow angle is too large to be measured by the seven-hole probe. Upwash flow is found near the base of the cylinder and it is believed to come from the slanted Kármán vortices that appear symmetrical in a time-averaged field. Fig. 4.41 shows that a pair of counter-rotating vortices was found near the tip of the cylinder and it is responsible for the strong downwash flow from the free end. Also, there is another weaker counter-rotating vortex pair near the base of the cylinder induced by the slanted Kármán vortices around the base, which are referred to as the base vortices.

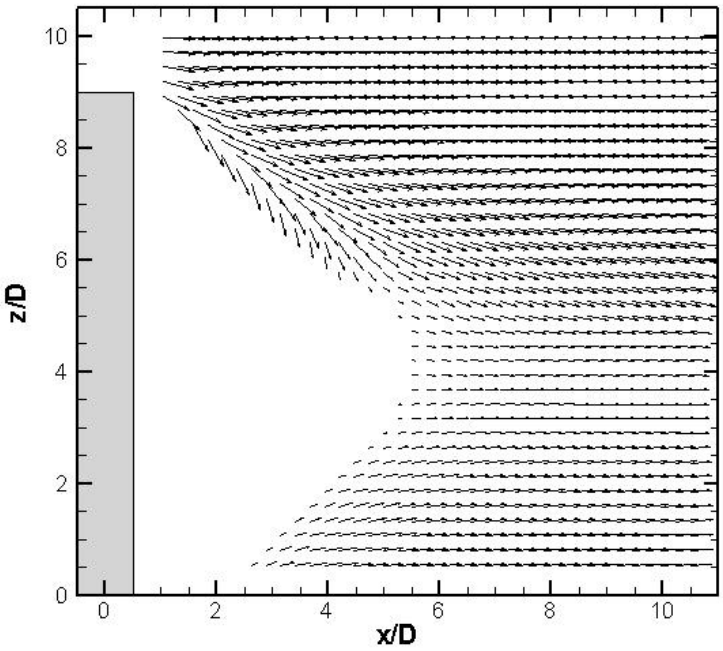

Figure 4.39. Time-averaged velocity field in a vertical plane along the wake centerline behind a single finite circular cylinder, $Re_D = 2.4\times10^4$, AR = 9 and $\delta/H = 0.4$.

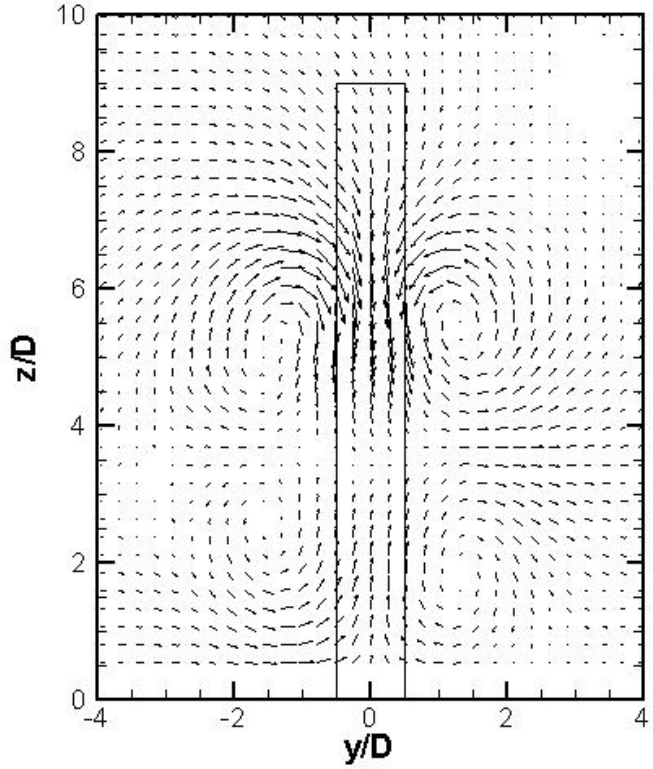

Figure 4.40. Time-averaged cross-stream velocity field behind a single finite circular cylinder at $x/D = 8$, $Re_D = 2.4\times10^4$, AR = 9, $\delta/H = 0.4$.

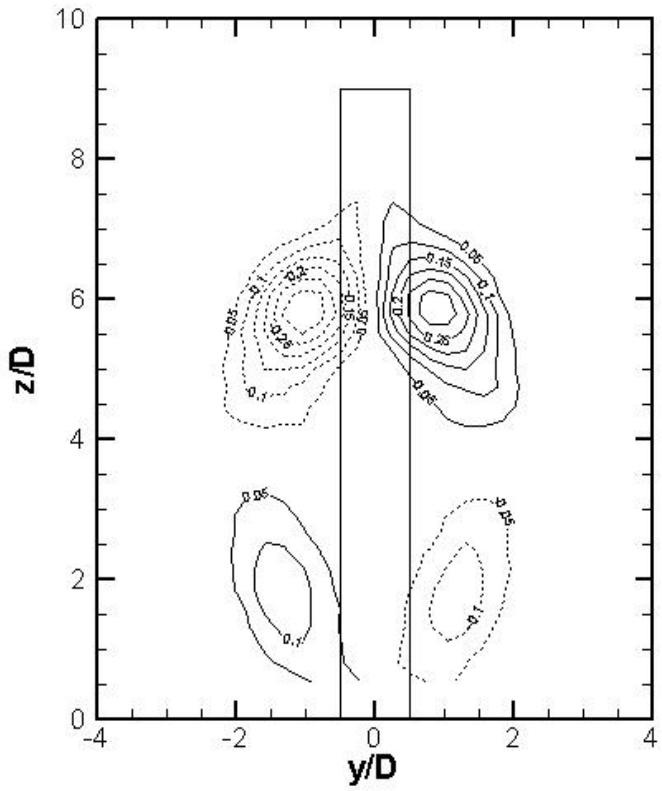

Figure 4.41 Non-dimensional, time-averaged, streamwise vorticity field (corresponding to the velocity field in Fig. 4.43) measured at x/D = 8 behind a single finite circular cylinder, $Re_D = 2.4\times10^4$, AR = 9, δ/H = 0.4. Vorticity contour increment 0.05, minimum vorticity contour ±0.05, solid lines represent positive (CCW) vorticity, dashed lines represent negative (CW) vorticity.

4.4.2 Two Finite Circular Cylinders in Tandem Configurations

It is observed from Figs. 4.42 to 4.50 that the wake velocity and streamwise vorticity fields behind two tandem finite circular cylinders are more complicated than that of the single finite circular cylinder, and that the two pairs of streamwise vortices are not shown clearly in the velocity plots. Furthermore, the recirculation regions behind the two tandem cylinders become irregular and discontinuous. Although the downwash and upwash flow still appear near the free end and base of the cylinder, they turn out to be

much weaker than the case of the single finite circular cylinder.

In addition, as shown in the Figs. 4.43, 4.46 and 4.49, the wake is not perfectly symmetrical, as was expected. The asymmetry was probably caused by a small misalignment of the two cylinders in tandem.

Distinct streamwise vortex structures are observed in Figs. 4.44, 4.47 and 4.50 for two finite circular cylinders arranged in tandem. For $P/D = 2$ (Fig. 4.47), a pair of counter-rotating combined vortices is seen near the free end of the cylinder. It is speculated that the upper vortex originates from the tip of the downstream cylinder and the lower one is generated at the upstream cylinder, and travels downstream with wake flow, and then meets with the vortices from the downstream cylinder. Compared to the results for the single finite circular cylinder (Fig. 4.41), the magnitude of vorticity decreases significantly for the vortices from the downstream cylinder due to the flow interaction near the free ends. However, the base vortices show similar vortex strength. Furthermore, the location of the tip vortices for the tandem configuration is higher than that of the single finite cylinder, indicating that a corresponding weaker downwash flow is induced by the tip vortices from the downstream cylinder.

For $P/D = 5$ (Fig. 4.50), the streamwise vortices emanating from the free end of the upstream cylinder further descend below the free end and thus there are no combined vortices any more. Instead, two pairs of counter-rotating vortices are observed at the upper part of the cylinder. The vortices from the tip of the downstream cylinder are still weaker than the case of the single finite circular cylinder, but are stronger than the case of

P/D = 2 (Fig. 4.47), implying that the flow interaction between the cylinders weakens with the two cylinders spaced further away. Besides, the tip vortices from the upstream cylinder show a much weaker strength than the cases of single cylinder and two cylinders at P/D = 2 as a result of the vorticity diffusion when the vortices travel downstream. For the same reason, there is no base vortex pair measured near the base.

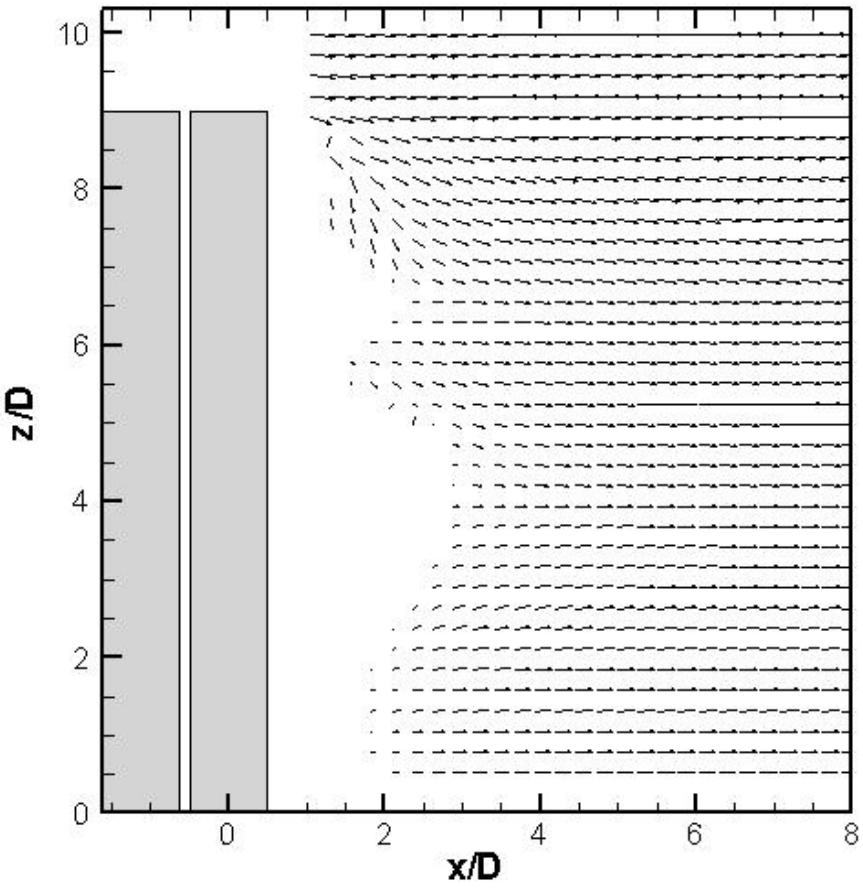

Figure 4.42. Time-averaged velocity field in a vertical plane along the wake centerline, P/D = 1.125, α = 0°, $Re_D = 2.4\times10^4$, AR = 9 and δ/H = 0.4.

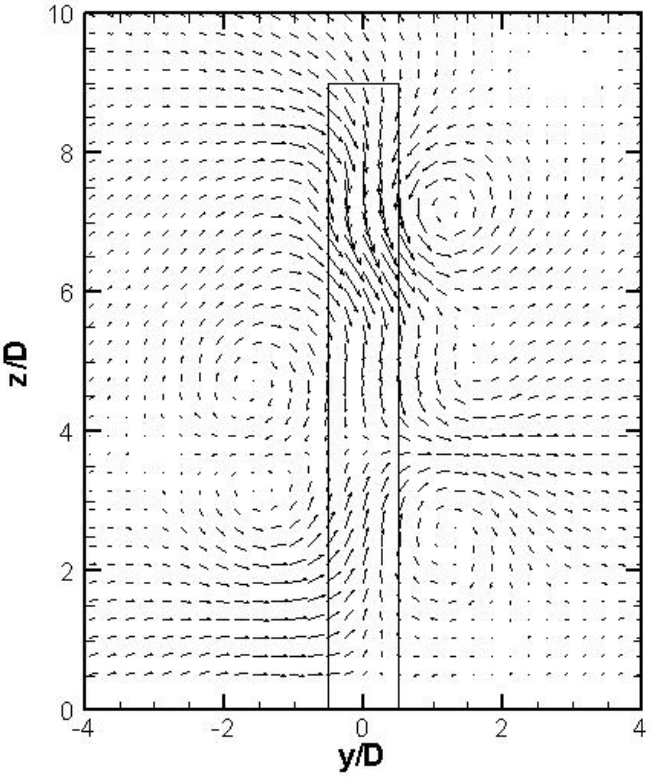

Figure 4.43. Time-averaged cross-stream velocity field at x/D = 8 behind two finite circular cylinders in tandem, P/D = 1.125, α = 0°, $Re_D = 2.4\times10^4$, AR = 9 and δ/H = 0.4.

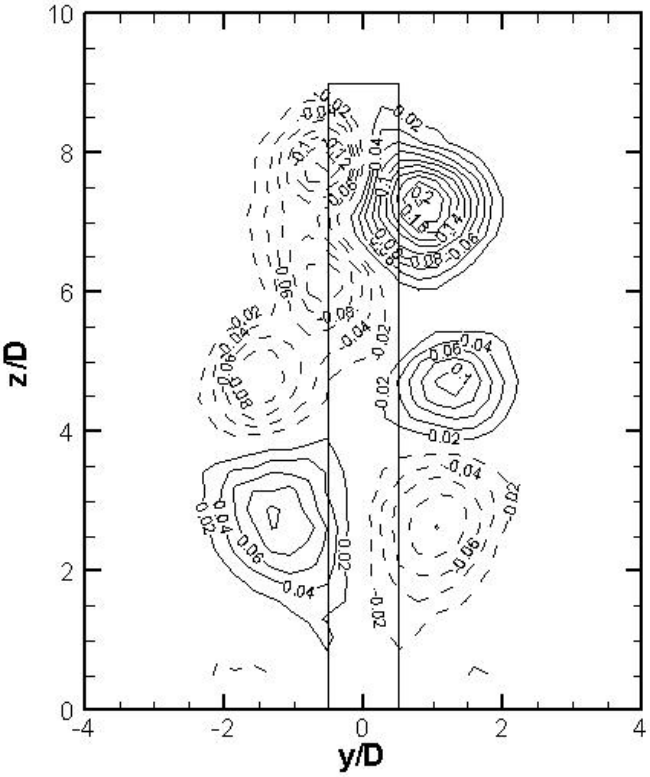

Figure 4.44. Non-dimensional, time-averaged, streamwise vorticity field (corresponding to the velocity field in Fig. 4.46), measured at x/D = 8 behind the two finite circular cylinders in tandem, P/D = 1.125, α = 0°, $Re_D = 2.4\times10^4$, AR = 9 and δ/H = 0.4. Solid lines represent positive (CCW) vorticity, dashed lines represent negative (CW) vorticity.

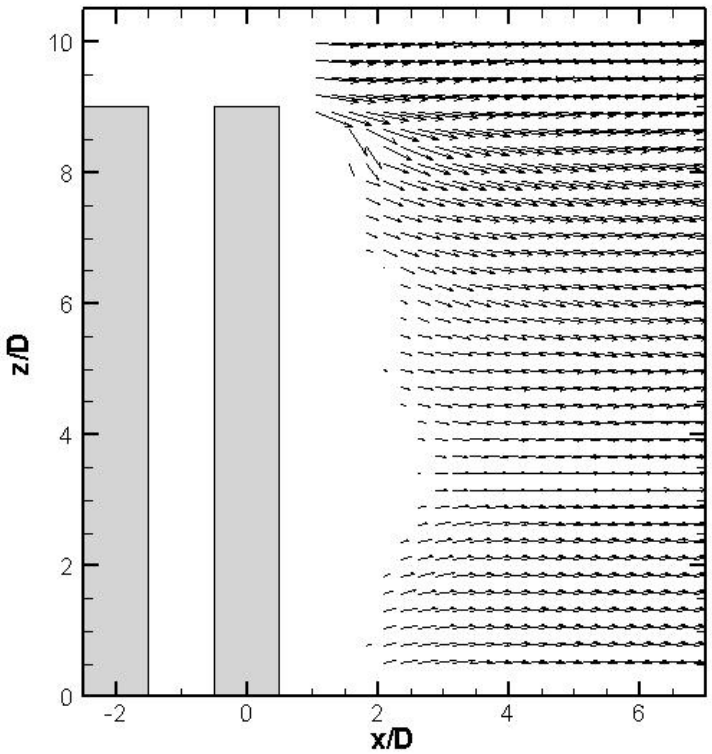

Figure 4.45. Time-averaged velocity field in a vertical plane along the wake centerline, $P/D = 2$, $\alpha = 0°$, $\mathrm{Re}_D = 2.4\times10^4$, AR = 9 and $\delta/H = 0.4$.

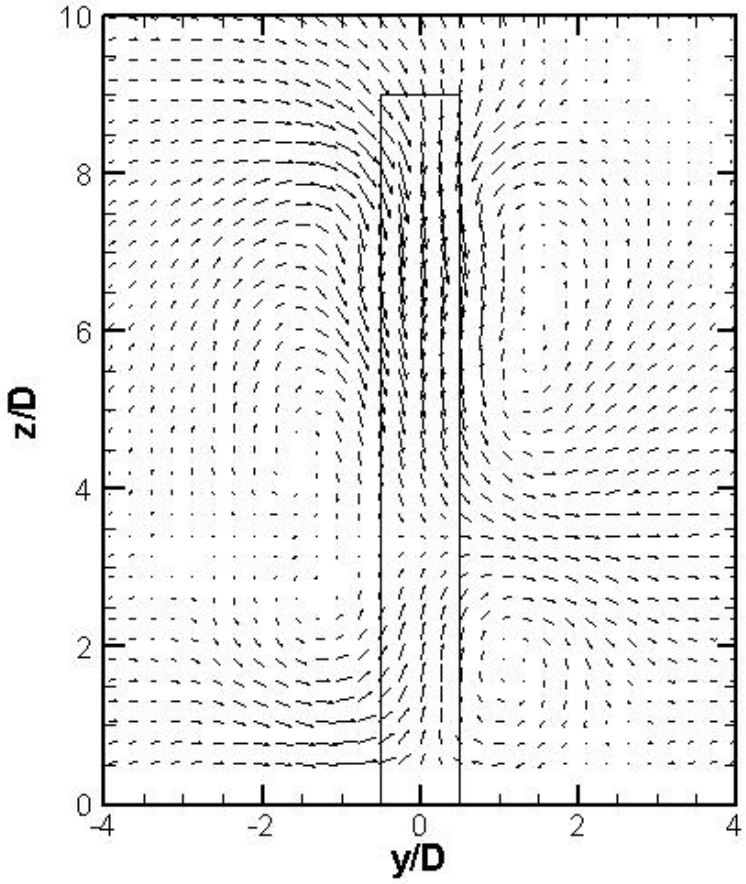

Figure 4.46. Time-averaged cross-stream velocity field at x/D = 8 behind two finite circular cylinders in tandem, P/D = 2, α = 0°, $Re_D = 2.4\times10^4$, AR = 9 and δ/H = 0.4.

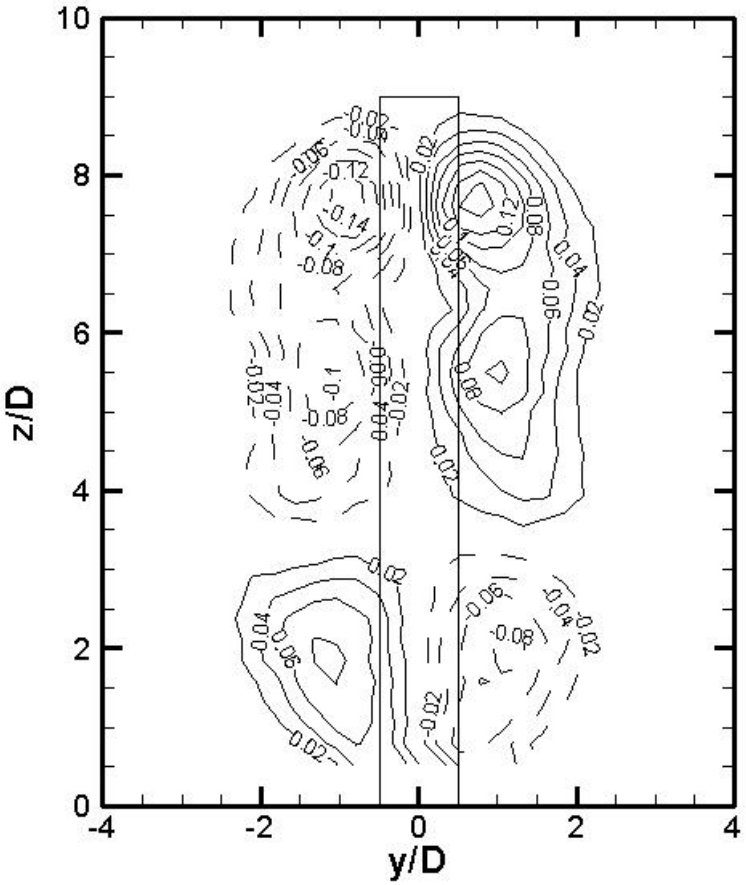

Figure 4.47. Non-dimensional, time-averaged, streamwise vorticity field (corresponding to the velocity field in Fig. 4.49), measured at x/D = 8 behind the two finite circular cylinders in tandem, P/D = 2, α = 0°, $\mathrm{Re}_D = 2.4\times10^4$, AR = 9 and δ/H = 0.4. Solid lines represent positive (CCW) vorticity, dashed lines represent negative (CW) vorticity.

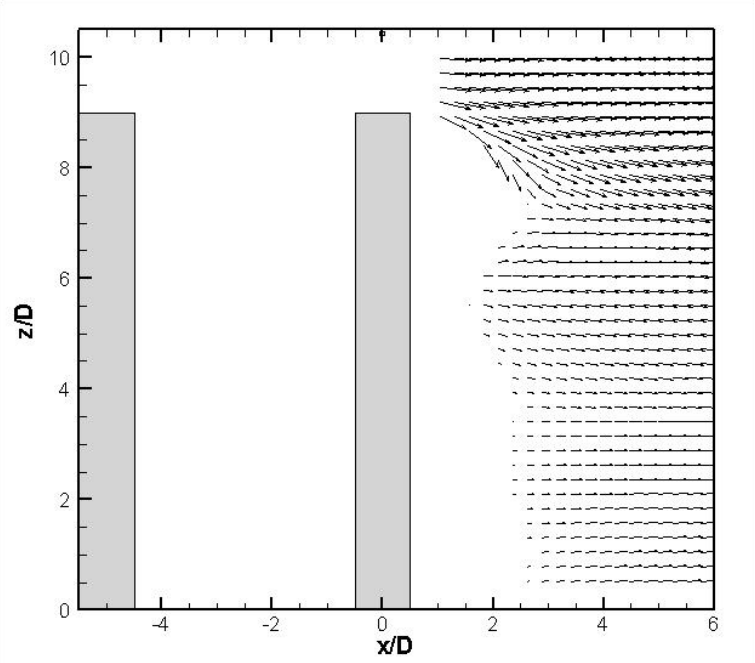

Figure 4.48. Time-averaged velocity field in a vertical plane along the wake centerline, $P/D = 5$, $\alpha = 0°$, $\mathrm{Re}_D = 2.4\times10^4$, AR = 9 and $\delta/H = 0.4$.

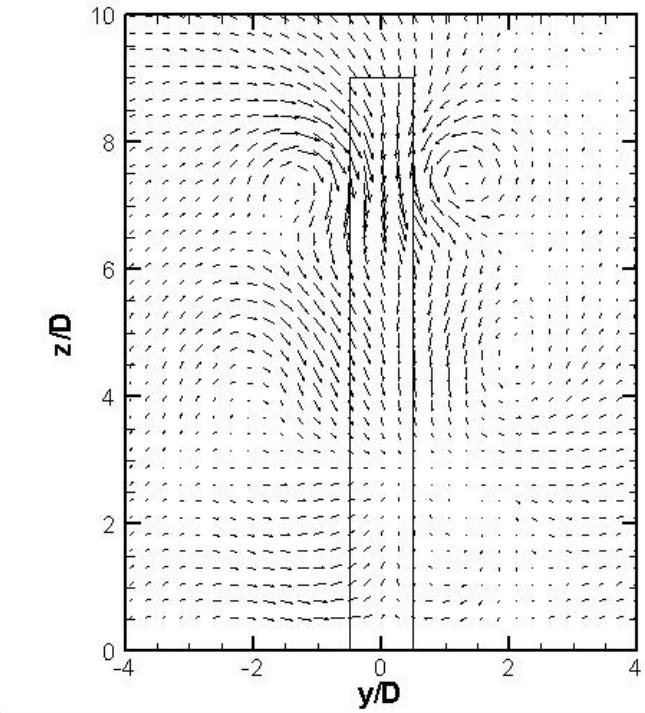

Figure 4.49. Time-averaged cross-stream velocity field at $x/D = 8$ behind two finite circular cylinders in tandem, $P/D = 5$, $\alpha = 0°$, $\mathrm{Re}_D = 2.4\times10^4$, AR = 9 and $\delta/H = 0.4$.

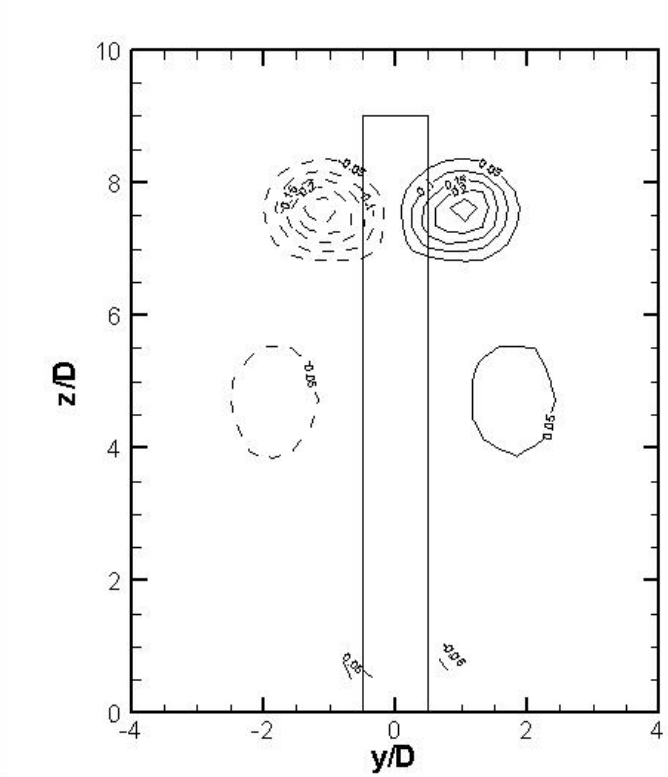

Figure 4.50. Non-dimensional, time-averaged, streamwise vorticity field (corresponding to the velocity field in Fig. 4.52), measured at x/D = 8 behind the two finite circular cylinders in tandem, P/D = 5, α = 0°, $\mathrm{Re}_D = 2.4\times10^4$, AR = 9 and δ/H = 0.4. Solid lines represent positive (CCW) vorticity, dashed lines represent negative (CW) vorticity.

CHAPTER 5

CONCLUSIONS AND RECOMMENDATIONS

5.1 Conclusions

Two staggered finite circular cylinders in cross-flow were studied experimentally in a low-speed closed-return wind tunnel, with the main focus on the vortex shedding from each of the cylinders. For all of the experiments, the Reynolds number based on the cylinder diameter was $Re_D = 2.4\times10^4$. Two identical finite-height circular cylinders of H = 171.45 mm, D = 19.1 mm, and AR = 9, were used, which were chosen to be consistent with previous work reported by Sumner et al. (2004) and Adaramola et al. (2006). These finite circular cylinders were arranged in staggered configurations in the test section. Pitch ratios of P/D = 1.125, 1.25, 1.5, 2, 2.5, 3, 4, and 5, were used in the experiments. The central cylinder of the staggered configuration was mounted vertically from a six-component force balance located outside and below the wind tunnel test-section. The second cylinder was mounted onto a turntable; rotation of the turntable made the angle of incidence change from 0° to 180°, by which the central cylinder could represent either an upstream or downstream cylinder over the full range of incidence angle, α. An incidence increment of 1° and 2° was used, depending on the region of interest. At the position of the central finite circular cylinder, the boundary layer on the test-section ground plane was approximately 68 mm thick, and the ratio of the boundary layer thickness, δ, to the height of the cylinder, H, was $\delta/H \approx 0.4$. The cylinders,

therefore, were partially immersed in the turbulent flat-plate boundary layer on the ground plane, similar to previous work reported by Sumner et al. (2004) and Adaramola et al. (2006) in the same facility.

Four different measurement probes, namely a boundary layer Pitot probe, an X-probe two-component hot-wire probe, a single hot-wire probe, and a seven-hole pressure probe, were used to measure the boundary layer mean velocity profile, the boundary layer turbulent velocity profile, the vortex shedding frequencies from the cylinders, and the velocity fields in the wakes of the staggered-cylinder arrangements, respectively. The measurements obtained from the experiments were broadly divided into three parts, including measurements of the vortex shedding frequencies (or Strouhal number) at the mid-height of the finite circular cylinders, measurements of the vortex shedding frequencies (or Strouhal numbers) along the heights of the finite circular cylinders, and wake velocity field measurements behind the finite circular cylinders. The main conclusions of the research are summarized as follows.

5.1.1. Vortex Shedding at Mid-Height

First, the vortex shedding frequencies were measured at the mid-height ($z/H = 0.5$) of the finite circular cylinders at incidence angles from $\alpha = 0°$ to 180° at increments of 1° or 2°. All eight pitch ratios, of P/D = 1.125, 1.25, 1.5, 2, 2.5, 3, 4, and 5, were used in these experiments. Similar to Sumner et al. (2005) for two staggered infinite circular cylinders, the Strouhal number behavior at mid-height could be broadly classified,

according to pitch ratio, into closely spaced configurations (P/D = 1.125, 1.25), moderately spaced configurations (P/D = 1.5, 2, 2.5, 3) and widely spaced configurations (P/D = 4, 5). More specific conclusions are given below.

- For closely spaced configurations (P/D = 1.125, 1.25), the Strouhal number data measured behind the downstream cylinder are nearly in accordance with the Strouhal number data from the upstream cylinder at all incidence angles, which means the vortices from upstream cylinder and downstream cylinder are shed at the same frequency and they both come from a single vortex shedding process. The two finite circular cylinders therefore behave like a single bluff body. Compared with the Strouhal number values for two staggered infinite circular cylinders, the Strouhal number values for two staggered finite circular cylinders are smaller.
- For moderately spaced configurations (P/D = 1.5, 2, 2.5, 3), two different values of Strouhal number are measured behind the upstream cylinder and downstream cylinder as a result of the interaction between the two vortex shedding processes from the two cylinders. The difference in Strouhal number between the two finite circular cylinders is larger than that between the two infinite circular cylinders because a larger vortex formation region is found at the middle height of a finite circular cylinder, resulting in a stronger interaction between the two finite cylinders than the infinite cylinders. The longer vortex formation length of the finite cylinder and stronger interaction between the two cylinders also causes the

extension of the moderately spaced behavior to P/D = 3, a higher range of pitch ratio than for two infinite circular cylinders.

- For widely spaced configurations (P/D = 4, 5), the results revealed that some interference still exists between the two cylinders, but the cylinders behave more independently and shed vortices more like two independent, isolated single finite circular cylinders, for one cylinder now is far away from the other. Similar to the result for moderately spaced configurations, for the same P/D and α configuration, there is stronger interference between two finite circular cylinders than two infinite circular cylinders, which leads to larger difference in Strouhal number between the two finite circular cylinders than that between the two infinite circular cylinders.

5.1.2. Vortex Shedding Along the Heights of the Cylinders

The vortex shedding frequencies were also measured along the heights of the individual finite circular cylinders, but only at selected incidence angles and pitch ratios chosen to be representative of closely spaced, moderately spaced, and widely spaced staggered configurations. The general conclusions from the power spectra of the velocity fluctuations showed that strong peaks are observed around the mid-height of the cylinders and weak peaks or no peaks are found near the bases and the free ends of the cylinders. The vortex shedding frequency generally does not change along the heights of the cylinders, at least for most staggered configurations. Two distinguished variations

in the shape of the power spectra were observed around z/H = 0.25 and z/H = 0.6, showing the effects of the base and free end of the cylinders.

For some particular configurations, such as two tandem finite circular cylinders at P/D = 1.125, 1.25, 1.5, 2 and 2.5, the Strouhal number magnitude also varied along the heights of the cylinders, corresponding to changes in the flow patterns along the heights of the cylinders. In addition, the shape of the power spectra near the tip behaved very strange for several cylinder arrangements, and this probably resulted from the complicated interaction between the two downwash flows from the two cylinders and their combined effect on the vortex shedding near the free ends of the cylinders.

5.1.3. Wake Velocity Field Measurements

The time-averaged velocity fields in the wakes of the staggered finite circular cylinders were measured with a seven-hole probe. These experiments were only carried out for selected configurations, including the single finite circular cylinder and two tandem finite circular cylinders at P/D = 1.125, 2 and 5. Based on the limited experimental data, it was concluded that the flow structure behind two finite circular cylinders arranged in a tandem configuration is more complicated than that of the single finite circular cylinder. The downwash flow from the tip of the downstream cylinder is weaker due to the flow interaction between the two cylinders near the free end, and this downwash flow becomes stronger as P/D is increased. A similar trend happens to the vorticity of the tip vortex structures. However, the upwash flow behind the downstream

cylinder is not strongly affected by the existence of the upstream cylinder. Also, there is only a slight change in the vorticity of the base vortex structures near the base of cylinder compared to those of the single finite circular cylinder.

5.2 Recommendations

In this thesis research, vortex shedding from two staggered finite circular cylinders in cross-flow was experimentally studied and a large set of experimental data was collected and analyzed. However, some problems still remain unsolved, such as how the downwash flows from the free ends of the two finite circular cylinders interact with each other, and what the flow structures look like near the free ends at various staggered configurations. The use of quantitative flow visualization techniques, such as particle image velocimetry (PIV), is a possible way to solve this problem. Alternatively, more extensive wake measurements using the seven-hole probe would also be recommended, to improve the physical understanding of the flow.

Also, for a complete comparison to the infinite-cylinder data of Sumner et al. (2005), for two staggered infinite circular cylinders, the mean drag force coefficients and mean lift force coefficients also need to be measured. A more comprehensive study could also involve measuring the pressure distributions on the cylinders for selected staggered configurations.

In this research, the hot-wire probe was mostly fixed at a streamwise position of $x/D = 3$ and a cross-stream position of $y/D = 1$. When the two cylinders were arranged at

some particular configurations, there was no vortex shedding detected, which usually led to the conclusion that there was no vortex shedding happening behind the cylinder or the vortex shedding was extremely weak. But, this may not always be the case, for sometimes the phenomenon of no peak in the power spectrum may result from the vortices shed from the cylinder being deflected out of the detection range of the probe. Therefore, additional experiments are recommended where the probe is moved in the streamwise direction and cross-stream direction, to confirm the flow structure when the power spectral peaks are not measured by the hot-wire probe. The movement of the probe position in the streamwise and cross-stream directions was only done for a limited number of cases in the present thesis research, and the effect of probe position has not been extensively investigated in the literature for the staggered configuration (except possibly for the work of Kiya et al. (1980)).

REFERENCES

Adaramola, M.S., Akinlade, O.G., Sumner, D., Bergstrom, D.J., Schenstead, A.J., 2006. Turbulent wake of a finite circular cylinder of small aspect ratio. *Journal of Fluids and Structures* **22**, 919–928.

Adaramola, M.S., Oladeinde, A.O., Sumner, D., Bergstrom, D.J., 2006. Effect of velocity ratio on vortex shedding from a short stack. 2006 ASME Pressure Vessels and Piping Division Conference, July23-27, 2006, Vancouver, BC, Canada. PVP2006-ICPVT11-93121.

Afgan, I., Moulinec, C., Prosser, R., Laurence, D., 2007. Large eddy simulation of turbulent flow for wall mounted cantilever cylinders of aspect ratio 6 and 10. *International Journal of Heat and Fluid Flow* **28**, 561–574.

Akbari, M.H., Price, S.J., 2005. Numerical investigation of flow patterns for staggered cylinder pairs in cross-flow. *Journal of Fluids and Structures* **20**, 533–554.

Akosile, O.O., Sumner, D., 2003. Staggered circular cylinders immersed in a uniform planar shear flow. *Journal of Fluids and Structures* **18**, 613–633.

Coutanceau, M., Defaye, J.R., 1991. Circular cylinder wake configurations: a flow visualization survey. *Applied Mechanics Reviews* **44**, 255–305.

Donnert, G. D., Kappler, M., Rodi, W., 2007. Measurement of tracer concentration in the flow around finite-height cylinders. *Journal of Turbulence* **8**.

Fox, R.W., McDonald, A.T., 1992. *Introduction to Fluid Mechanics*, 4th edition. John

Wiley & Sons, New York.

Gu, Z.F., Sun, T.F., 1999. On interference between two circular cylinders in staggered arrangement at high subcritical Reynolds numbers. *Journal of Wind Engineering and industrial Aerodynamics* **80**, 287–309.

Igarashi, T. 1981. Characteristics of the flow around two circular cylinders arranged in tandem (1st report). *Bulletin of the JSME* **24**, 323–331.

Igarashi, T. 1984. Characteristics of the flow around two circular cylinders arranged in tandem (2nd report, unique flow phenomenon at small spacing). *Bulletin of the JSME* **27**, 2380–2387.

Kareem, A., Kijewski, T., Lu, P.C., 1998. Investigation of interference effects for a group of finite cylinders. *Journal of Wind Engineering and Industrial Aerodynamics*, **77–78**, 503–520.

Kiya, M., Arie, M., Tamura, H., Mori, H., 1980. Vortex shedding from two circular cylinders in staggered arrangement. *ASME Journal of Fluids Engineering* **102**, 166–173.

Kronke, I., Sockel, H., 2007. Measurement of extreme aerodynamic interference forces acting on circular cylinders in turbulent boundary layers. *Journal of Wind Engineering and industrial Aerodynamics* **95**, 1229–1241.

Lee, T., Lin, C.L., Friehe, C., 2007. A. Large-eddy simulation of air flow around a wall-mounted circular cylinder and a tripod tower. *Journal of Turbulence* **8**.

Liu, Y., Cui, Z.X., 2006. Two side-by-side cantilevered cylinders in a cross flow. 2006 ASME Pressure Vessels and Piping Division Conference, July 23-27, 2006, Vancouver, BC, Canada. PVP2006-ICPVT11-93894.

Ljungkrona, L., Norberg, C., Sunden, B., 1991. Free-stream turbulence and tube spacing effects on surface pressure fluctuations for two tubes in an in-line arrangement. *Journal of Fluids and Structures* **5**, 701–727.

Ljungkrona, L., Sunden, B., 1993. Flow visualization and surface pressure measurement on two tubes in an inline arrangement. *Experimental Thermal and Fluid Science* **6**, 15–27.

Luo, S.C., Gan, T.L., Chew, Y.T., 1996. Uniform flow past one (or two in tandem) finite length circular cylinders. *Journal of Wind Engineering and Industrial Aerodynamics* **59**, 69–93.

Narasimha, R., Prasad, S.N., 1994. Leading edge shape for flat plate boundary layer studies. *Experiments in Fluids* 17, 258–360.

Okamoto, S., Sunabashiri, Y., 1992. Vortex shedding from a circular cylinder of finite length placed on a ground plane. *ASME Journal of Fluids Engineering* **114**, 512–521.

Okamoto, T., Yagita, M., 1973. The experimental investigation on the flow past a circular cylinder of finite length placed normal to the plane surface in a uniform stream. *Bulletin of the JSME* **16**, 805–814.

Park, C.W., Lee, S.J., 2000. Free end effects on the near wake flow structure behind a finite circular cylinder. *Journal of Wind Engineering and Industrial Aerodynamics* **88**, 231–246.

Park, C.W., Lee, S.J., 2003. Flow structure around two finite circular cylinders located in an atmospheric boundary layer: side-by-side arrangement. *Journal of Fluids and Structures* **17**, 1043–1058.

Palau-Salvador, G., Stoesser, T., Frohlich, J., Rodi, W., 2007. LES of the flow around two cylinders in tandem. IUTAM Symposium, Corfu, Greece.

Sarode, R.S., Gai, S.L., Ramesh, C.K., 1981. Flow around circular- and square-section models of finite height in a turbulent shear flow. *Journal of Wind Engineering and Industrial Aerodynamics* **8**, 223–230.

Sumer, B,M, and Fredsoe, J., 2007. *Hydrodynamics around Cylindrical Structures*. Singapore ; London : World Scientific Publishing.

Sumner, D., 2002. A comparison of data-reduction methods for a seven-hole probe. *ASME Journal of Fluids Engineering* **124**, 523–527.

Sumner, D., Heseltine, J.L., Dansereau, O.J.P., 2004. Wake structure of a finite circular cylinder of small aspect ratio. *Experiments in Fluids* **37**, 720–730.

Sumner, D., Price, S.J., Païdoussis, M.P., 2000. Flow-pattern identification for two staggered circular cylinders in cross-flow. *Journal of Fluid Mechanics* **411**, 263–303.

Sumner, D., Richards, M.D., Akosile, O.O., 2005. Two staggered circular cylinders of equal diameter in cross-flow. *Journal of Fluids and Structures* **20**, 255–276.

Sumner, D., Wong, S.S.T., Price, S.J., Païdoussis, M.P., 1999. Fluid behaviour of side-by-side circular cylinders in steady cross-flow. *Journal of Fluids and Structures* **13**, 309–338.

Szepessy, S., 1991. On the three-dimensionality of vortex shedding from a circular cylinder. Ph.D. Thesis. The School of Mechanical Engineering, Chalmers University of Technology, Gothenburg, Sweden.

Taniguchi, S., Sakamoto, H., Arie, M., 1981. Interference between two circular cylinders of finite height vertically immersed in a turbulent boundary layer. *ASME Journal of Fluids Engineering* **104**, 529–536.

White, F.M., 2003. *Fluid Mechanics*, 5th edition. McGraw-Hill, Boston.

Williamson, C.H.K., 1996. Vortex dynamics in the cylinder wake. *Annual Review of Fluid Mechanics* **28**, 477–539.

Xu, S.J., Zhou, Y., So, R.M.C., 2003. Reynolds number effects on the flow structure behind two side-by-side cylinders. *Physics of Fluids* **15**, 1214-1219

Zdravkovich, M.M., 1980. Aerodynamics of two parallel circular cylinders of finite height at simulated high Reynolds numbers. *Journal of Wind Engineering and Industrial Aerodynamics* **6**, 59–71.

Zdravkovich, M.M., 1997. *Flow Around Circular Cylinders. Vol. 1: Fundamentals*. Oxford: Oxford University Press.

Zdravkovich, M.M., 2003. *Flow Around Circular Cylinders*. *Vol. 2: Applications.* Oxford: Oxford University Press.

Zdravkovich, M.M., Pridden, D.L., 1977. Interference between two circular cylinders; series of unexpected discontinuities. *Journal of Industrial Aerodynamics* **2**, 255–270.